Electro-spark Deposition Process for Fine Structures and New Materials Coating

by

Jihui Yan

A thesis

presented to the University of Waterloo

in fulfillment of the

thesis requirement for the degree of

Master of Applied Science

in

Mechanical and Mechatronics Engineering

Waterloo, Ontario, Canada, 2023

© Jihui Yan 2023

Author’s Declaration

I hereby declare that I am the sole author of this thesis. This is a true copy of the thesis, including any required final revisions, as accepted by my examiners.

I understand that my thesis may be made electronically available to the public.

Abstract

The electrospark deposition (ESD) process can be used in industry to apply coatings and repair components. It uses a rod-shaped conductive material as the raw material for the electrode, which is melted by the high temperature of the process of discharging to form an electric spark during contact with the substrate, which is then transferred and solidified to the substrate surface. The speed of this process is also accompanied by the melting of the substrate surface, which fuses with the electrode material to give a mixed layer at the interface between the coating and the substrate. However, the deposition process is extremely fast and thus the heat input is small, which has little to no effect on the properties of the substrate.

Because the temperature at which electrical sparks are generated is much higher than the melting point of all materials, ESD can make coatings from almost any conductive material. Some materials can also be manufactured into thick buildups with ESD. This process can be treated as an additive manufacturing technique, which can be used to perform the structural repair of damaged parts with fine structures, such as thin wall geometries, thus reducing the cost of replacement parts and reducing the scrap waste of damaged parts. The repair of damaged thin-walled structures with Inconel 718 is described in Chapter 3 of this report, which includes optimization of parameter sets during the manufacturing, and analysis of microstructure, microhardness, and heat-affected zone (HAZ).

The high temperature in the process of manufacturing a coating with ESD melts the electrode and the substrate, but if there is a conductive interlayer between the two, such as a layer of metal powder, the high temperature of the spark will melt the powder instead, which then fuses and solidifies on both the substrate and electrode so that the transfer of electrode material can be prevented. Therefore, ESD will be used to fabricate the M/HEA coating using powder as the interlayer that will be presented in Chapter 4, as well as the optimization of the manufacturing process, and analysis of microstructure, as well as the wear resistance of M/HEA coating fabricate using electrospark powder deposition (ESPD).

Some application trials with ESD are performed and will be presented in Chapter 5, which describes the repairing of thin walls using manual ESD and automated ESD. The fabrication of high entropy alloy (HEA) coatings with the conventional ESD process will also be presented as a HEA coating trial, along with the discussion of microstructure, microhardness, and the wear resistance of this HEA.

Acknowledgements

First and Foremost, I would like to thank my Supervisor Professor Peng Peng, and Prof. Norman Zhou. Their unwavering support and advice helped guide and lead me for the past two years. I would also like to extend my gratitude towards all the members of my friends, Kaiping and Pablo, and the many members of CAMJ. Through working alongside a great group of talented and motivated people I have learned so many skills and life lessons. I am looking forward to moving forward with my full passion.

Dedication

To my mother Youling, amd my father Jianhong. Your selfless support inspires me to move forward towards my goals.

Table of Contents

List of Figures

List of Tables

Chapter 1

Introduction

1.1 Problem Statement

Metal deposition processes are often used in the manufacture of coatings, which can attach special properties to the workpiece, such as resistance to corrosion, wear, etc. Besides the manufacturing coating, some deposition processes can create thick buildups to modify the surface structure. This process can then be utilized to perform the structural repair of the damaged workpiece with fine surfaces such as the parts with thin wall geometries, which extends the life of the workpiece and reduces the cost of replacement and scrap due to damage.

A low-energy-input deposition technique, direct laser deposition or directed energy deposition (DED) is a common technique in additive manufacturing that uses metal powder as the feedstock, melts the powder using a laser or electron beams, and builds up the powder material layer by layer on the substrate, which can also be used to repair the damaged parts. Compared to high-energy-input technique, such as gas tungsten arc welding (GTAW), DED-repaired parts have the same lifetime as the original part, while GTAW has only 21% of the lifetime of the original part [1]. This is because the high energy input of GTAW has a greater impact on the microstructure of the substrate, which changes the surface properties of the workpiece, resulting in a significant reduction in the service life of the part [2], [3]. Therefore, high-quality repair or manufacturing of coatings with low energy input technology is more economical and has a strong sustainability.

In this thesis, a low-energy input deposition technique, electrospark deposition (ESD), will be discussed, which uses high temperatures during electrical discharge to melt, transfer, and solidify metal rods onto a substrate to form a layer of coating. The temperature of the sparks is much higher than the melting point of the metal electrodes, which means that ESD can deposit almost any conductive material onto the substrate to form a coating. Moreover, the heat input of this technique has minimized influence on the substrate, which shows a high potential for utilization. In addition, this easy-to-carry and inexpensive technique also shows the advantage of ESD. There has been a great deal of research into the manufacture of coatings using ESD in surface modification and repair. For example, the repair of a damaged cannon cradle on an M1A1 main battle tank with Inconel 718 results in a 97% reduction in replacement cost, with only labor and material costs [4].

In addition, one of the most popular research topics nowadays is the medium/high-entropy alloys (M/HEAs) proposed in 2004 [5]. Extensive research has been conducted in various fields such as bulk, powder, coating, and thin film. However, the complex and diverse composition of HEAs, including the types and quantities of elements in the alloys, results in significant variations in the properties of different M/HEA alloys [6]. This has created a substantial knowledge gap within the HEA system, providing ample opportunities for further research and advancement in the field of HEAs.

This report also describes the research on manufacturing M/HEA coatings using ESD, which utilizes both powders and electrodes as feedstock, respectively, to achieve coating formation by high temperature melting and resolidification. The intuitive elemental composition of M/HEA alloys (equiatomic) makes powder deposition feasible and enables the production of such coatings, whose manufacturing process will be discussed in detail.

1.2 Thesis Objectives

In previous studies, the application of ESD has been more oriented towards the fabrication of coatings or repair of damage on wide planar substrates using metal rods as feedstock, but in this report, the extended use of ESD will be presented. For example, repairing special structures or manufacturing coatings using different feedstock.

a) The first part of this report is to investigate the repair of thin-walled structures with ESD. Some thin-walled workpieces, such as turbine blades and pump impellers in aeroengines, may be damaged during manufacturing or after servicing to develop cracks or erosion. As the cost of a part is too high to make the replacement, a repair technique is a more efficient solution. Therefore, repair on thin-walled structures is studied; in other words, effective buildup on thin walls is the focus of this section.

b) The second part is the fabrication of medium/high entropy alloys. The conventional ESD process uses metal rods as the electrode, but for M/HEAs, it seems to be possible to use metal powder as the feedstock. This section will investigate the feasibility of using metal powders as feedstock to manufacture M/HEA coatings.

c) The third part is the trial processing of repairing the damaged part as described in the first part, the automated ESD repair is also included in this section, as well as the HEA coatings with conventional ESD steps, which marks the beginning of research on HEA coatings.

1.3 Thesis Approach and Overview

This thesis details the repair and coating fabrication for two ESD extension usages. As part of the possible process development, deposition parameters will be investigated and compared to obtain the most appropriate parameter sets, the deposited microstructure, metallographic, and mechanical properties will also be characterized.

Chapter 2 begins with a review of the coating techniques, followed by an introduction of ESD, with its mechanism and the effect of parameters in order to familiarize the reader with the technology. The third part is the review of materials used in ESD for different purposes, and a detailed review of ESD of Inconel 718, including chemical composition and phase transformation of the material, are presented to give the reader an idea of the microstructural analysis of this study. The study of fabrication of buildup on thin walls with Inconel 718 will be presented and discussed in Chapter 3, which includes the comparison and selection of parameter sets to obtain a higher-quality buildup with a guaranteed deposition rate. The microstructure and microhardness of the buildup will be characterized, and the results obtained with different parameter sets will be presented and discussed. The effect on the substrate is also investigated, including the microhardness and microstructure of the heat affected zone (HAZ), because unlike coatings, buildups require a longer deposition time, which increases the heat input, and the thermal transfer efficiency of thin-walled structures is much smaller than that of bulk materials. In addition, a trial of repair of thin-wall using the manual and automated ESD will be presented in Chapter 5.

Chapter 2 also reviews the M/HEA, including its definition, thermal stability, HEA types, and the preparation methods of different forms of the alloy. The focus is on reviewing the different ways to fabricate coatings and presenting articles on the use of ESD mechanisms to fabricate coatings from powder as feedstock, from which this study was inspired. Chapter 4 then presents the fabrication of HEA coatings on substrates using single-element powders as feedstock to form the coating using ESD, which describes the preparation of the mixed powder and the optimization of the ESD process to obtain a suitable parameter set and high-quality coating. Afterward, characterization techniques are used to

confirm that the fabricated alloy is desired, the microstructure of the coating and substrate is analyzed, which includes microhardness, HAZ, etc., and wear tests of the coating are performed. Moreover, Chapter 5 presents the ESD with AlCrFeCoNi HEA electrodes. The microstructure is analyzed, followed by characterization and measurement of microhardness and wear tests.

Chapter 2

Literature Review

2.1 Process for Metal Coatings

Metal coating methods play a crucial role in enhancing the surface characteristics and functional capabilities of various materials in multiple industries. The technology for producing diverse coatings has undergone continuous optimization and refinement, culminating in the establishment of a mature system. For example, thermal spray is a process where melted or heated materials, such as metals, ceramics, or polymers, are sprayed onto a surface to form coating. Cold spray, on the other hand, is a similar technique but operates at lower temperatures, allowing for the deposition of metals without melting. Laser cladding uses a high-energy laser to melt and fuse the feedstock material onto substrate, creating a strong metallurgical bond. Electroplating is an electrochemical process where a metal coating is deposited onto a substrate through the application of an electric current. Galvannealed (GA) coating is a specialized type of coating applied to steel surfaces through a process. It offers corrosion resistance and enhanced paint adhesion, making it suitable for automotive and construction applications. Galvanized coating refers to the application of a layer of zinc onto iron or steel surfaces. It provides excellent corrosion protection by creating a barrier between the substrate and the environment. These coating techniques offer a range of benefits and find applications in various industries for surface protection, customization, and functional enhancements.

The objective of this literature review is to present a comprehensive overview of common metal coating techniques, encompassing their methodologies, applications, and recent advancements. By summarizing key findings from the literature, the review highlights the advantages and limitations of each technique and explores their specific applications across diverse fields. Additionally, it investigates recent progress and emerging trends in metal coating techniques, with a particular emphasis on novel materials, enhanced deposition processes, and surface engineering strategies.

2.1.1 Thermal Spray

Thermal spray, as a coating technology, has a long and dynamic history of growth and advancement, which has experienced notable developments that have propelled its extensive use across diverse industries in the present day. This section presents a summary of the historical development and

evolution of thermal spray techniques, emphasizing important milestones and the driving forces behind their continuous improvement.

The roots of thermal spray can be traced back to the early 20th century when the first thermal spray process called metallic flame spraying [7], [8]. Later, the melting metal wires in a combustion flame and propelling the resulting molten droplets onto a substrate using compressed air [7], [8]. This marked the fundamental beginnings of thermal spray technology. The technology was extensively employed to deposit anti-corrosion and wear-resistant coatings on components. These initial industrial applications drove the refinement of thermal spray processes and equipment.

Following that, new thermal spray techniques were developed, and alternative heat sources were introduced. In the 1950s, the detonation gun spraying technique emerged, which allowed for the deposition of high-velocity coatings by utilizing energy from a detonating mixture of gases and oxygen [7], [8]. This technique resulted in improved coating adhesion and density. In the 1960s, the plasma spraying process revolutionized thermal spray technology [7], [8]. Plasma spraying employed a high-temperature plasma arc as the heat source to melt and propel feedstock materials onto a substrate. This technique offered enhanced control over coating properties, improved deposition efficiency, and the ability to spray a wide range of materials, including ceramics.

During the 1970s, high-velocity oxy-fuel (HVOF) spraying gained prominence as a thermal spray technique [7], [8]. It involved the combustion of a fuel gas, typically hydrogen or hydrocarbon, mixed with oxygen to produce a high-velocity and high-temperature flame. HVOF spraying provided superior coating density, reduced oxide content, and improved bond strength compared to traditional flame spraying.

Over time, progress in materials science has broadened the scope of thermal spray applications. The range of coating materials has expanded to encompass ceramics [9]–[11], polymers [12]–[14], composites [15]–[17], and nanostructured substances [18]–[20]. This advancement enables the production of customized coatings with specific properties, such as thermal barriers, electrical conductivity, and biocompatibility. Thermal spray coatings now find widespread use in industries such as aerospace [21], automotive [22], [23], power generation [24], [25], and biomedical sectors [26], [27]. Recent advancements in thermal spray technology focus on optimizing processes, automation, and environmental sustainability. Advanced modeling and simulation techniques, in combination with in-

situ monitoring and control strategies, have enhanced coating quality and efficiency [28]–[30].

The historical progression and advancement of thermal spray technology illustrates the transformation from early flame spraying techniques to the sophisticated and adaptable coating methods we have today. The increasing requirements for enhanced performance, longevity, and versatility across diverse industries have propelled the continuous improvement and expansion of thermal spray processes. Through ongoing research and development, thermal spray is poised to play a crucial role in tackling future coating complexities and fulfilling the ever-changing demands of industries globally.

Flame Spray. Flame spraying is a coating technique that employs a combustion flame to heat and propel coating materials onto a substrate. This section offers a comprehensive overview of the fundamental principles and distinctive process characteristics associated with flame spraying.

Flame spraying utilizes a fuel gas, such as acetylene, propane, or hydrogen, mixed with oxygen to generate a high-temperature combustion flame that serves as the heat source [7], [8]. This flame provides the necessary energy to melt the coating material. The coating materials, typically in the form of wires or powders, depends on specific application requirements, are introduced into the flame [7], [8]. The intense heat of the flame melts the material, transforming it into droplets that are either fully molten or partially molten. To propel these droplets towards the substrate, compressed air or inert gas is employed. Upon contact with the substrate, the molten or semi-molten droplets rapidly solidify, forming a coating. A sketch and photo of the flame spray are shown in Fig. 2-1.

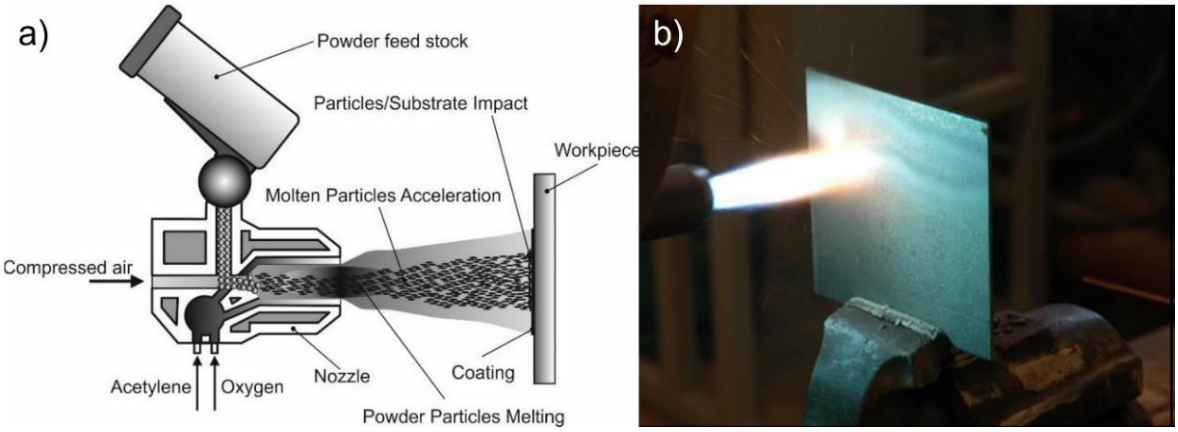

Figure 2-1 a) a sketch and b) a photo of flame spray, adapted from Czupryński [31]

Flame spraying possesses distinct process characteristics that impact the resulting coating quality and properties. Thickness control is achievable in flame spraying, with coatings typically ranging from a few micrometers to several hundred micrometers. Adjusting parameters like the coating material feed rate and spraying speed allows for thickness modulation [7], [8]. Porosity is a common feature in flame-sprayed coatings due to the solidification of molten droplets. Factors such as particle size, spraying distance, and gas flow rates influence porosity, which can be mitigated through post-coating processes like sealing or impregnation [7], [8]. The adhesion between the coating and substrate is critical for coating integrity and performance. Attaining strong adhesion and bond strength involves surface preparation, compatibility with the substrate material, and appropriate spraying parameters [7], [8]. Flame-sprayed coatings typically exhibit a relatively rough surface texture. Fine-tuning spraying parameters such as working distance, gas flow rates, and powder size can control the degree of roughness [7], [8]. Although considered less efficient compared to plasma spraying or HVOF spraying, flame spraying remains widely employed in diverse applications due to its simplicity, cost-effectiveness, and versatility.

Plasma Spray. Plasma spraying is a process that applies coating materials to a surface by utilizing a high-energy plasma arc. This arc generates significant heat, melting the coating materials and propelling them onto the substrate.

A plasma arc is generated by directing a high-velocity gas, typically argon or nitrogen, through an electric arc. This gas becomes ionized, creating a plasma jet with extremely high temperatures, often reaching several thousand degrees Celsius [7], [8]. The coating material, either in the form of powders or wires, is introduced into the plasma jet. The intense heat generated by the plasma arc swiftly melts the material, turning it into molten or partially molten droplets. These droplets are propelled toward the substrate by the high-velocity plasma jet [7], [8]. Upon impact, the droplets spread out and solidify, forming a coating that strongly adheres to the substrate. A sketch of the plasma spray process is shown in Fig. 2-2.

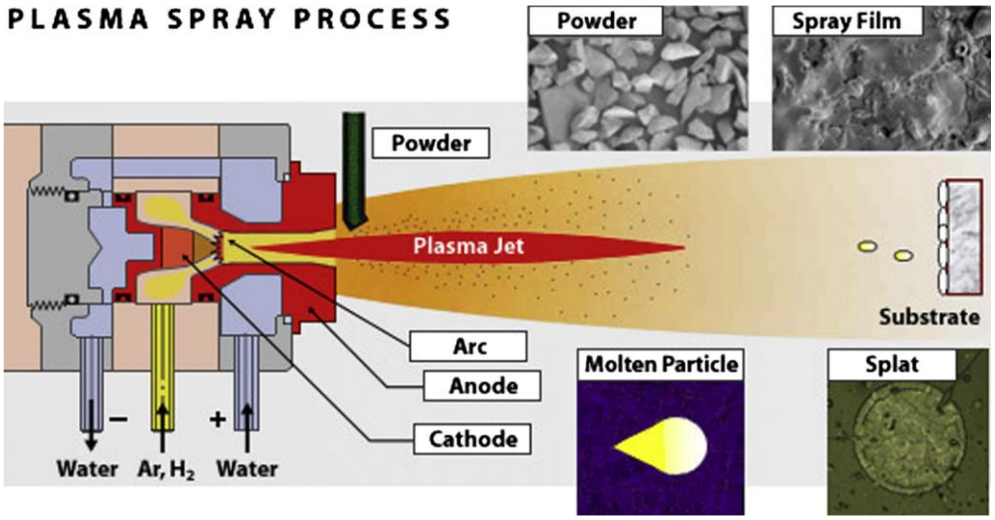

Figure 2-2 A sketch of the plasma spray process, adapted from Zhang et al [32]

The process characteristics of plasma spraying have a direct impact on the quality and effectiveness of the resulting coating. Similar to flame spraying, plasma spraying allows for control over coating thickness, composition, and porosity. Plasma-sprayed coatings generally have high densities due to the intense temperature and energy of the plasma jet [7], [8]. The molten droplets cool rapidly upon contact, resulting in coatings that are dense and firmly adhered. Plasma spraying is compatible with various substrate materials, including metals, ceramics, and certain polymers [7], [8], although careful consideration of substrate properties and surface preparation is essential to ensure strong adhesion. The microstructure of plasma-sprayed coatings typically exhibits a layered or flattened droplet arrangement. This microstructure is influenced by factors such as powder particle size, spray parameters, and substrate temperature.

HVOF. High-velocity oxy-fuel (HVOF) spraying is a thermal spray technique where coating materials are propelled onto a substrate through the use of a high-speed stream of combustion gases.

HVOF spraying encompasses the combustion process of a fuel gas mixture (such as hydrogen, propane, or kerosene) with oxygen within a dedicated chamber [7], [8]. This combustion generates a high-velocity and high-temperature gas stream. Fine powder coating material is introduced into the combustion chamber or the gas stream near the nozzle. As the powder particles pass through the combustion zone, they undergo acceleration and heating [7], [8]. The high-velocity gas stream propels the heated powder particles toward the substrate, reaching speeds between 300 and 1,000 meters per

second [7], [8]. Upon impact on the substrate surface, the particles deform and create a compact and strongly bonded coating.

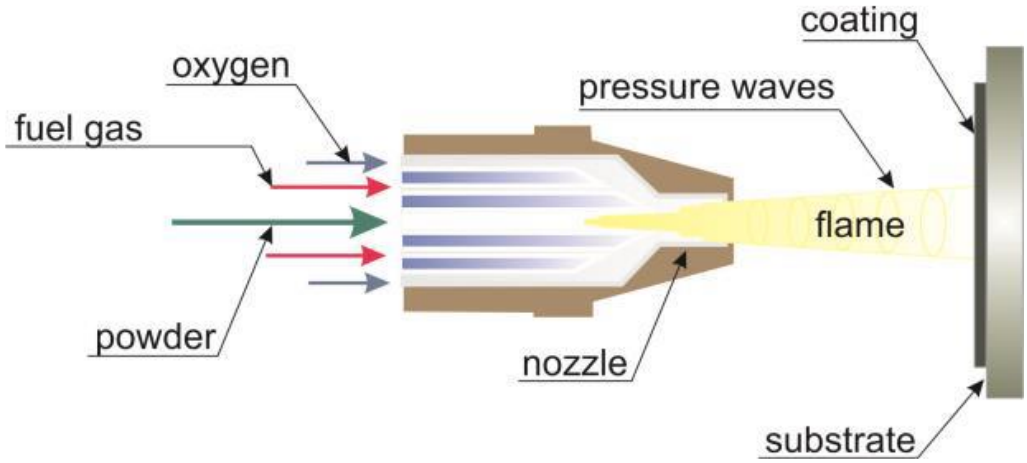

Figure 2-3 Schematic HVOF process, adapted from Jonda et al [33]

HVOF spraying provides several advantages when compared to alternative thermal spray techniques. HVOF coatings demonstrate remarkable density and minimal porosity, attributed to the high kinetic energy of the powder particles and the effective melting and bonding achieved during the spraying process [7], [8]. This leads to enhanced mechanical properties, including elevated hardness, improved wear resistance, and heightened fatigue resistance. HVOF spraying produces coatings with reduced oxide content, resulting in superior corrosion resistance and oxidation resistance, particularly in high-temperature environments. Additionally, the high velocity of the powder particles and the efficient combustion process in HVOF spraying minimize heat transfer to the substrate [7], [8], thereby reducing the risk of substrate distortion or degradation.

HVOF spraying enables the application of coatings with adjustable thicknesses, typically ranging from 25 to 500 micrometers. The control of coating thickness can be achieved by modifying the powder feed rate and spraying duration [7], [8]. HVOF coatings display exceptional adhesion to the substrate due to the high kinetic energy and deformation experienced by the powder particles upon impact. This results in a robust bonding strength and reduces the likelihood of delamination [7], [8]. Moreover, HVOF coatings typically exhibit a compact and well-consolidated microstructure, characterized by minimal porosity and oxide content. The microstructure is influenced by various factors, including powder properties, combustion parameters, and spraying conditions.

2.1.2 Cold Spray

Cold spray coating technology, alternatively referred to as supersonic particle deposition or cold gas dynamic spraying, is a modern advancement within the realm of surface engineering. It entails the application of solid particles onto a substrate at supersonic speeds, leading to the creation of a compact and firmly adhered coating. This section presents a comprehensive introduction to the origins and importance of cold spray coating technology.

The inception of cold spray coating technology can be traced back to the 1980s when it emerged as a method primarily employed for repairing aerospace components afflicted by damage or wear [35]. This innovative approach stemmed from the realization that solid particles propelled at high velocities could undergo plastic deformation upon collision, consequently establishing a robust bond with the substrate [34], [35]. As time progressed, notable progressions in equipment, powder materials, and process parameters ensued, broadening the scope of cold spray applications to encompass coating deposition across diverse industries, surpassing its initial purpose of repairs.

Cold spraying is a distinctive thermal spray technique that functions at comparably lower temperatures, ensuring the preservation of coating material integrity. It involves accelerating solid powder particles to high velocities using a high-pressure gas, usually nitrogen or helium [34], [35]. These particles are propelled towards the substrate, where they collide with and adhere to the surface. The kinetic energy carried by the particles upon impact leads to plastic deformation and interlocking between the powder particles and the substrate surface. This process culminates in the creation of a coherent and strongly bonded coating [34], [35]. Unlike other methods, cold spraying operates at temperatures below the melting point of the coating material. Consequently, there is minimal heat transfer to the substrate, preserving the integrity of the coating material and minimizing the potential for thermal damage [34], [35].

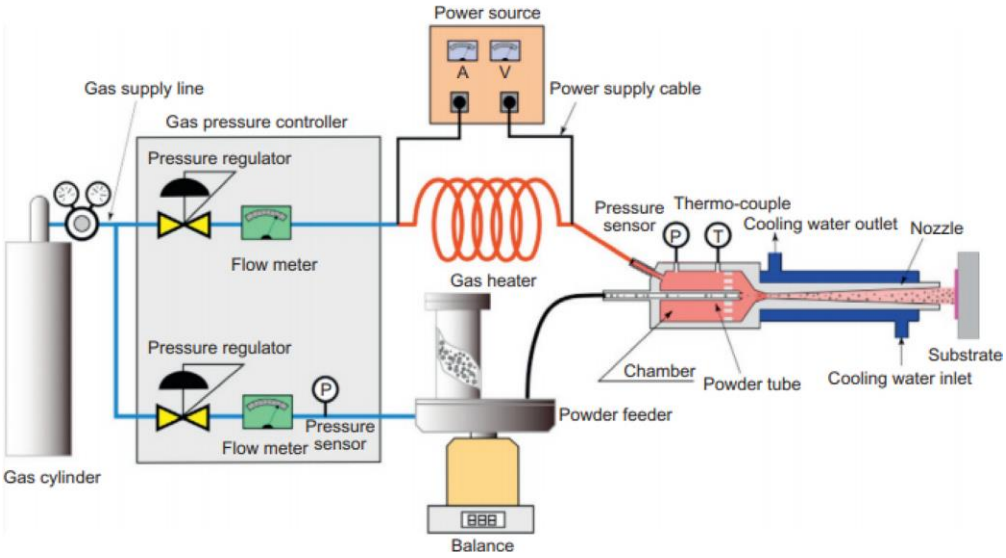

Figure 2-4 A schematic components of cold spray, adapted from Singh et al [36]

Cold spraying provides several advantages over traditional thermal spray processes. By operating at lower temperatures, cold spraying effectively prevents oxidation, phase transformations, and thermal degradation of the coating materials. This preservation of their original properties encompasses mechanical strength, chemical composition, and microstructure [34], [35]. Furthermore, cold spraying exhibits remarkable versatility in depositing a wide range of materials, including metals [37], alloys [38]–[40], ceramics [41]–[43], composites [44], [45], and even certain polymers [46], [47]. This adaptability allows for the creation of coatings with tailored properties to meet specific application requirements. The resulting coatings from cold spraying are dense, well-bonded, and exhibit minimal porosity [34], [35]. The high kinetic energy of the particles involved in the process promotes strong interparticle bonding, leading to coatings with exceptional adhesion and excellent mechanical properties [34], [35]. Moreover, the low-temperature nature of cold spraying significantly reduces oxide formation, resulting in coatings with minimal oxidation levels. This enhances the corrosion resistance and stability of the coatings.

Cold spraying demonstrates distinct process features. The inherently low temperatures involved in cold spraying make it well-suited for coating heat-sensitive materials like polymers and specific alloys, thereby minimizing thermal stress on the substrate. Typically, cold spraying achieves remarkable deposition efficiencies, often surpassing 90%, meaning that a substantial portion of the sprayed particles adheres to the substrate, resulting in minimal material wastage [34], [35]. The thickness of

cold-sprayed coatings can be finely regulated by adjusting process parameters such as gas pressure, powder feed rate, and spraying distance. This level of control enables precise management of coating thicknesses, ranging from a few micrometers to several millimeters.

Spraying methods are widely utilized in different industries owing to their adaptability and ability to produce top-notch coatings. They find notable applications in various sectors such as aerospace (utilizing plasma-sprayed thermal barrier coatings), automotive (applying wear-resistant coatings), power generation (providing erosion resistance, corrosion protection, and thermal barrier properties), electronics (offering insulation, electrical conductivity, and thermal management), biomedical (promoting osseointegration and reducing wear and corrosion), and oil and gas (ensuring corrosion protection and wear resistance).

2.1.3 Laser Cladding

Laser cladding, also referred to as laser metal deposition (LMD) or laser powder deposition (LPD), brought out in 1960s, is an additive manufacturing process where a laser beam is employed to bond a powdered coating material onto a substrate [48]. This section offers a summary of the fundamental principles, advantages, process characteristics, and applications of laser cladding.

In laser cladding, a concentrated high-power laser beam is directed onto the surface of the substrate. The laser's intense heat melts both the top layer of the substrate and the powdered coating material [48], [49]. This powdered coating material is introduced into the melted pool that forms due to the laser beam. As the molten powder combines with the molten substrate material, a metallurgical bond is formed when the mixture solidifies [48], [49]. The computer-aided design (CAD) software controls the laser beam and the deposition of the powder, enabling precise layer-by-layer construction of the desired coating shape [48]. The localized melting and solidification process establishes a strong metallurgical bond between the coating material and the substrate, resulting in exceptional adhesion and mechanical properties.

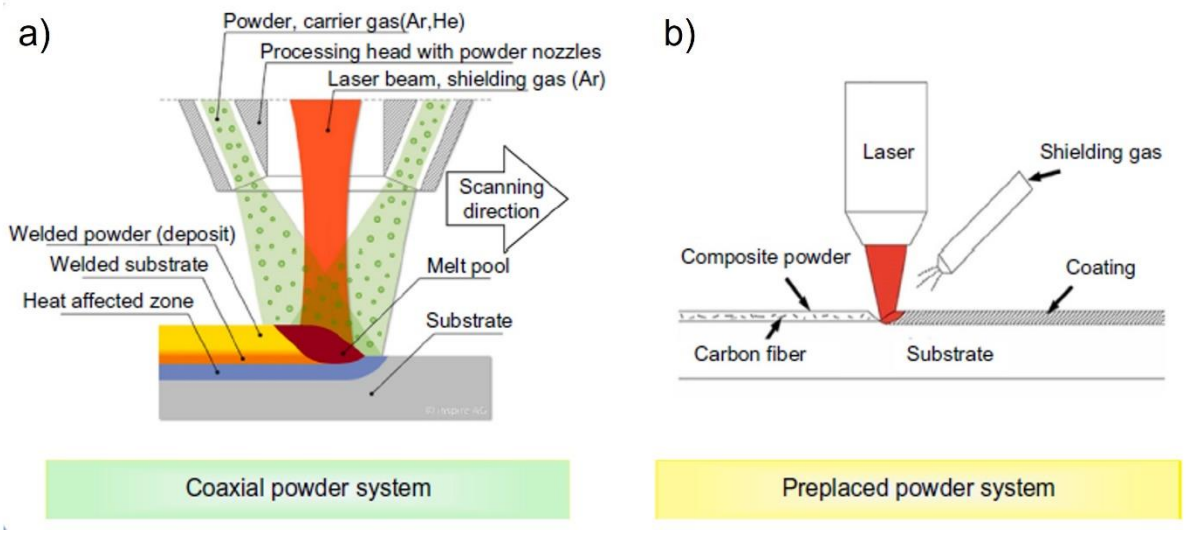

Figure 2-5 Schematic diagrams of laser cladding technique with a) coaxial powder system and b) preplaced powder system adapted from Zhu et al [50]

Laser cladding presents several advantages when compared to traditional coating processes. It enables precise control over coating thickness, composition, and geometry, allowing for customized coatings with specific properties [48], [49]. The localized heating from the laser beam limits heat transfer to the substrate, minimizing the risk of thermal distortion or damage [48], [49]. Dilution between the coating material and the substrate is kept to a minimum in laser cladding, preserving the original properties of both materials [48], [49]. The technique supports a wide range of coating materials, including alloys [51], [52], ceramics [53], [54], and composites [55], [56], offering flexibility in material selection for various applications. The focused laser beam enables high precision and resolution, making laser cladding suitable for intricate and complex coating patterns. Moreover, the near-net-shape capabilities of laser cladding reduce the need for extensive post-processing, resulting in time and cost savings [57], [58].

Laser cladding demonstrates distinctive process features that contribute to its effectiveness. It enables high deposition rates, facilitating efficient coating production and reducing manufacturing time [48], [49]. The resulting coatings from laser cladding exhibit outstanding quality, with low porosity, high density, and a robust metallurgical bond with the substrate [48], [49]. The rapid solidification process during laser cladding produces a refined microstructure in the coating material, enhancing its mechanical properties. Additionally, the localized heating of the laser beam limits the heat-affected

zone, minimizing the potential for thermal damage to the substrate [48], [49].

Laser cladding is gaining traction in diverse industries such as aerospace (for repair and refurbishment purposes) [59], oil and gas (to enhance wear resistance, corrosion protection, and restore dimensions) [60], [61], as well as medical and dental (to improve biocompatibility and durability) [62]–[64].

Laser cladding is a promising technology that is gaining traction across multiple industries due to its precision, versatility, and ability to produce high-quality coatings. With the capability to create intricate shapes and functional surfaces, this advanced manufacturing technique offers new opportunities for diverse applications and component refurbishment.

2.2 Electrospark Deposition

ESD is a distinctive method for modifying surfaces that harnesses the power of high-energy electrical discharges to deposit metallic materials onto substrates. This comprehensive literature review aims to offer a detailed analysis of ESD, encompassing its underlying principles, process parameters, material considerations, applications, and recent advancements. Through a thorough examination of various research articles, patents, and industry reports, this review aims to shed light on the notable contributions and recent progress made in the field of ESD.

The roots of ESD can be traced back to the early 1900s with the introduction of electric spark machining, which involved the use of high-voltage discharges to remove material from metal surfaces. Researchers soon realized that these electrical discharges not only eroded material but also caused localized melting and fusion on the surface. In the 1960s and 1970s, scientists began to explore the potential of utilizing electrical discharges to deposit material onto surfaces, giving rise to the concept of ESD for coating creation and substrate property modification [65], [66].

The ESD process involved the use of a power supply to generate high-voltage electrical pulses discharged across a small gap between an electrode and the substrate. The electrical discharges vaporized the electrode material, which then condensed and solidified onto the substrate, forming a coating. Initially, the primary application of ESD was for repairing and restoring worn or damaged parts [65], [66]. It proved effective in the localized material buildup and the restoration of component dimensions and functionality.

Advancements in power supply technology, electrode design, and process control have significantly improved ESD over time. Researchers developed methods to control electrical parameters such as pulse duration, frequency, and voltage, enabling better control over coating characteristics. New electrode materials and compositions were explored to achieve desired coating properties.

In recent years, ESD has gained recognition as a valuable surface engineering technique across various industries. Its ability to deposit coatings with tailored properties, including enhanced hardness, wear resistance, and corrosion resistance, has made it appealing for applications in the automotive, aerospace, energy, and tooling industries.

Continuing research and development endeavors aim to enhance and broaden the capabilities of ESD. The focus is on fine-tuning process parameters, gaining deeper insights into the underlying mechanisms, and investigating novel electrode materials and coating compositions. These advancements seek to further enhance coating quality, adhesion, and control over coating thickness. The goal is to establish ESD as a versatile and dependable technique for surface modification.

2.2.1 ESD Mechanism and Steps

ESD enables precise control over the deposition process. Process parameters such as voltage, current, pulse duration, electrode material, and electrode geometry can be adjusted to achieve the desired deposition characteristics, including layer thickness, composition, and surface roughness [67].

The workpiece surface is prepared through a thorough cleaning process that involves the removal of contaminants, grease, and oxide layers. This preparation ensures effective mixing and bonding between the deposited and substrate material. The electrode is positioned at a precise distance from the workpiece surface, typically within a range of a few tenths of a millimeter. The specific gap distance depends on the particular application and desired deposition characteristics.

ESD encompasses various stages, including the choice of the electrode, tool geometry, and electrical parameters, as part of the overall process [67], [68]. Selecting the appropriate electrode material is a critical aspect of ESD. The electrode material must be compatible with the workpiece material and possess favorable deposition properties, such as high electrical conductivity, a high melting point, and chemical stability [65], [67], [68]. The shape of the electrode can differ based on the specific demands of the application. It may take on cylindrical, conical, spherical, or customized designs to achieve the

desired deposition pattern or address repair requirements [65]–[68]. Tool geometry influences aspects such as deposition precision, material transfer, and process stability [65]–[68].

To initiate the process, a high-voltage electrical potential is applied across the electrode and the workpiece, leading to an electrical discharge. The electrical discharge can be generated using methods such as capacitor discharge, pulsed power supply, or other suitable techniques [67], [68]. This discharge creates a plasma channel, leading to the vaporization and ionization of the electrode and workpiece materials, and generates intense heat, creating a localized molten pool at the interface between the electrode and the workpiece.

The electrical parameters are vital in governing the ESD process. These parameters encompass voltage, current, pulse duration, and frequency. They dictate the strength of electrical discharges, heat production, material transfer, and deposition characteristics. The choice of electrical parameters relies on factors like the workpiece material, desired deposition properties, and the specific equipment utilized. Typically, a short-duration pulse with high voltage is employed to generate a controlled spark and localized melting, and a portion of the molten droplets from the electrode transfers to the workpiece surface, which are propelled towards the workpiece due to the electromagnetic forces generated in the process [67], [68]. The transfer of material is also influenced by factors like the electrode geometry, and properties of the molten material. This rapid solidification results in a metallurgical bond between the deposited material and the substrate, minimizing HAZ and workpiece distortion [67], [68]. A sketch of the ESD process is shown in Fig. 2-6.

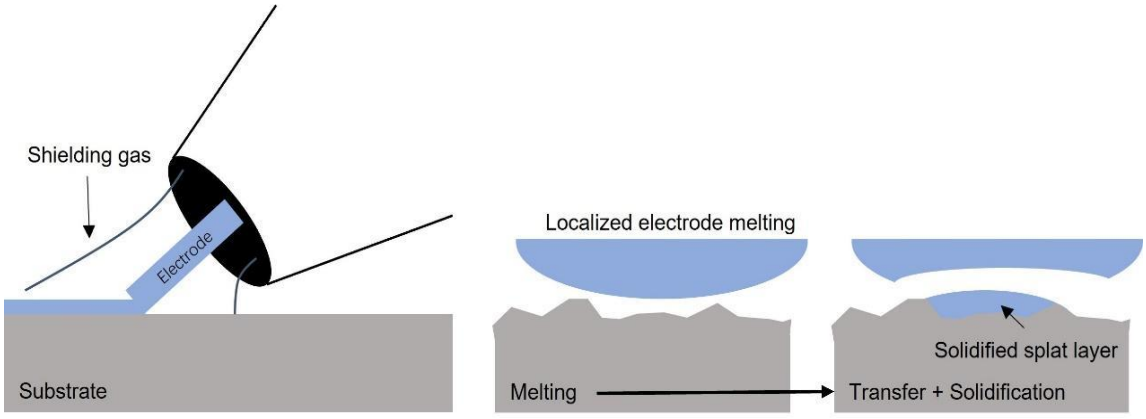

Figure 2-6 Sketch of the ESD process

Following deposition, the surface may undergo additional treatments such as machining, grinding, or polishing to achieve the desired surface roughness, dimensional accuracy, or final shape.

During the deposition process, the previous splat layer becomes the substrate of the next splats, and the solid-liquid interface moves from the base metal to the deposition surface as the solidification of the splats [69]. During this process, the cellular subgrains are formed at the outer surface of the deposition along the deposition direction. It is expected that the fine cellular structure (subgrain diameter) will coarsen as the continuous heating of the system. From the high magnification images, the differences in the size of the subgrain can be distinguished, which is due to the different thermal treatments that undergo [69]. Fig. 2-7 shows the mechanism of grain/subgrain growth and the subgrain diameter and splat thickness are represented by 2-headed arrows.

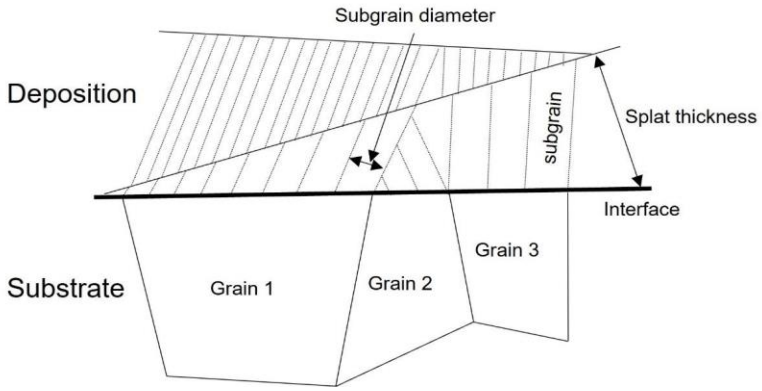

Figure 2-7 Solidification mechanism of Inconel 718 deposition using ESD

The relationship between the subgrain size and the splat thickness, and the microhardness was also studied [69]. The thicker the splat, the lower the cooling rate, which would produce the higher sized subgrain, and result in a lower microhardness.

2.2.2 Effect of ESD Parameters

The process parameters employed in ESD are instrumental in determining the characteristics of the deposition and overall process performance. The discharge voltage directly influences the energy input into the ESD process. Higher voltages result in greater discharge energies, leading to increased material vaporization and plasma temperature. This can enhance material transfer and deposition efficiency [70]–[72]. However, excessively high voltages can result in excessive material loss, elevated electrode erosion, and potential arcing or substrate damage.

The discharge current determines the rate at which energy is delivered during each discharge pulse. Higher currents typically yield larger plasma volumes, increased material vaporization, and higher deposition rates [70]–[72]. However, excessively high currents can lead to electrode overheating, increased material loss, and reduced process control.

The discharge frequency refers to the rate at which discharge pulses are applied during the ESD process. Higher frequencies generally enable faster material deposition due to increased discharge repetition [70]–[72]. However, the selection of frequency should be balanced with process stability, electrode cooling, and material transfer efficiency. Lower frequencies may be preferred in certain applications to ensure better control of the deposition process.

The pulse duration represents the duration for which the discharge current is applied during each discharge pulse, and it can be adjusted through capacitance control. Longer pulse durations provide higher energy input, resulting in increased material vaporization and plasma temperatures [70]–[72]. This can improve deposition efficiency and promote stronger bonding between the deposited material and the substrate. Nevertheless, excessively long pulse durations can cause excessive heating, electrode erosion, and reduced control over the deposition process.

The pulse energy and the power input can be calculated using the following equation [70], [73]:

$$E = \frac{1}{2}CV^2 \quad (1)$$

$$P = E \times f = \frac{1}{2}CV^2 \times f \quad (2)$$

The unit of the parameters are capacitance (C) [μF], voltage (V) [V], and frequency (f) [Hz].

The electrode gap refers to the distance between the electrode and the substrate surface, which can be altered by applying force [74], [75]. The electrode gap affects the distribution of the electric field, discharge stability, and material transfer efficiency. Smaller electrode gaps typically lead to more localized discharges, higher energy density, and improved material transfer. However, the adjustment of electrode gap should consider factors such as the desired deposition thickness, and cooling effectiveness.

2.2.3 Applications of ESD

The use of ESD provides an economical method for repairing valuable components. Instead of undergoing the costly and time-consuming process of replacing the entire component, ESD allows for targeted repairs, resulting in reduced downtime and cost savings. This is especially advantageous for crucial components in industries like aerospace, power generation, and automotive, where the expenses associated with component replacement are significant.

Surface modification. ESD is commonly employed to alter the surface morphology of workpieces, specifically for coating purposes. This practice is particularly prevalent in industrial equipment, such as the production of TiC coatings on copper electrodes in RSW, as illustrated in Fig. 2-8a and 2-8b. This choice stems from the fact that copper undergoes plastic deformation during repeated heating processes, leading to a reduction in its durability. Following the manufacture of TiC coatings, the decreased conductivity serves to enhance the heat generated during the RSW process (allowing for the use of lower parameters). Moreover, the higher plasticity of TiC prevents copper deformation and extends the electrode's durability, as depicted in Fig. 2-8c and 2-8d.

Figure 2-8 Photo of a) uncoated and b) coated RSW copper electrodes; and the c) uncoated and d) coated electrodes that undergo multiple welding, adapted from [76]

Repair. ESD is also frequently employed for the repair of surface damage on metal workpieces. For instance, WC coatings are applied using ESD to address the restoration requirements of rusted journal shaft surfaces, as shown in Fig. 2-9a and 2-9b. ESD is also utilized for structural repairs, such as in the case of turbine blades damaged due to thermal fatigue, as illustrated in Fig. 2-10. Fig. 2-10a presents a photograph of the damaged component, while Fig.2-10b depicts the removal of the damaged section followed by structural repair. The repaired component is shown in Fig. 2-10c.

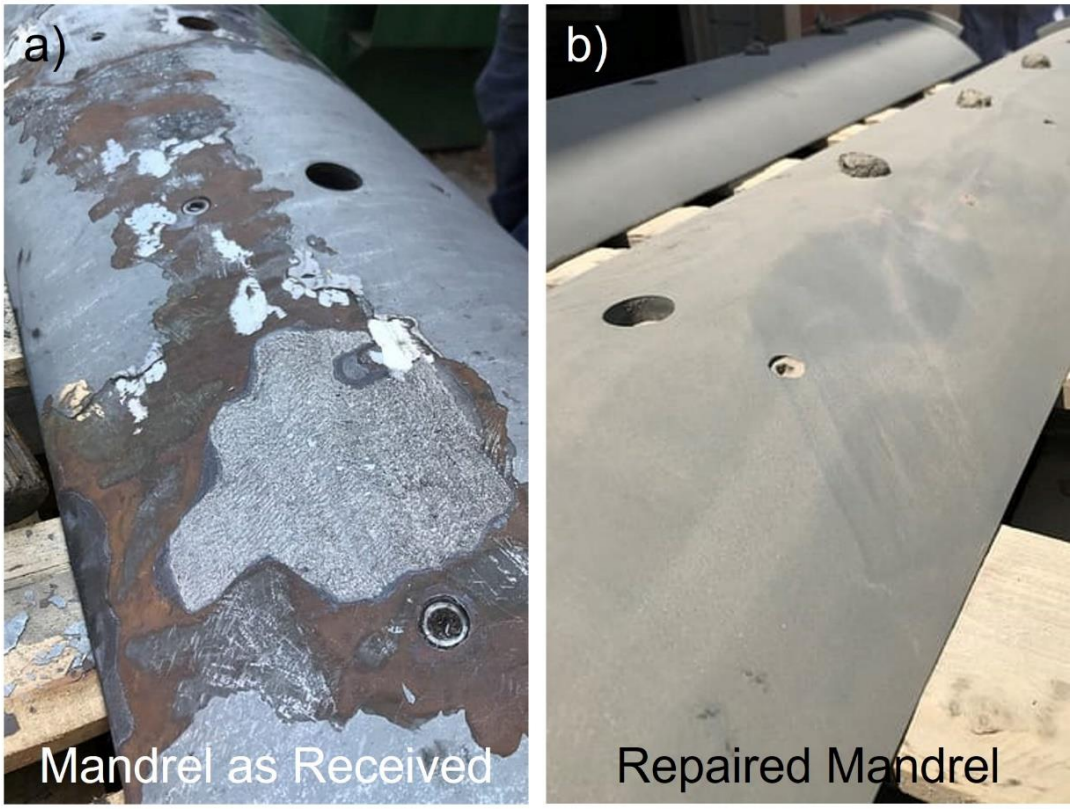

Figure 2-9 Repair of rust mandrel a) before and b) after WC ESD coating, adapted from [76]

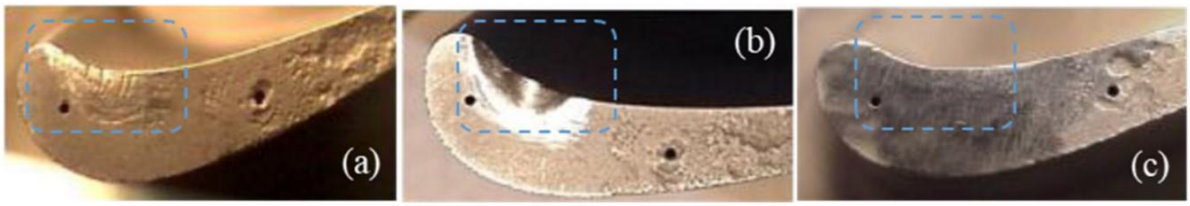

Figure 2-10 Photo of a) thermal fatigue damaged turbine blade; b) grinding off the damaged part; and c) the structural repair of turbine blade, adapted from Johnson [77] **and Barile et al** [78]

ESD with powder feedstock. Unlike the conventional ESD technique, Zhao et al. [79] used a planar electrode with ultrasonic vibration to fabricate NiCrSiB coating on a carbon steel ASTM1045 substrate. The NiCrSiB powder was glued to one side of the copper tape, and then the other side of the copper tape was glued to the planar electrode as shown in Fig. 2-7. After touching the substrate surface with ultrasonic vibration when the power was turned on, the electric spark melted the powder on the tape, fused it, and transferred and solidified it onto the substrate. The etched coating exhibited columnar dendritic grains that grew in a direction perpendicular to the substrate surface, with primary dendrite arm spaces less than 1 μm and secondary dendrite arm spaces less than 0.2 μm. The microhardness of the coating was measured to be 680 Hv, much higher than the substrate's 329 Hv. The increase in coating hardness was due to two main factors, one being the generation of intermetallic compounds, chromium carbide, and boron precipitates, and the other being the refinement of the grains. In addition, a wear test was performed, and the wear rate was 5.71×10-7mm2/N, which is nearly a fourfold reduction with respect to the substrate.

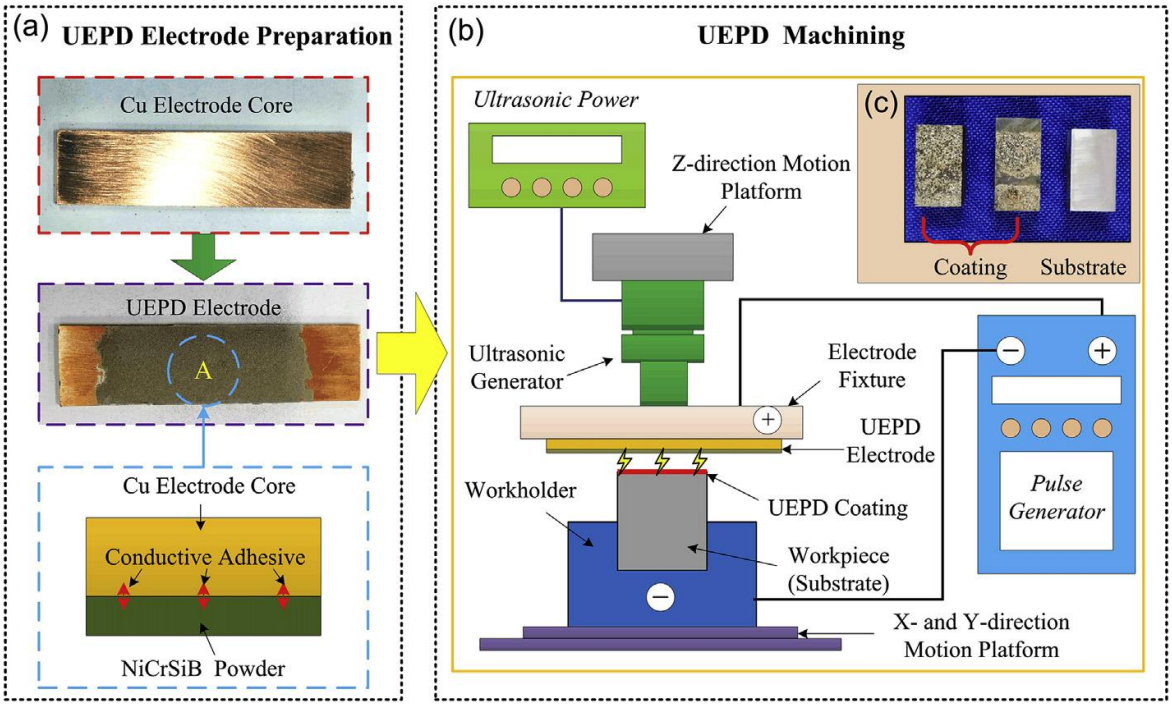

Figure 2-11 Schematic ultrasonic electrospark powder deposition (ESPD) diagram, adapted from Zhao et al [79]

Burkov et al. [80] used another ESD technique to fabricate the coating in Ti6Al4V using metal powders as raw material, the the sketch shown in Fig. 2-8. A mixture of monometallic powders Ti, Ni, Zr, Mo, Al, and alloy powders Ti3Al + 10% C is poured into a metal container, and then the substrate workpiece is stretched into the container and connected to the circuit respectively, and the contact of the mixed powder in the container acts as a circuit between the container and the workpiece, while the electric spark formed during the contact causes the powder to melt, fuse, and transfer and solidify to the substrate to form the coating as shown in the figure. After sufficient deposition, AlNi2Ti, MoNi4 and NiTi intermetallic compounds were observed in the coating. Microhardness of 765 Hv, surface roughness Ra=31, and wear rate from 2.2*10-6g/Nm of the substrate material to 4.5*10-7g/Nm of the coating were also measured, which indicates that the coating can protect the substrate effectively from adhesive wear.

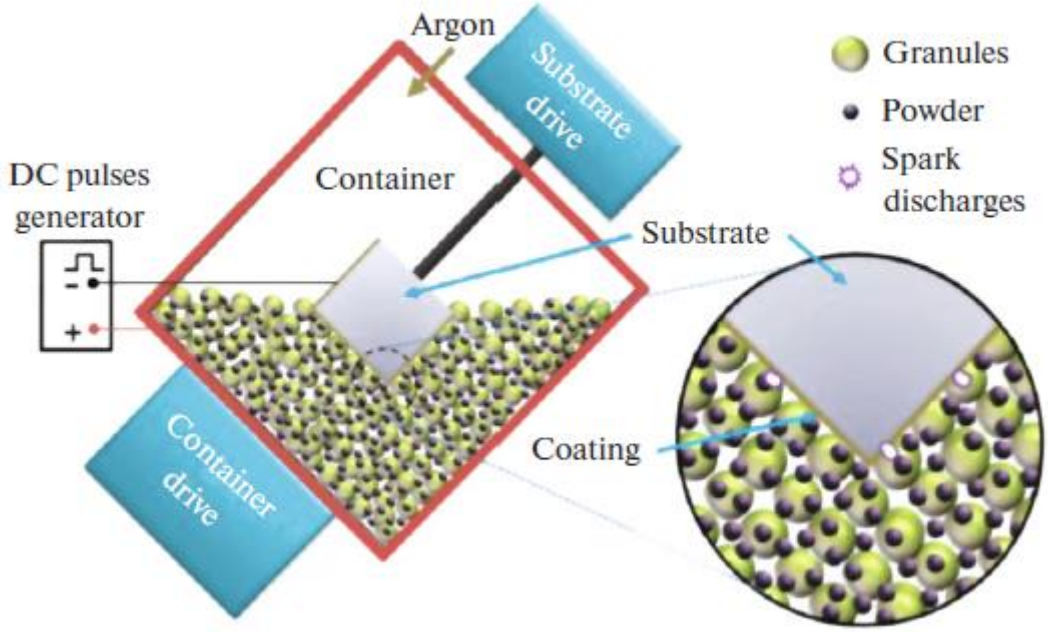

Figure 2-12 Schematic coating deposition by ESA in granule medium, adapted from Burkov et al [81]

2.3 Coating Materials for ESD

A variety of metallic materials are frequently utilized in ESD, each possessing distinct properties and advantages tailored for specific applications. This section offers a comprehensive overview of the metallic materials frequently employed in ESD.

Nickel-based alloys, such as Inconel and Hastelloy [82]–[84], find extensive application in environments characterized by high temperatures and corrosive conditions. These alloys possess exceptional resistance to oxidation, heat, and chemical corrosion, and enhance fatigue life, rendering them suitable for a range of industries including gas turbines, chemical processing, and power generation.

Aluminum and its alloys [85], [86] provide a favorable balance of strength, low weight, and resistance to corrosion. They are frequently employed in ESD for applications that demand lightweight coatings with efficient thermal conductivity. Examples of such applications include heat exchangers, electronic components, and aerospace structures.

Ceramics, such as WC [87], [88], are often produced to elevate the surface roughness, and resistance to wear and corrosion of the surface of the workpieces. TiC [89] can be coated on resistance spot welding (RSW) copper electrode to prolong the working life of the cap.

Cobalt-based alloys, exemplified by Stellite [90], are renowned for their remarkable ability to withstand wear, exhibit high strength at elevated temperatures, and resist corrosion. These alloys are extensively utilized in applications where severe wear is prevalent, including valve seats, cutting tools, and components requiring exceptional wear resistance.

It is important to emphasize that when choosing metallic materials for ESD, careful consideration is given to the desired coating properties, application requirements, and compatibility with the substrate material. Factors such as mechanical properties, corrosion resistance, thermal conductivity, electrical conductivity, and cost-effectiveness should be taken into account when making the material selection.

2.3.1 Inconel 718 Superalloy by ESD

Ni-base high-temperature alloy materials can work for a long time at temperatures above 600°C and under certain stresses [91]. They are mainly used in the fields of aviation, aerospace, petroleum,

chemical, naval, electric power, automobile, etc. [92]. High-temperature alloy industry is a technology-intensive industry, and its production process is characterized by high technical content and great difficulty in development. The research and development of a new type of high-temperature alloy products not only requires the achievement of technical conditions, but also must go through mass production and master the production process, which requires the accumulation of more industry experience to succeed, and the technical barriers and industry barriers are high. In addition, the military field is strict and long-period verification of products, once passed the verification will not easily change the supplier, the customer barriers are high.

Inconel 718 high-temperature alloy is a Ni-Cr-Fe-based deformation alloy developed by the United States in 1950s and patented by International Nickel Corporation. It has become one of the most widely used high-temperature alloys (accounting for 40%-50% of the world's total production of high-temperature alloys) because of its good high-temperature stability, oxidation resistance and welding properties, excellent fatigue, and creep resistance [93]. As an aero-engine structural material, Inconel 718 alloy is subject to the combined effects of high temperature, stress and corrosion during service, and its working condition is subject to fatigue-creep interaction, and the service life is closely related to the evolution of the microstructure of the alloy under service conditions, especially in long-term service above 650 ℃, the primary strengthening phase γ” phase in the alloy will be coarsened or transformed to δ phase [94]. It is important to elucidate the precipitation and evolution of the precipitated phase during service to further extend the service life of Inconel 718 alloy. The crystal structures of Ni matrix and strengthening phases are shown in Fig. 2-13. The chemical composition and phase information are shown in Table 2-1 and Table 2-2, respectively.

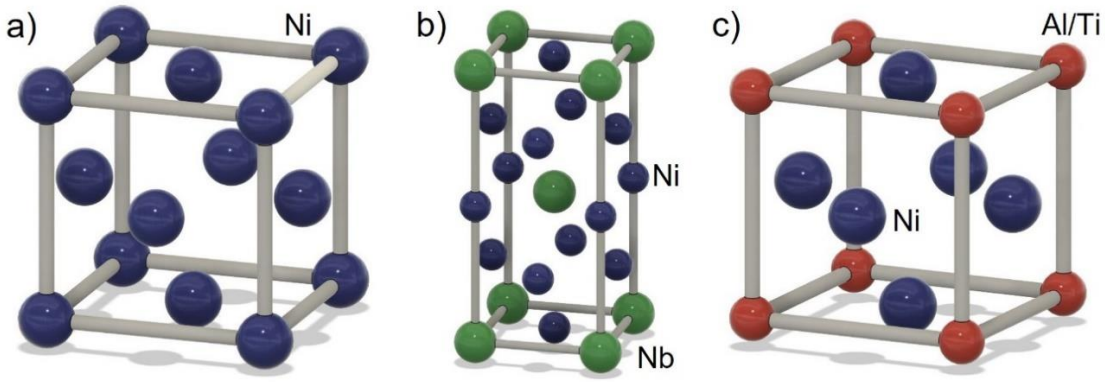

Figure 2-13 The lattice structure of the phases and the precipitates in Ni-base superalloy. They are a) FCC Ni matrix, b) orthogonal Ni3Nb, and c) FCC Ni3(Al, Ti, respectively

Table 2-1 Chemical composition of Inconel 718

Ni	Fe	Cr	Nb	Mo	Al	Ti	C
50-55	Bal.	17-21	4.4-5.4	2.8-3.3	0.2-0.8	0.65-1.15	<0.08

Table 2-2 Phases in the Inconel 718 along with chemical formula, crystal structure, and lattice parameters [95]

Phase	Formula	Crystal structure	Lattice constant (nm)
γ	-	FCC	A=0.36
γ’	Ni_3(Al, Ti)	FCC	A=0.35
γ”	Ni_3Nb	BCT	a=0.36, c=0.74
δ	Ni_3Nb	Orthogonal	a=0.51, b=0.42, c=0.45
MC	(Nb, Ti)C	FCC	a=0.45
Laves	$(Ni, Cr, Fe)_2$(Nb, Mo, Ti)	Hexagonal	a=0.48, c=0.78

Besides the primary strengthening phase γ”, the secondary strengthening phase γ’ can also improve the properties of the material. The former has a 60 nm by 10 nm discs-shaped precipitates, which has a large lattice mismatch between the body-centered tetragonal (BCT) and the FCC Ni-matrix (γ), which results in a high coherency strain that strengthens the material. The latter has an ordered FCC crystal structure, with a similar lattice parameter with γ matrix, which is stable between 600 to 850 ℃. Whereas the low Al and Ti compositions decide that the γ’ only occupies a low fraction of the strengthening phases. The high niobium composition results in the great performance of Inconel 718 at high

temperatures under 650 [88, 90]. The carbide and Laves phase are considered detrimental phases in the material [91, 92], as they trap the Nb which prevent the formation of γ", and inhibit grain growth, which can initiate the crack and make the material brittle [97].

The phase evolution analysis during the manufacture of Inconel 718 has been meticulously studied, but the phase evolution after some special treatments has only been reported to a small extent. In what follows, the ESD technique has been used to prepare the coating of Inconel 718, its microstructure and phase evolution was studied, and the internal details after heat treatment were analyzed.

The pulse energy and the frequency play an important role in the ESD process as introduced in Section 2.2.2. The higher pulse energy and power input will result in a higher heat input, and during each sparking, more electrode material will be molten and transfer onto the substrate, as a result, a thicker splat can be formed for each scan of the electrode, and then lead to a higher deposition rate or thick coating [98]. The shape of the individual splat is shown in Fig.2-14.

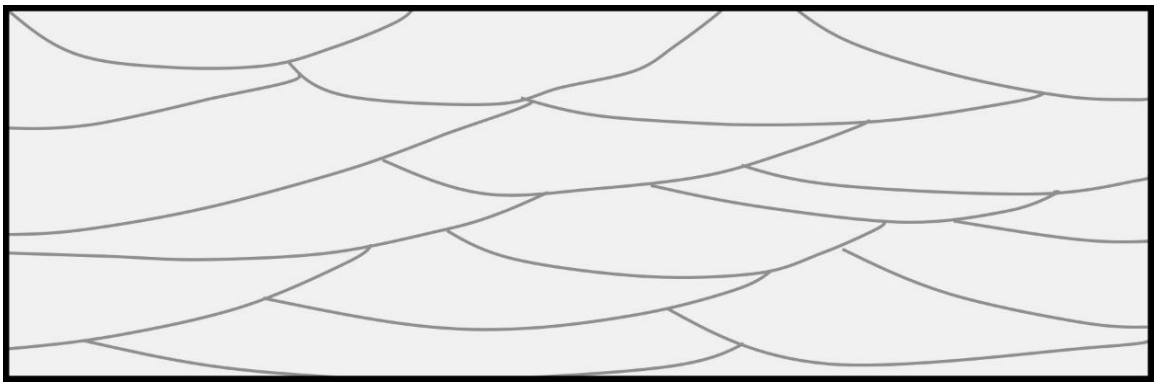

Figure 2-14 A sketch of the individual splat is thicker in the middle, and thinner at the sides

A study has shown that the thickness of the splats affects the microhardness as well. The thicker the splat (higher deposition rate), the lower the microhardness, and a detailed analysis will be presented.

Besides the deposition rate, another primary result is also important, which is the cavities, or defects, and the most common defect is the voids. The voids in deposition techniques are mainly due to the lack of fusion (LOF) [98]. In the ESD technique, the lack of fusion is mainly because of (1) the lack of transfer of the material from the electrode to the substrate and (2) the temperature of the sparking is only slightly higher than the melting temperature of the electrode material, and due to the high viscosity

of the molten material, it cannot fill into the voids during the transfer and before the solidification [98]. The two statements above suggest that the lack of fusion is mainly due to the low pulse energy, as the lower the pulse energy, the lower the material transfer, and the lower the sparking temperature. However, the observation shows differently, the volume fraction of the voids increased with the increasing pulse energy, and the size of the voids also increase with the increasing pulse energy, which suggests that there are other key factors that must be considered when analyzing the formation of the voids [98].

The geometry of the voids is mainly located at the interface of the splats. This is because, during the deposition, the uneven contact between the electrode and the substrate could result in the formation of a gap or valley between the splats at the same layer. Due to the rapid solidification of the deposition layer, the molten material cannot fill the voids. When using high pulse energy, the thicker splats will form the deeper valley, and therefore, a larger size and larger fraction of the voids can be observed. It can also be observed by roughness measurement. The degree of roughness increases with the increasing pulse energy. The higher the pulse energy, the higher the number of unidentified areas that represent the valleys formed at the surface during the deposition [98].

Another type of defect is the cracks, which are mainly located at the middle of the splat. The shape of the splats shows that the side of the splats is thinner than that of the middle region, which in turn leads to a different solidification rate, as a result, there will be a thermal gradient inside the individual splat that causes the residual stresses inside the splats during the solidification. Most of the splats are parallel to the substrate, therefore the direction of the residual stresses is also parallel to the substrate, which generates cracks that are perpendicular to the substrate [98].

These observations are true for almost all the materials that can be used for ESD procession. An efficient buildup can be achieved due to the high ductility of the Inconel 718, there is almost no limit for this material. Whereas for other materials such as Tungsten Carbide, the thickness can only reach 30 μm.

The phases present in the deposition layer are characterized by TEM analysis [99], which shows the columnar cell γ matrix in the Inconel 718 Ni-superalloy system. The columnar cells have an elongated direction along the deposition direction, which is also the shape of the subgrain in the deposition layer. There is no reflection from the strengthening phases γ', γ", or δ precipitate in as-deposited samples, but

the Laves phase and the carbide can be observed at the boundary of the subgrains, which has a chemical composition of (Ni, Cr, Fe)$_2$(Nb, Mo, Ti) and NbC respectively that are confirmed from the EDX analysis. Niobium is present in both Laves phase and carbide, which shows that these two precipitates are harmful to the system, as they trap the niobium and further prevent the formation of the primary strengthening phase γ" phase, with a chemical composition of Ni_3Nb. In addition, the nanosized oxide precipitate can also be observed in the deposition layer, according to the EDX analysis, the oxide is mainly aluminum and titanium oxide, which trap the aluminum and titanium that prevents the formation of the secondary strengthening phase γ' phase with a composition of Ni_3(Al, Ti) [99].

The hardness of the deposition layer of Inconel 718 is mainly affected by the presence of the strengthening phases [99]. As there are no strengthening phases in as-deposited layers, the hardness is then mainly due to the presence of the oxide, the smaller grain size, as well as the residual stresses from the deposition process. The microhardness of the deposition layer before and after the heat treatment does not have many differences, which shows that the microstructure of the deposition layer does not have much change. Interestingly, from the electron beam welding (EBW) of the Inconel 718, the grain size in the fusion zone increases after the heat treatment, which contains the Laves phase and carbide, with no strengthening phases and δ precipitates. Since the EBW was performed under an oxygen-free environment, there is no oxide present in the fusion zone. Comparing the results from both techniques, the oxide can also inhibit the grain growth in deposited Inconel 718, and the degree of the inhibition of the grain growth of the oxide is higher than that of the Laves phase and the carbide.

To determine the properties of the strengthened Inconel 718, The strengthening phases γ' and γ" were then detected after the full heat treatment (FHT). No Laves phase is observed [99], and the microhardness, yield strength, and ultimate strength increase evidently.

In addition, Pablo et al [84] found that the peening process also plays an important role during the deposition. The hammer peening (HP) can reduce the surface roughness efficiently and improve the external properties of the base metal. The microhardness after the hammer peening shows a great improvement. The fatigue tests show an effective improvement after hammer peened (ESD + HP), and direct aged (DA) (ESD + HP + DA).

2.3.2 High Entropy Alloy Coating

High entropy alloys (HEAs) are a promising group of materials known for their remarkable mechanical and physical properties. ESD is a surface modification method that provides distinct benefits for coating purposes. This literature review seeks to present a thorough examination of the research conducted on high entropy alloy coatings manufactured via ESD. The review encompasses a summary of the principal discoveries, methodologies employed, and performance attributes of HEA coatings, emphasizing their potential applications and avenues for future exploration.

Thermodynamic Stability. Alloys have been utilized for thousands of years by adding elements to materials to alter the properties of pure materials. Copper was added to silver to harden the material since pure silver is too soft. Chromium and carbon were added to iron to obtain the properties of corrosion resistance and higher strength, respectively. The examples above are adding a small number of secondary elements into a primary element, this strategy greatly limits the possibilities of combination of elements, but for HEA, there is less concept of the primary and secondary element, which leads the number of combinations will increase dramatically, i.e. multi-principal element alloys (MPEAs), but minor elements can be considered to alter the properties of materials, which can also increase the number of combinations of HEA.

HEA has several definitions based on different concepts, one is composition-based, the HEA is defined as the alloys that contains five or more elements with the same atomic fraction [5], which is then expanded as the five or more elements with an atomic fraction between 5 and 35% [5], [100], which means the same concentration is not restrictive, which is clearly understood. Another definition is entropy-based, the solid solution can be described with low entropy ($S < 0.69R$), medium entropy ($0.69R < S < 1.61R$), and high entropy ($S > 1.61R$), where R is the gas constant [101]. This definition has conceptual problems since it requires the alloys to be “liquid solution and high-temperature solid solution states where the thermal energy is sufficiently high to cause different elements to have random positions within the structure” [102]. However, the changes in temperature will affect the configurational entropy by changing the short-range order of atoms, which makes it hard to have random positions, which is a challenge to use this definition.

For a simple alloy combined with two elements A and B, the relative free energy of solid solution and intermetallic phases can be described as follows:

A + B = AB (solid solution): $\Delta G_{mix} = \Delta H_{mix} - T\Delta S_{mix}$

A + B = AB (intermetallic): $\Delta G_f = \Delta H_f - T\Delta S_f$

Where ΔG_{mix}, ΔH_{mix}, and ΔS_{mix} are Gibbs free energy, enthalpy and entropy of mixing, respectively, and ΔG_f, ΔH_f, and ΔS_f are those of formation of AB intermetallic compound. At thermodynamic equilibrium, the enthalpy of the system is 0, and the degree of negativity of free energy of the system decides the phase present in the alloy with different stoichiometry AiBj. In addition, for only solid solution, depending on ΔHmix, different atoms can order or cluster on the lattice, so the solid solution does not have to be ideal, and there might be a possibility that the system contains two solid solutions with different crystal structure, lattice parameter with different compositions. In binary-phase diagrams, the solid solution phase is usually shown near the elements, and the intermetallic phases are typically shown in between the ends.

However, the problem becomes much more complicated with the increasing number of elements in the alloy because of the possibilities of phases in the system at the same time, and the most common mixings can be shown in Fig. 2-15.

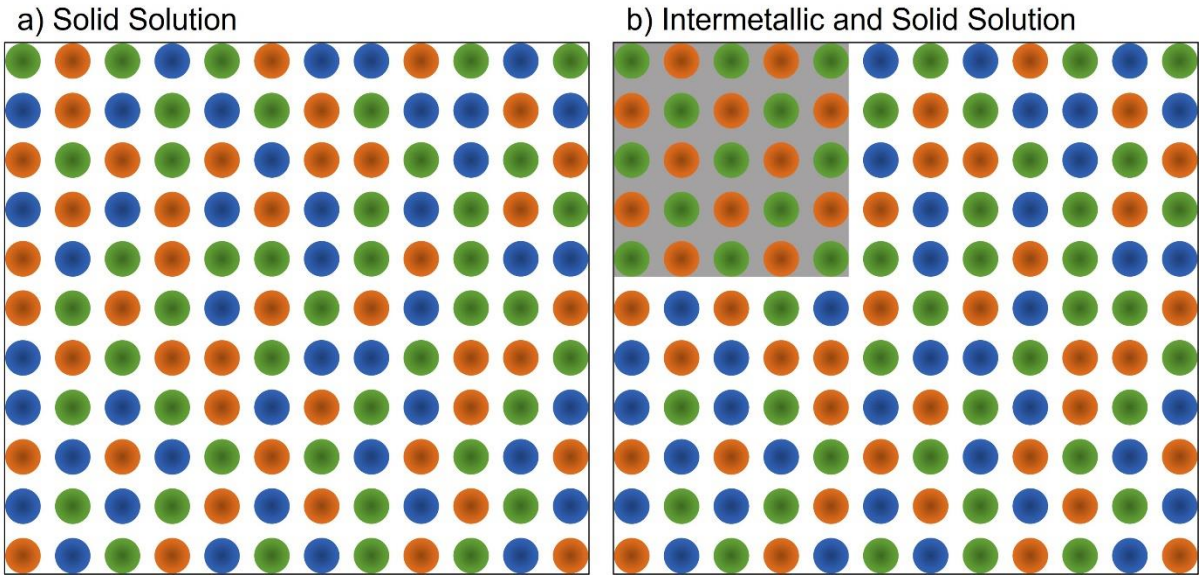

Figure 2-15 Possible mixing for three-element alloy

Yeh et al. [5] proposed that the increasing ΔS_{mix} would impede the intermetallic formation, and it is possible to substitute the intermetallic compounds with the stabilized solid solution by adding more and

more elements to the system. To simplify the problem, they considered an ideal solid solution, in the case of ΔH_{mix} is 0, and ΔS_f is 0 when the atoms in the intermetallic phase are perfectly ordered, the relative stability of two different phases depends on the degree of negativity of $-T\Delta S_{mix}$ and ΔH_f. The entropy of mixing is given by:

$$S_{mix} = -R\sum_{x_i} \ln x_i$$

Where R is gas constant and x_i is the mole fraction of element i, and entropy for equiatomic alloy ($x_1 = x_2 = x_3 = ...$) becomes:

$$\Delta S_{mix} = R\ln n$$

Where n is the number of elements. Based on the simplification, the entropy of mixing increases with the increased number of elements, which have a more negative $-T\Delta S_{mix}$ which compress the formation of intermetallic.

Major Alloy Families. More than 400 HEAs are studied to date and formed mainly by 37 elements in seven major alloy families (3d transition meta, refractory meta, light metal, lanthanide transition metal, brasses and bronzes, precious metal and interstitial compound) [103]. 85% of the HEAs are formed by 9 d transition elements (Al, Ti, V, Cr, Mn, Fe, Co, Ni, and Cu) [5], [103], [104], an example is Cantor alloy (CoCrFeMnNi) [103] that consists of five elements in these nine elements. These alloys can be regarded as an extension of superalloys and stainless steels. Superalloys have the principal elements of Ni-Cr-Co-Fe-Mo, and Fe-Cr-Ni act as principal elements in Austenitic (FCC) and duplex (FCC + BCC) hardened stainless steels, a small amount of Al, Cu, Nb, and Ti can be added to precipitation hardened stainless steels [105]. 9 refractory elements (Cr, Hf, Mo, Nb, Ta, Ti, V, W, and Zr) [106], [107] plus Al that form 29 refractory HEAs has been studied. These elements are used to produce new high-temperature structural metals, which have a wide range of melting points, density, and elastic moduli [105], which offer a large flexibility to produce materials with certain properties. For example, Cr, Nb, V, and Zr give low density, Mo, Nb, Ta, and W give high melting temperatures, and so on. Other elements in different families are also used to produce HEAs, the light metal element (Al, Be, Li, Mg, Sc, Si, Sn, Ti, and Zn) [108], [109] are used for light alloys, 4f elements (Dy, Gd, Lu, Tb, and Tm) [110] are used for single-phase, solid solution HEAs with HCP crystal structures. In addition, B [111], C [112] and N [113] can also be doped for HEAs because they would cause a significant change in microstructure and phases.

Preparation of HEAs. The technologies of preparation of HEA are shown in Table 2-3, Different forms of HEA have different methods of preparation. For bulk HEAs, the most common way to produce it is vacuum melting (e.g., $AlCoCrFeNiTi_X$) [114] and powder metallurgy method (e.g., $W_XTaTiVCr$) [115], which have the characteristics of low-temperature sintering, avoiding segregation, and high material utilization rate that is not available in the traditional casting method. Mechanical alloying methods are mainly used to prepare high-entropy alloy powder (e.g., CuNiCoZnAlTi) [116], nanocrystalline and amorphous particles with uniform composition distribution and structure can be obtained. To prepare high-entropy alloy coatings, laser cladding (e.g., $Al_{0.5}CoCrCuFeNiSi$ and $Al_{0.8}CrFeCoNiCu_{0.5}B_X$) [117], [118], thermal spraying (e.g., AlCoCrFeNi and MnCoCrFeNi) [119], and cold spraying (e.g., CoCrFeNiMn) [120] are mainly considered. As for high-entropy alloy film, plasma-based ion implantation (e.g., $AlCoCrFeNiTi_{0.2}$) [121], electrochemical deposition (e.g., AlCrFeMnNi and AlCrCuFeMnNi) [122], and magnetron sputtering (e.g., CrFeCoNi) [123] are used.

Table 2-3 Preparation technology of HEAs

Form of Alloy	Technique	Materials	Ref.
Bilk	Vacuum melting	$AlCoCrFeNiTi_X$	[114]
	Powder Metallurgy	$W_XTaTiVCr$	[115]
Powder	Mechanical Alloy	CuNiCoZnAlTi	[116]
Coating	Thermal Spray	AlCoCrFeNi	[119]
		MnCoCrFeNi	
	Cold spray	CoCrFeNiMn	[120]
	Laser Cladding	$Al_{0.5}CoCrCuFeNiSi$	[117]
		$Al_{0.8}CrFeCoNiCu_{0.5}B_X$	[118]
Film	Plasma-based Ion Implantation	$AlCoCrFeNiTi_{0.2}$	[121]
	Electrochemical Deposition	AlCrFeMnNi	[122]
		AlCrCuFeMnNi	
	Magnetron Sputtering	CrFeCoNi	[123]

HEAs Coating by Common Coating Techniques. Li et al. [118] fabricated $Al_{0.8}CrFeCoNiCu_{0.5}B_x$ coatings on aluminum alloy by laser melting with single element Al, Cr, Fe, Co, Cu, and B powders by controlling the composition of the blended powder with x being 0, 0.1, 0.2, 0.3, 0.4. The article characterized the metallographic changes at different x and measured the hardness and wear resistance.

The coating exhibits BCC1+BCC2+FCC phases when $x \leq 0.1$, while borides Cr2B and Fe2B start to form when $x \geq 0.2$. The microhardness of the coating increases from 79 Hv in the substrate to 479, 549, 613, 601, and 705 Hv with increasing boron content, which is 6-9 times that of the substrate, respectively. Meanwhile, the wear rate of the coating surface decreases with the increase of x, from 1.19×10-5 to 1.5×10-7 mm2/N, which is only 0.01%-5.43% of the wear rate of the substrate.

Ang et al. [119] fabricated AlCoCrFeNi and MnCoCrFeNi HEA coatings by plasma spraying, with corresponding powder fabricated by high purity Al, Co, Cr, Fe, Ni, and Mn powder as the feedstock, the former HEA powder has the structure of BSS, and the latter of the FCC. The study investigated the temperature, speed, and splat anatomy during spraying to obtain a higher quality coating. Regarding the exploration of microstructure, the paper analyzes the architecture, porosity network, and multiphase composition during sputtering. XRD analysis reveals that both HEAs produced coatings with predominantly FCC structure and the generation of oxide is unavoidable due to the high temperature. As for the mechanical properties, the void fraction of the coatings is less than 10%, and the microhardness of the coatings is greater than 4 GPa.

Feng et al. [120] used CoCrFeNiMn powders as feedstock to fabricate coatings by cold spray. This study investigated the optimization of the spraying parameters to obtain coatings with a porosity less than 2%. Unlike thermal spraying, no oxide was observed in the coatings by cold spraying, and no phase transformation of the material was observed. Cold spraying is performed by dynamic recrystallization to fuse the powder to obtain the coating, this process creates a high dislocation density at the particle interface, making the hardness (5.64 GPa) much higher than that of CoCrFeNiMn prepared by the casting method. After annealing treatment at 650C, the dislocations were alleviated, and the hardness decreased to 4.95 GPa.

The mentioned studies all employ powdered materials as feedstock, which impose stringent requirements on the powder characteristics in order to ensure flowability and fusion density. Furthermore, the optimization of the process to achieve high-quality coatings is inherently complex and entails adjustments of multiple parameters. In industrial applications, these processes are time-consuming and costly. Hence, there is a need to explore simpler and more intuitive coating techniques.

HEA Coating by ESD. Chandrakant et al. [124] fabricated AlCrFeCoNi coatings on AISI 410 stainless steel. BCC and a small amount of FCC structure was measured in the coating. Diffusion of elements

occurred at the interface between the coating and the substrate, which strengthened the solid solution. The coating achieved a microhardness of 907 Hv and showed good wear resistance.

Ciprian et al. [125] used ESD to fabricate high-temperature metal HEA HfNbTaTiZr coatings on 316L stainless steel to obtain a corrosion-resistant surface. The researchers obtained high quality coatings, which showed that the coatings were homogeneous and had good adhesion on the substrate. The obtained samples were subjected to electrochemical corrosion in salt water and a small corrosion rate was obtained.

Kuptsov et al. [126] fabricated CrFeNiCo(Cu) coatings on AISI420 stainless steel to protect the stainless steel for use in coastal or offshore areas. The researchers fabricated coatings with single-phase FCC structure and concluded that CrFeCoNiCu has weaker corrosion resistance in artificial seawater than CrFeCoNi. In addition, the presence of Cu caused the surface of the components to exhibit significant antimicrobial activity. The friction resistance of the surface also has a significant improvement.

2.4 Summary

This chapter provides a detailed overview of commonly used coating manufacturing technologies, including the history of thermal spray, cold spray, and laser cladding, the process of manufacturing coatings, as well as the characteristics and properties of coatings. Subsequently, the chapter introduces the mechanism, manufacturing process, and the influence of parameters on coating fabrication in the context of Electrostatic Spray Deposition (ESD), highlighting its differences from traditional techniques. Furthermore, it presents the metallographic characteristics of Inconel 718 and High Entropy Alloys (HEA), followed by an exploration of research on coating fabrication using ESD in subsequent chapters, demonstrating the flexibility and intuitiveness of ESD.

Chapter 3

Inconel 718 Buildup on Thin-wall Geometry

3.1 Introduction

Components with thin geometries are widely adopted in industrial and commercial products, such as the edges of turbine blades and pump impeller blades; but usually they are tricky to weld repair due to their small thermal mass available in those regions. Often, erosion of the part during repair occurs when there is too much heat buildup. Additive manufactured parts with lattices or thin-wall geometries that are designed to be lightweight or have high surface area can also face this challenge. The ability to repair these challenging geometries could extend the service life of these parts, especially when they experience wear, corrosion, or stress/fatigue cracking [127], as well as reducing scrap rates for parts that fail during manufacturing due to overheating and warping, cracking, and dimensional inaccuracies.

In this study, Inconel 718 was used to produce buildups of up to 8 mm on additive manufactured 17-4 stainless steel thin-walled structures with thicknesses of 0.5 and 1 mm. The quality of the deposition was investigated, which includes the deposition rate, defect type, microstructures, and microhardness when using different ESD parameters. The extent of dilution was also measured on thin walls. The HAZ size in thin geometries was also characterized. This study explored the effect of reduced thermal mass in the substrate and changing ESD process parameters to determine whether this frequently claimed cold welding process also limits the extent of substrate damage when repairing thin-wall geometries.

3.2 Materials and Methods

3.2.1 Thin-wall Manufacturing

Thin walls of 17-4 stainless steel were additive manufactured using a material extrusion method with the Markforged Metal X system. Wall thicknesses of 0.5 and 1 mm were printed by extruding a 1.85 mm diameter filament made from a mixture of metal powder, 2-4 vol.% polypropylene, and 2-6 vol.% hydrocarbon wax. The filaments are extruded into tracks with a final sintered height of 0.125 mm and a width of 0.25 mm, although they are automatically printed larger to account for shrinkage during sintering. Two and four tracks were deposited for the 0.5- and 1-mm walls, respectively, as shown in

Fig. 3-1.

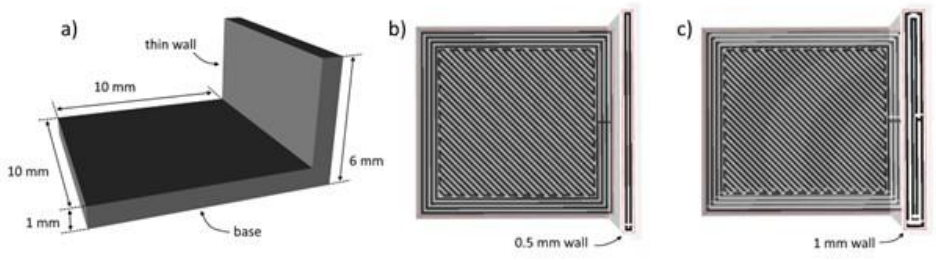

Figure 3-1 a) Thin walls used as substrate; b) scan path for 0.5 and c) 1 mm wall print

3.2.2 ESD Process

In the ESD process, consumable Inconel 718 electrodes are attached to the anode and the workpiece is connected to the cathode. In this study, only three electrical parameters were varied for comparison with a manual ESD equipment, namely capacitance (C), voltage (V), and pulse discharge frequency (f). Other parameters, such as the travel speed of the electrode, the travel method, and the contact force between the electrode and the substrate, could not be controlled quantitatively under manual conditions, and thus these engineering parameters were left to the operator to maintain as consistently as possible. During the deposition process, high purity argon was used as a shielding gas at a rate of 30L/min to protect the Inconel 718 electrode and 17-4 stainless steel substrate.

Table 3-1 Chemical composition of Inconel 718 electrode and 17-4 stainless steel substrate wt%

Material	Al	Nb	Mo	Ti	Cr	Fe	Ni	Cu
Inconel 718	0.46	5.78	2.38	1.21	20.21	18.66	51.30	-
17-4 SS	-	0.41	-	-	16.22	77.69	4.20	1.48

A manual ESD machine developed by Huys Industries was used to produce the buildup of Inconel 718 on 0.5- and 1-mm thin walls. A 1.8 mm thick rod of Inconel 718 was used as the electrode material, and the chemical composition is shown in Table 3-1. When depositing Inconel 718 on a flat surface, a parameter set of 100 μF, 80 V, 150 Hz can produce a high-quality deposition layer [79]. However, during deposition on small geometries where heat can accumulate more readily from previous material transfer events, additional process optimization is needed. Therefore, capacitance, voltage, and frequency were varied separately to investigate the effect of the parameters on the deposition. The parameter selections and corresponding parameter set numbers are listed in Table 3-2.

Table 3-2 Parameter combinations, and calculated pulse energy and average power

Parameter set #	Capacitance (μF)	Voltage (V)	Frequency (Hz)	Pulse energy (J)	Power (W)
G1	80	100	50	0.4	20
G2	80	100	100	0.4	40
G3	80	100	150	0.4	60
G4	80	120	50	0.576	28.8
G5	80	120	100	0.576	57.6
G6	80	120	150	0.576	86.4
G7	80	140	50	0.784	39.2
G8	80	140	100	0.784	78.4
G9	80	140	150	0.784	117.6
G10	100	100	50	0.5	25
G11	100	100	100	0.5	50
G12	100	100	150	0.5	75
G13	100	120	50	0.72	36
G14	100	120	100	0.72	72
G15	100	120	150	0.72	108
G16	100	140	50	0.98	49
G17	100	140	100	0.98	98
G18	100	140	150	0.98	147
G19	120	100	50	0.6	30
G20	120	100	100	0.6	60
G21	120	100	150	0.6	90
G22	120	120	50	0.864	43.2
G23	120	120	100	0.864	86.4
G24	120	120	150	0.864	129.6
G25	120	140	50	1.176	58.8
G26	120	140	100	1.176	117.6
G27	120	140	150	1.176	176.4

3.2.3 Characterization

The samples were mounted in conductive resin, and then ground and polished for further study. The OM images were obtained from an Olympus BX51M optical microscope. The deposition thickness and defect rate, and width of the grains were measured using ImageJ, and the deposition rates were calculated. The stainless-steel substrate and Inconel 718 deposition layers were etched using Kalling's No. 2 Reagent and inverted glyceregia, respectively. The microhardness was measured using a Clemex CMT with a force load of 50 g and 10 s dwell time. Each indent was spaced 2.5 times of the indent width. Scanning electron microscopy images and elemental information were obtained by a Field Emission scanning electron microscope (FE-SEM, Zeiss UltraPlus) equipped with energy-dispersive x-ray spectroscopy (EDX, AMETEK EDAX Apollo XL) attachment.

3.3 Results and Discussion

3.3.1 Effect of Pulse Energy and Power Input on Coating

An overall comparison between deposition rate and power in Fig. 3-2a (which incorporates voltage, capacitance, and frequency as shown in equations in Section 2.2.2) shows that increasing the power results in an increased deposition rate that is indifferent to the wall thickness. This suggests that differences in heat accumulation during ESD did not notably affect the deposition rate for wall thicknesses between 0.5 and 1 mm. To observe the effect of frequency, the deposition rate vs. pulse energy for each of the three frequency levels is plotted in Fig. 3-2b (for ESD on a 0.5 mm thick wall) and Fig. 3-2c (for a 1 mm thick wall). These plots show that increasing the pulse energy increases the deposition rate, an observation that holds true for deposits on both wall thicknesses and is more evident at frequencies of 100 Hz and 150 Hz. When ESD is performed at a low pulse frequency of 50 Hz, an increase in pulse energy still results in a slight increase in deposition rate. However, the quantity of material transferred to the substrate is significantly smaller than expected when compared to the higher frequency depositions, which suggests material transfer is less efficient at this low frequency.

The quantity of material buildup on a substrate during ESD is a balance between the amount of material transferred from the electrode and the amount of material removed from the substrate. Due to the high localized heating, some material from both electrode and substrate is lost due to vaporization, or some material transfers from the substrate to the electrode [69], [128]. These reduce the transfer efficiency of the process, depending on the chosen process parameters [69], [128]. In some cases, erosion of the

substrate rather than buildup has been reported [128], [129]; and the mass transfer has been repeatedly shown to be non-linear with respect to the process parameters and deposition time. This non-linearity explains the significantly lower deposition rate at higher pulse energy when using 50 Hz compared to that of 100 and 150 Hz, because of significant erosion of the substrate compensating material buildup at a low pulse energy.

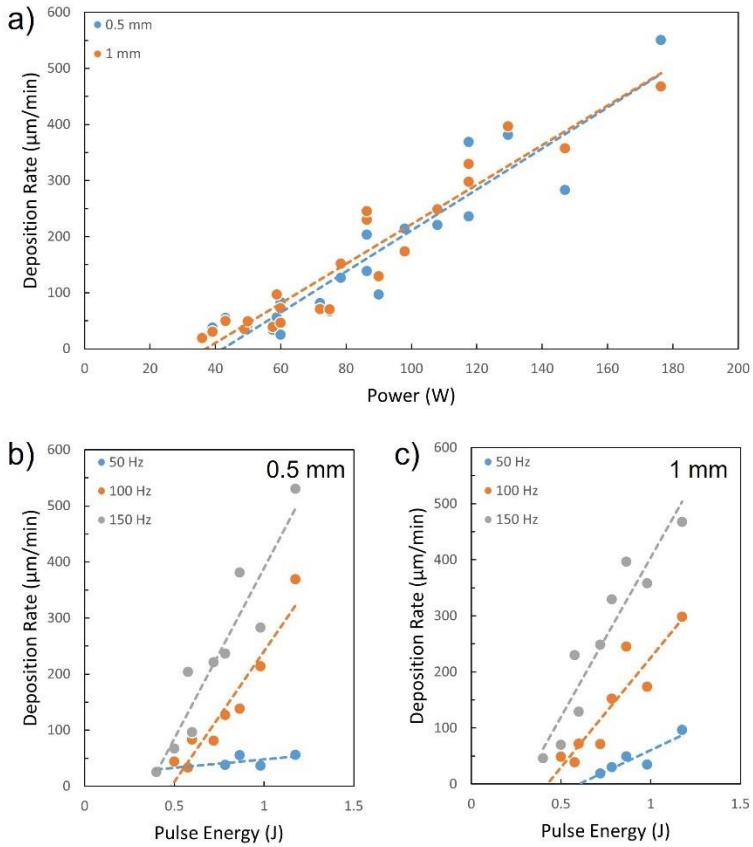

Figure 3-2 a) Overall relationship between the deposition rate and the power input. Relationship between the deposition rate and pulse energy on b) 0.5 mm wall and c) 1 mm wall

The diagrams in Fig. 3-3 show the relationship between pulse energy or power input, and defect rate (voids and oxides), which is defined as the area fraction of the defect viewed on a cross-section. Fig. 3-3a and b indicate the defect rate increases with increasing pulse energy on walls of 0.5 and 1 mm, respectively. Fig. 3-3c also illustrates the positive relationship between the defect rate and power input; where 1 mm wall has lower defects than 0.5 mm wall generally. When lower pulse energy or power

input is used, the type of defect is mainly voids, whereas the voids are dominated by oxides at high pulse energy or power input.

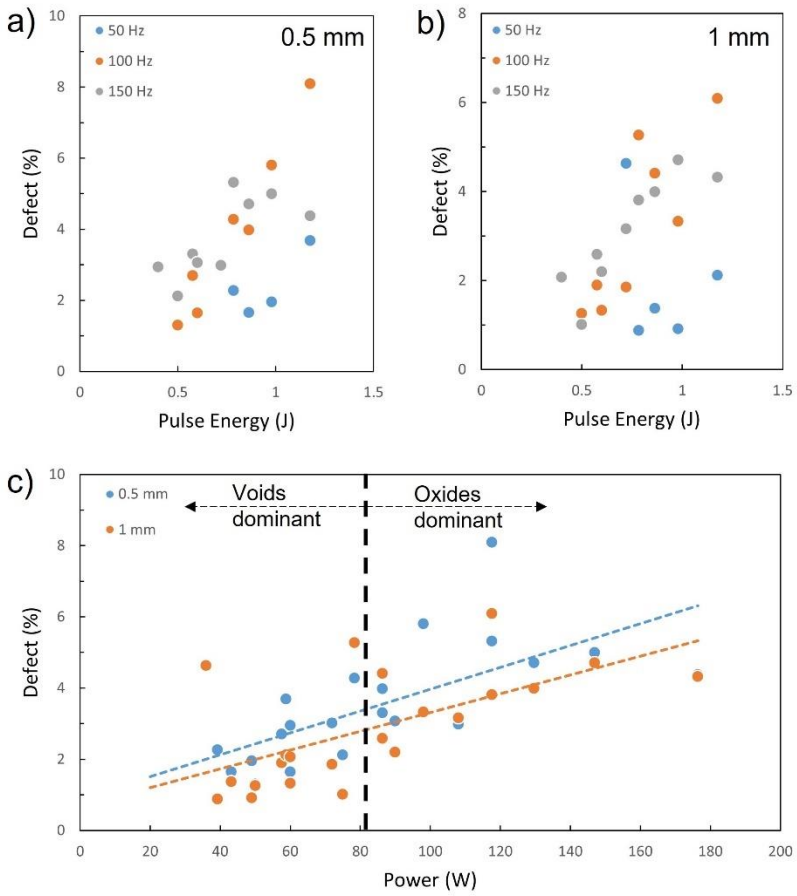

Figure 3-3 Relationship between the defect rate and pulse energy on a) 0.5 mm wall and on b) 1 mm wall; c) overall relationship between the defect rate and the power input

Fig. 3-4 shows optical images of cross-sections of deposits with different ESD parameter sets and different wall thicknesses. As can be observed in the figures, higher pulse energy and power input (Fig. 3-4c, f, G24) produce a larger number and area of defects, which consist mainly of oxides. For the lower parameter set (Fig. 3-4a, d, G6), the defects are mainly voids.

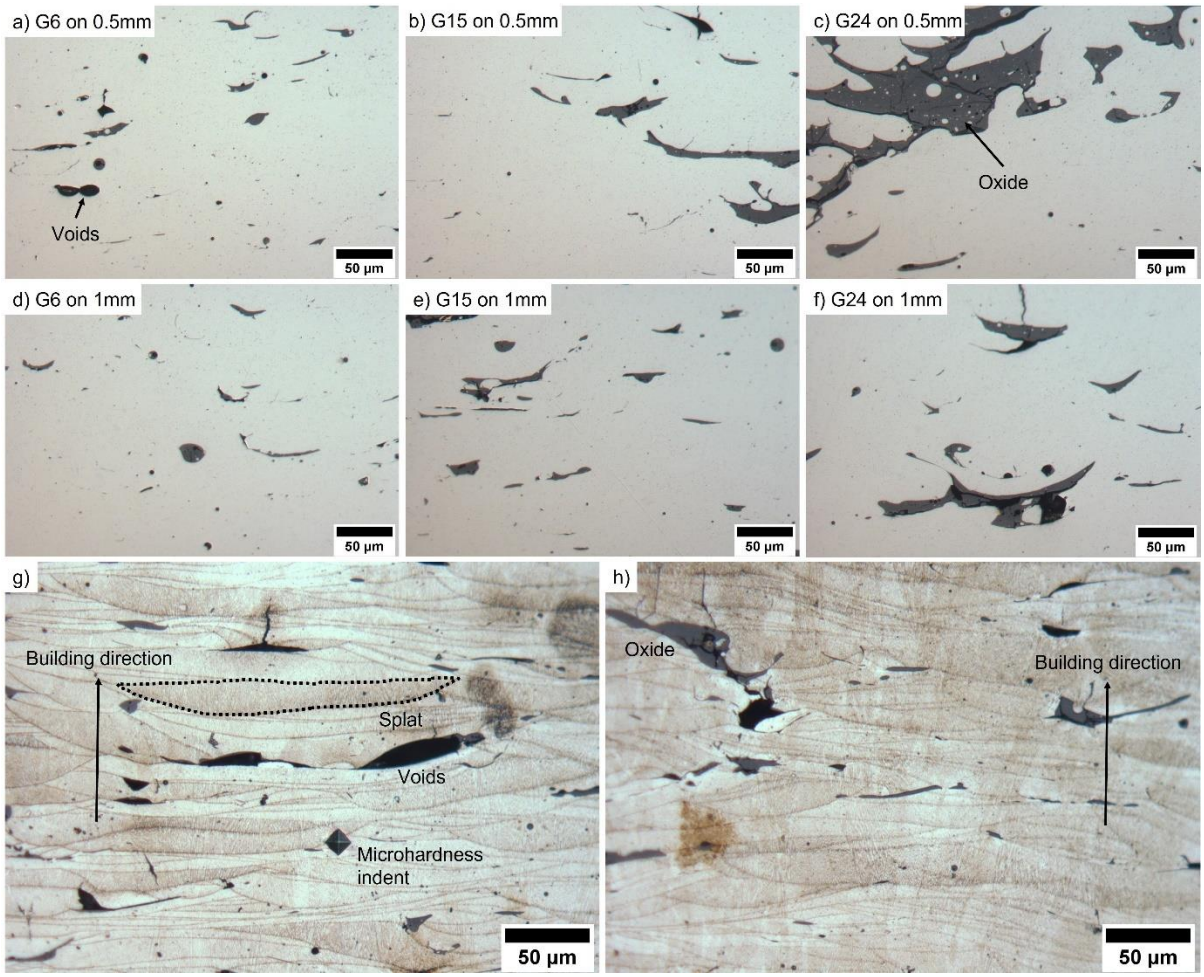

Figure 3-4 Optical images of the cross-section of the deposition under different parameter sets and wall thickness: a,d) G6; b,e) G15; c,f) G24; g) and h) show an etched deposition with visible splat boundary

The individual splat layer boundaries can be clearly observed in Fig. 3-4g and h. The building direction is marked by arrows in the images, and the individual splat layer boundaries are mostly perpendicular to the building direction. Tracing out the splat layer boundaries reveals that the geometric positions of the voids and oxides are mostly located at the interface between the individual splat layers. This suggests that the defect formation occurs as droplets of material are stacked on top of each other and the ESD process parameters strongly govern their formation. The low energy process transfers smaller volumes of material at a time, which cool faster during transit and arrive at the substrate colder. This molten material cools faster and may flow less readily into surface asperities, leaving lack-of-fusion

(LOF) voids. However, increasing pulse energy does not guarantee that these asperities are filled by transferred material. Higher pulse energies can create thicker splats, leading to deep voids if adjacent splats do not overlap. This can be made more problematic over the span of several layers because material is preferentially deposited onto protruding peaks on the substrate surface. Although the larger droplets and higher thermal mass of material transferred with higher pulse energy should keep the material molten for a longer period of time, the solidification rate remains very high and does not guarantee the filling of the voids, which also shows the voids in high pulse energy deposition (G24).

The other major defects are oxides, which are also marked in Fig. 3-4. The EDX analysis of such oxides are shown in Fig. 3-5. The oxides mainly consist of titanium and aluminum, which is similar to previously reported results. This is due to a large amount of heat generated when the tip of the electrode touches the substrate, which causes the rapid aggregation and oxidation of the easily oxidized elements. It is more obvious in the case of high power input. As previously mentioned, the defect rate on 1 mm walls is generally lower than that on 0.5 mm walls due to the lower heat accumulation, which leads to lower oxidation.

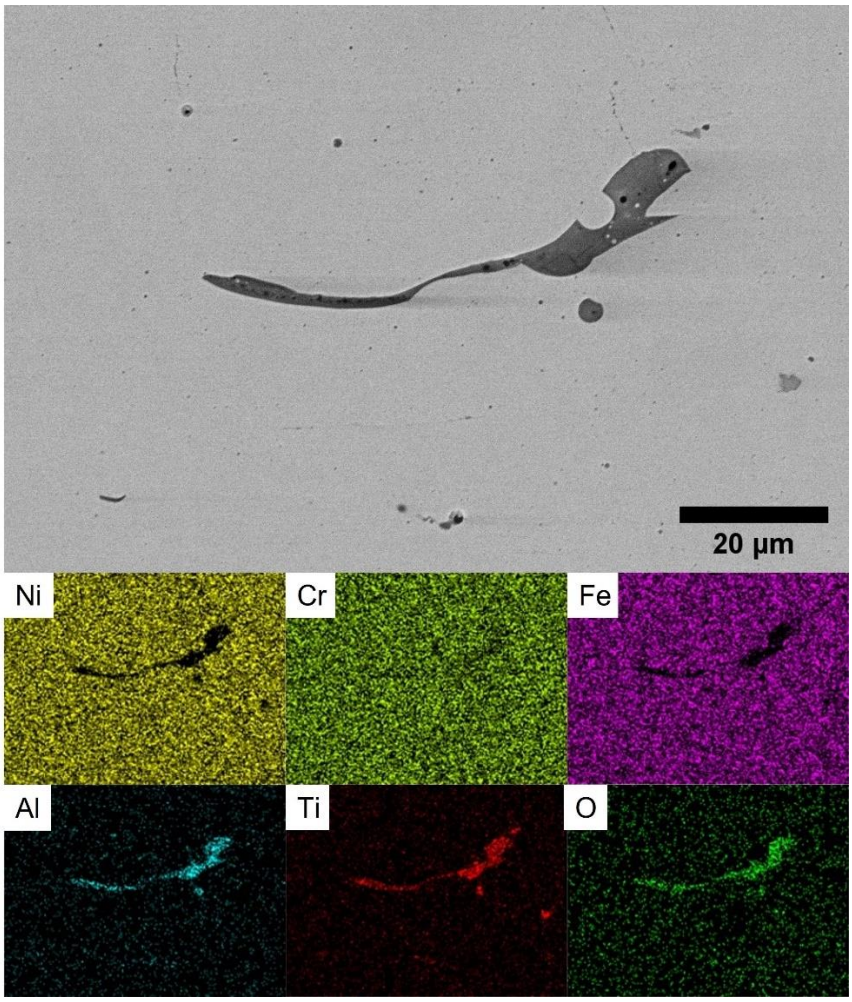

Figure 3-5 EDX analysis of oxide in Inconel 718 deposition layer

From the comparison in Fig. 3-2 and Fig. 3-3, there is a trade-off between deposition rate and defect rate; a higher deposition rate is often accompanied by a higher defect rate. In practical applications, high deposition rate (more economical repairs) and low defect rate (better performance) are desired. Thus, it is important to identify a parameter set that meets the conditions for practical applications. In general, castings can have an acceptable porosity level of up to 5%. It is used as a reference for selecting appropriate ESD process parameters in this study. Among the investigated 27 parameter sets, G6 (80 µF, 120 V, 150 Hz) and G15 (100 µF, 120 V, 150 Hz) are the most suitable ones with sufficiently high deposition rates and acceptable levels of defects. G24 (120 µF, 120 V, 150 Hz) was also characterized as a comparison, which has a very high deposition rate and higher defect level. Their deposition rates and defect rates are listed in Table 3-3.

Table 3-3 The deposition rate and defect rate on 0.5 and 1 mm walls when using three typical parameter sets: G6, G15, and G24

Parameter set #	Parameters	Deposition rate (μm/min)		Defect rate (%)	
		0.5 mm	1 mm	0.5 mm	1 mm
G6	80 μF, 120 V, 150 Hz	203.72	229.75	3.31	2.59
G15	100 μF, 120 V, 150 Hz	220.81	248.27	2.98	3.16
G24	120 μF, 120 V, 150 Hz	381.10	496.44	4.71	3.99

3.3.2 Microstructure and Microhardness of Deposited Inconel 718 Layer

During the ESD process, melting occurs on both the electrode and substrate surface. This provides the opportunity for the transferred material from the electrode to undergo convective mixing with the substrate, resulting in a dilution of the transferred material when both are in the liquid state. During the build-up process, the previously deposited layer solidified but is partly melted again during the deposition of the next layer, allowing the substrate material to dilute further. Due to the small volume of materials transferred during ESD, this dilution is often limited to the first 20-40 μm of material.

One of the benefits of using Inconel 718 for thin wall repair on 17-4 stainless steel is that the distance of elemental mixing can be measured from the chemical content of iron (from 17-4SS) and nickel (from Inconel 718) in the system. A line scan was done between the deposited layer and the substrate, the direction of which is marked with a white arrow in Fig. 3-6a. The positive side in Fig. 3-6b indicates the distance between the point in the deposited layer and the interface; while the negative side indicates the distance away from the interface in the substrate. The content of chromium in the two materials does not differ much and its concentration does not change significantly. The main differences are in Fe and Ni. Fig. 3-6b illustrates the mixing of the elements for the deposition on a thin wall of 0.5 mm made with the parameter set of G15, whose mixing zone is highlighted with a gray box and whose mixing distance is about 39 μm. As a comparison, EDX analysis was also done on two other parameter sets and both wall thicknesses, the results of which are shown in Fig. 3-6c. The mixing distances for G6, G15, and G24 are 24, 39, and 40 μm, respectively, on a 0.5 mm thin wall; and 13, 19, and 22 μm widths are observed on a 1 mm thin wall. Therefore, high pulse energy or power input can promote the mixing of elements at the interface, because more substrate material is melted during deposition. The microhardness in the deposited layer from the interface to the upper surface of the deposited layer is shown in Fig. 3-6d. The microhardness in the region away from the interface is clearly higher than that

in the mixing zone near the interface, confirming dilution does occur during deposition and can change the properties of the deposited layer.

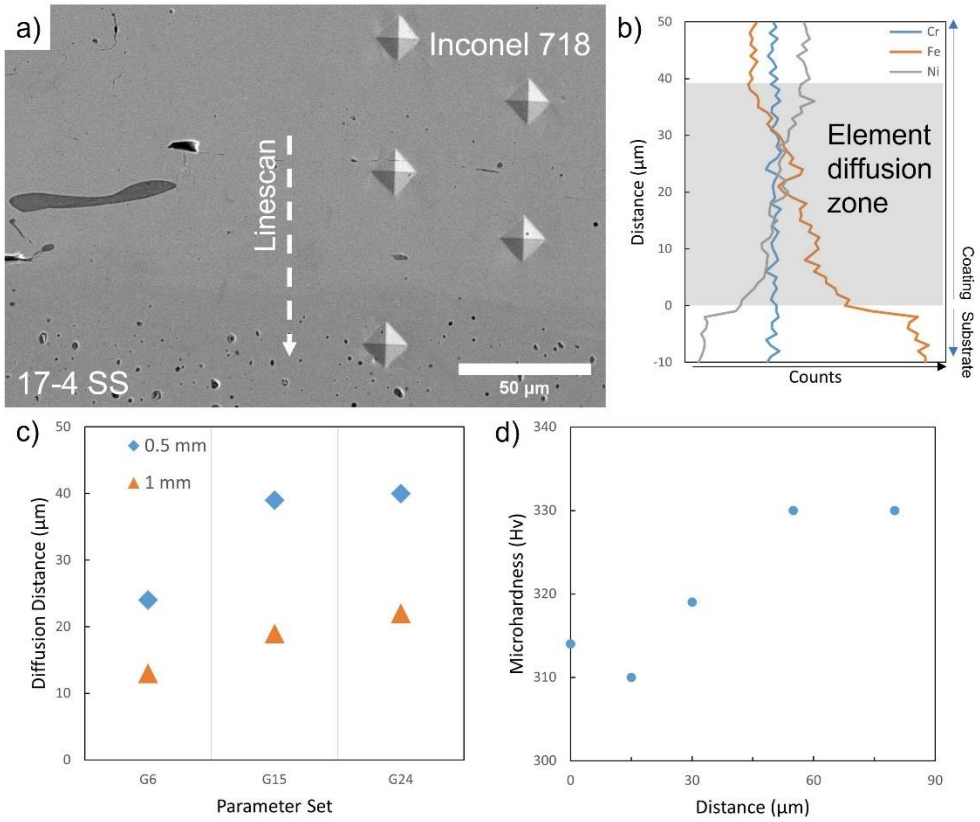

Figure 3-6 a) SEM image of G15, 0.5 mm wall deposition/substrate interface; b) EDX linescan along arrow indicated in a), with zero indicating the deposition/substrate interface; c) comparison of mixing zone size for three parameter sets and two wall thicknesses; d) microhardness measurement from the interface into the G15 0.5 mm wall deposition

During the ESD process, the grains in prior layers – either the substrate or deposited splats – tend to grow in the direction of the buildup [69], [99], [130]. The OM images in Fig. 3-7 show the direction of growth of the grains in the deposited layer. A typical splat layer is highlighted with a black dashed line in Fig. 3-7a, a portion of which is magnified in Fig. 3-7b. Clearly, the cellular microstructure exists in the same splat layer, some misorientation exists between the grains. Further etching leads to Fig.6c, where the higher angle boundaries of individual grains can be distinguished from each other by their color because the etchant attacks differently with different subgrain orientations.

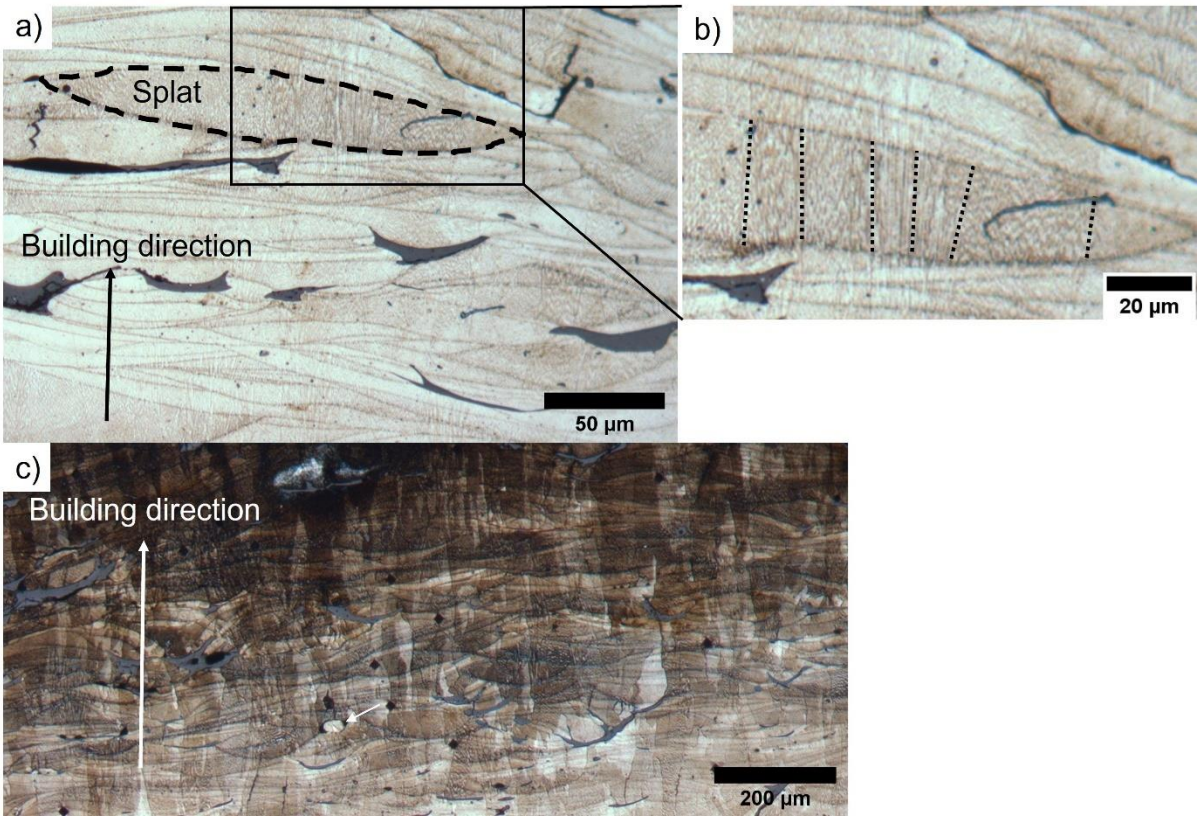

Figure 3-7 OM images of a) minor etched deposition layer with a splat layer circled in black dash line, building direction is also labeled; b) magnified area of the splat shows the different growth directions of grains in the same splat layer; c) further etched deposition showing grain contrast

The Laves phase is often found in the as-solidified microstructure of Inconel 718, which is rich in Nb and Ti [84], [98], [131]. During the ESD process, the partitioning of elements causes this phase to appear at the subgrain boundaries. SEM images of the deposition fabricated with parameter set G24 after etching are shown in Fig. 3-8, with the Laves phase and the Ni matrix labeled in Fig. 3-8a. EDX results of the two phases show the difference in chemical content, with the main differences being the quantity of Nb, Ti, and Al. In addition to the Laves phase, MX ceramic precipitates are also observed in the deposited layers, as shown in Fig. 3-8b and c. They are identified as carbides (NbC) and nitride (TiN), respectively.

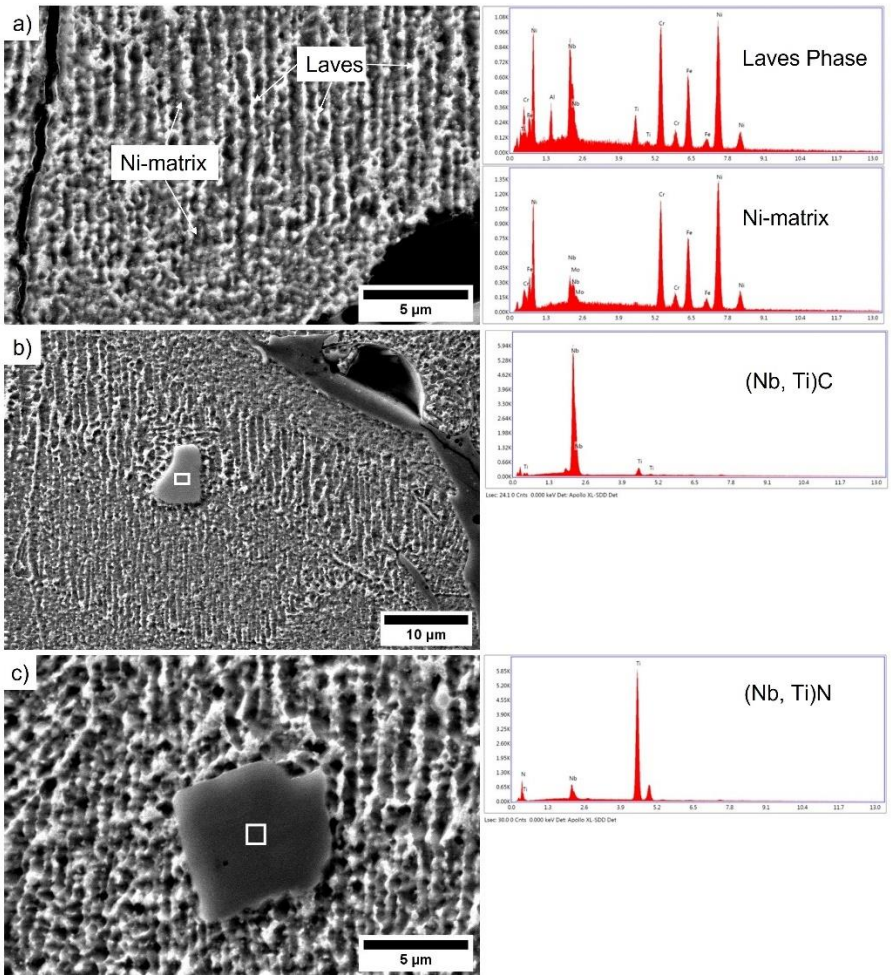

Figure 3-8 SEM images and EDX spectra of a) deposition containing Laves phase and Ni-matrix; b) carbide precipitation; c) nitride precipitation

Fig. 3-9a shows the microhardness in the deposition fabricated with parameter sets G6 (339.11 ± 5.84 Hv), G15 (327.57 ± 5.39 Hv), and G24 (294.36 ± 8.40 Hv) on thin walls of 0.5 mm, which is lower than that on 1 mm walls. A high power input reduces the microhardness of the deposition. This is attributed to greater heating and larger droplet sizes when using higher power parameters. Larger droplets and hotter molten material result in slower cooling rates, which results in a coarser subgrain that reduces hardness [69], [132]. Similarly, when depositing on thinner walls, the low heat transfer rate causes more significant heat accumulation in the deposited layer, making the subgrains coarser. Some variation in a subgrain width is visible within one buildup in different deposited splat, see Fig. 3-9b. Mosaic subgrain patterns can be observed in Fig. 3-9c, indicating that not all columnar subgrains

in this region are aligned perfectly with the building direction. In addition, although the deposition was performed under argon gas flow in the ambient environment, nano-sized spherical oxide particles can still be observed in the deposition layer, as shown in Fig. 3-9d.

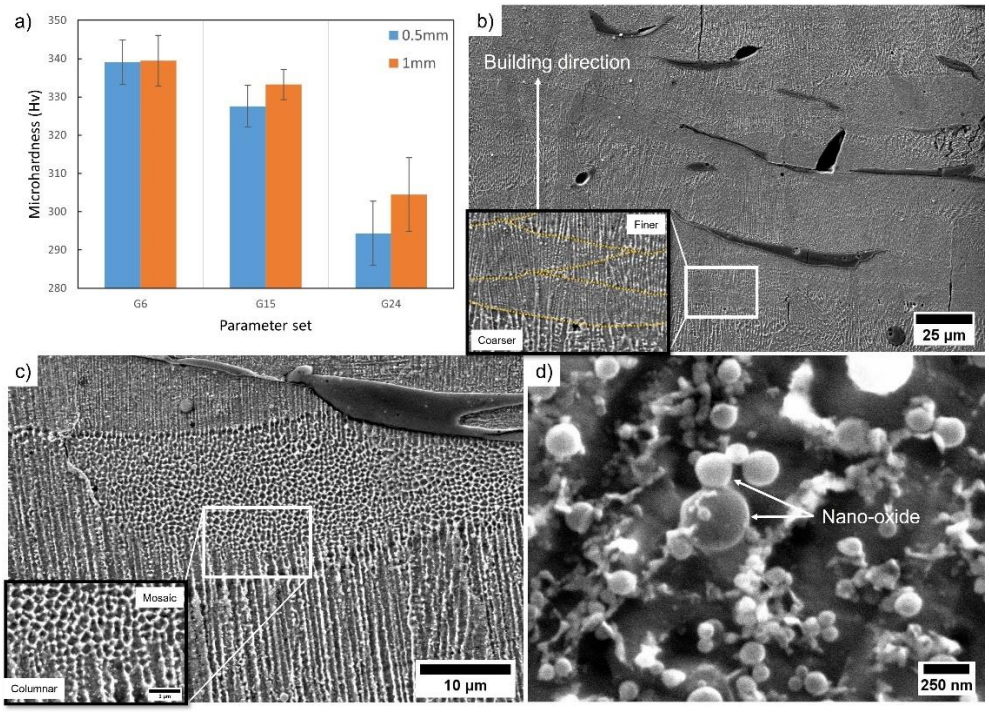

Figure 3-9 a) Vickers microhardness measurements in deposition layer on 0.5- and 1-mm walls using G6, G15, and G24 parameters; SEM image of b) the cross-section of the deposition, with magnified area showing different columnar subgrain widths; c) mosaic and columnar patterns, with magnified grain boundary; d) nano-sized spherical oxide within the buildup

3.3.3 Heat Affected Zone in the Substrate

In the process of ESD, the contact between electrode and substrate raises the local temperature to higher than 8000°C in a very short period of time, but cools down to room temperature at a cooling rate of up to 10^6 K/s. The heating and cooling process is accompanied by a very rapid melting and solidification of the electrode and substrate materials. In general, the short deposition time and fast heat transfer of ESD do not notably affect the microstructure of the substrate material when manufacturing thin Inconel 718 coatings in comparison to other welding/cladding techniques [98], [99]. However, the thin-walled geometry severely reduces the heat transfer efficiency for a heat accumulation, which makes the oxide content in the deposited layer higher than in ESD coatings on larger parts [98]. Therefore, a larger HAZ

may be expected when depositing material on thin geometries.

Fig. 3-10a shows the microstructure of as-deposited part with parameter set G15, while Fig. 3-10b shows the as-printed part with the typical martensitic structure of 17-4 stainless steel. After deposition on the thin-walled parts, the microstructure of the martensitic 17-4 stainless steel undergoes a transformation near the interface from the original martensitic structure into ferrite. In addition to this phase transformation, changes in grain size of the original martensite structure can also be observed further away from the interface. These could result in changes in substrate properties, which will be used to determine the size of the HAZ.

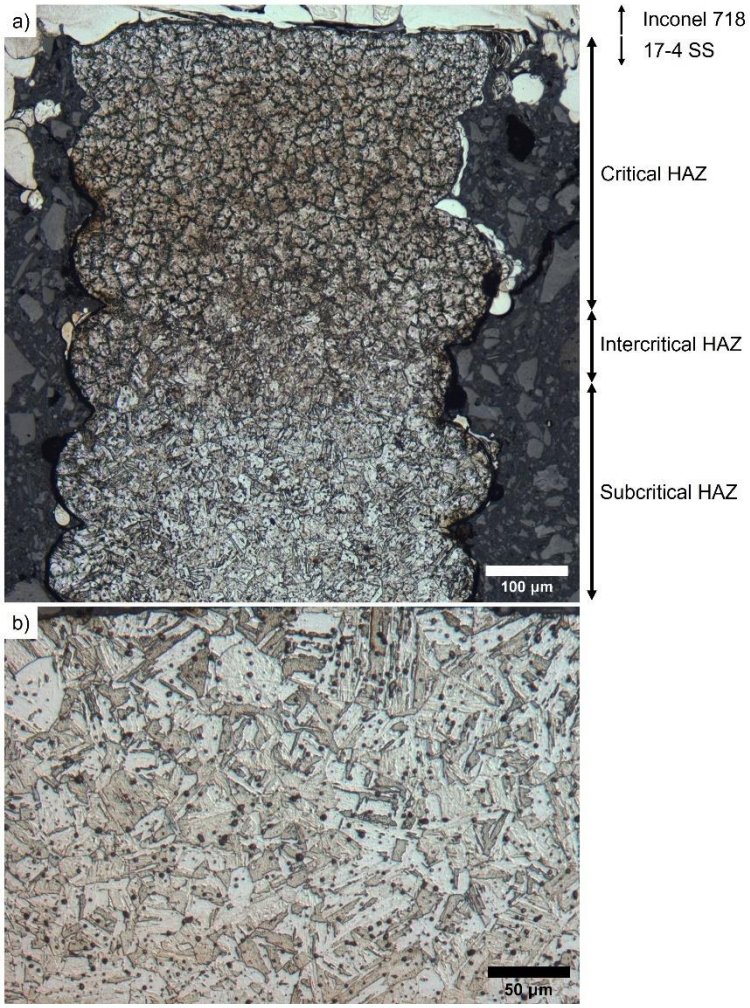

Figure 3-10 OM images of a) HAZ of substrate with parameter set of G15 on 0.5 mm thin-wall; b) microstructure of 117-4 base metal

Fig. 3-11a and b show the profiles of microhardness after deposition with G6, G15, and G24 on thin walls of 0.5 and 1 mm, respectively. The microhardness of 17-4 base metal is about 334.7 ± 3.8 Hv. The microhardness measurements are taken from the interface into the substrate as far as necessary to reach base metal hardness to determine the width of HAZ. The size of the HAZ for G6, G15, and G24 on a 0.5 mm thin wall 17-4 stainless steel substrate is 1700 µm, 2100 µm, and 2200 µm, respectively; while it on 1 mm thin wall is 950 µm, 1250 µm, and 1650 µm respectively. Thus, a high pulse energy or power input is correlated to a wide HAZ. A thicker wall can better dissipate the heat input, resulting in a smaller HAZ.

Thin walls with 0.5 mm thickness built up using lower energy input (G6) achieve a peak microhardness much closer to the interface (386 HV at 450 um) and decline to the base metal hardness at a shallower depth than those with high energy input (G24, 392 HV, 1300 um). The part built up with G24 parameters also sustains the peak microhardness over a larger area (900 um), suggesting that sufficiently elevated temperatures are spread over a larger area when greater energy input was used. For buildups applied with the three typical parameter sets on a 1 mm wall, parameter sets G6 and G15 show a small microhardness increase in comparison to G24. In all cases, the microhardness is lower than the 0.5 mm wall counterparts, ranging from 350-370HV. This suggests that the reduced heating not only lowers the size of the HAZ, but also has a lower effect on microhardness.

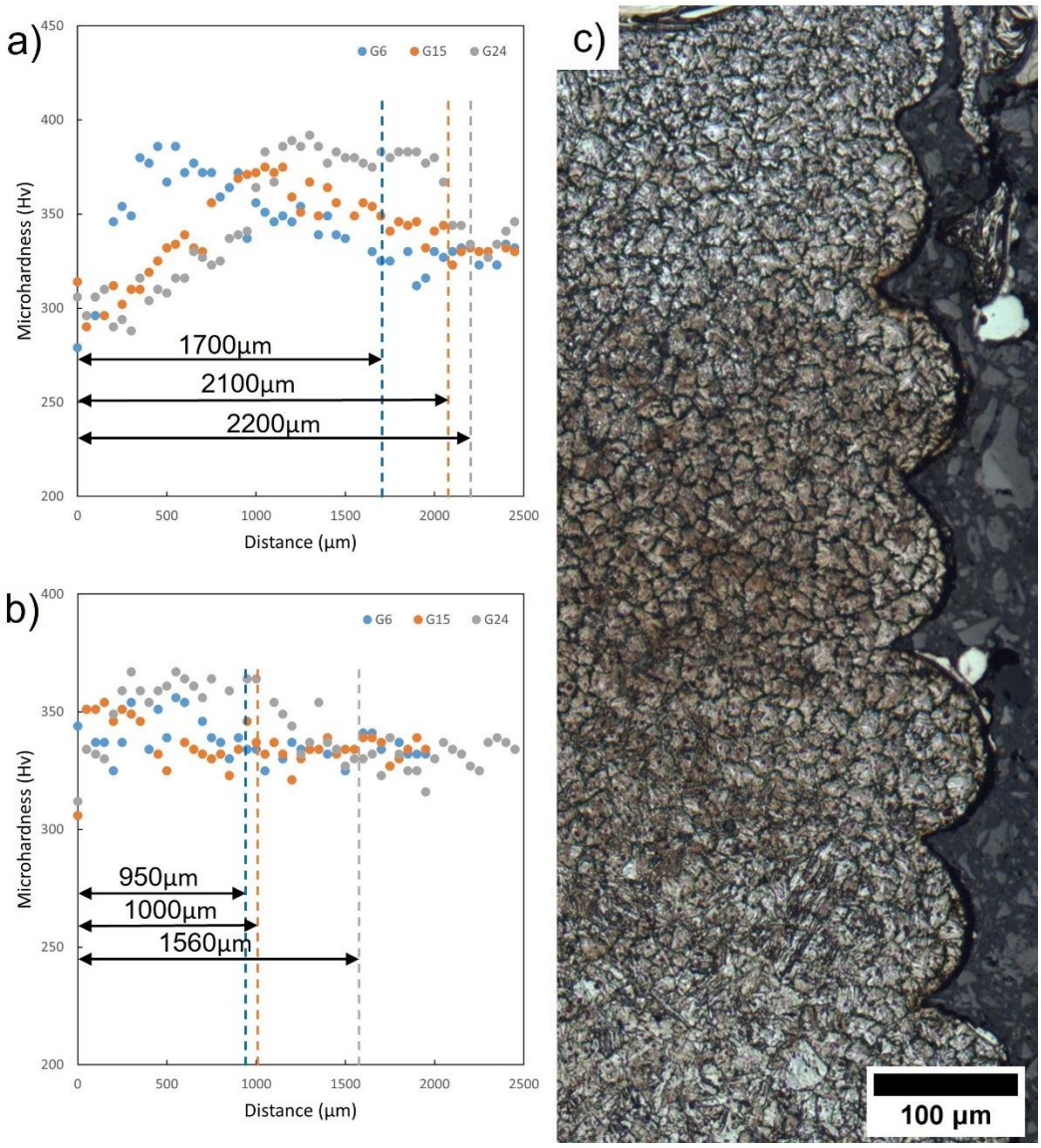

Figure 3-11 Microhardness profile of thin-wall 17-4 stainless steel substrate, with the size of the HAZ labeled for as-deposited part using parameter sets G6, G15, and G24 on a) 0.5- and b) 1-mm wall; c) HAZ microstructure of deposition on 0.5-mm wall with parameter set of G24

3.4 Summary

The study on the ESD repair of additive manufactured 17-4 stainless steel thin walls of 0.5 and 1 mm was performed. A total of 27 ESD parameter sets for the buildup of Inconel 718 were investigated, comparing their deposition and defect rates. The most promising parameter for general repair applications were selected for further characterization, including a measurement of the extent of

dilution between the deposition and substrate, and the formation of a HAZ in the thin-walled substrate.

- Higher pulse energy and power input resulted in higher deposition rates and more defects. There was no significant difference in deposition rate when comparing buildup on 0.5 and 1 mm walls.

- At low power input, voids were dominant defects; while oxides were dominant in high power set up. The selection of parameter sets for repair applications requires balancing deposition quality with deposition rate, and is frequently application specific.

- The width of the mixing/dilution zone between the deposition and substrate was larger when higher pulse energies and power inputs were used. The dilution zone was also more significant when depositing on thinner walls, due to heat accumulation and more melting of the substrate. The optimized parameter set produced a desired dilution zone of 10 μm, above which the composition was as expected for an Inconel 718 deposition.

- Lower energy/power input resulted in finer columnar subgrains and higher microhardness; while deposition on the thicker 1 mm wall also had higher microhardness than deposition on the 0.5 mm wall. 0.5 mm wall showed a wider HAZ than 1 mm wall after deposition.

- The optimized ESD parameters with an acceptable deposition rate, adequately low defect rate, high microhardness, minimal dilution, and minimal HAZ size were chosen, to demonstrate the successful repair of a pump impeller blade and a turbine blade.

Chapter 4

CrFeCoNi MEA Coating with Electrospark Powder Deposition

4.1 Introduction

HEAs is one of the most researched topics today because there are many gaps in the HEA system that make the results of studying HEA even more valuable. This study fabricates a CrFeCoNi MEA coating on A516 steel via ESD process using Cr, Fe, Co, Ni powders. The deposition parameters, such as electrical parameters, molar fraction of elements, and ESD process were optimized to reach the desired composition in the equiatomic CrFeCoNi MEA coating. The microstructure of the coating was analyzed. The roughness and the microhardness of the coating was measured, and the wear property of the coatings was also evaluated.

4.2 Materials and Methods

4.2.1 Experimental Materials

Commercially available Cr, Fe, Co, and Ni powders (Thermo Fisher Scientific) with morphology shown in Fig. 4-1a-d were used as feedstock. During the deposition process, a slurry-like powder mixture was used for this study to reduce dry powder movement due to the rotating electrode and flowing gas cover. The four metal powders were mixed according to the equal mole fraction of each element in the MEA. The ratio of mixed powder: polyvinyl alcohol solution (PVA, 80wt.% aqueous): ethylene glycol (EG) was 12g:1mL:1.4mL to form a slurry. The slurry was applied onto a 1.76 mm thick A516 plate and then dried on a hot plate. The morphology of the slurry after drying is shown in Fig. 1e.

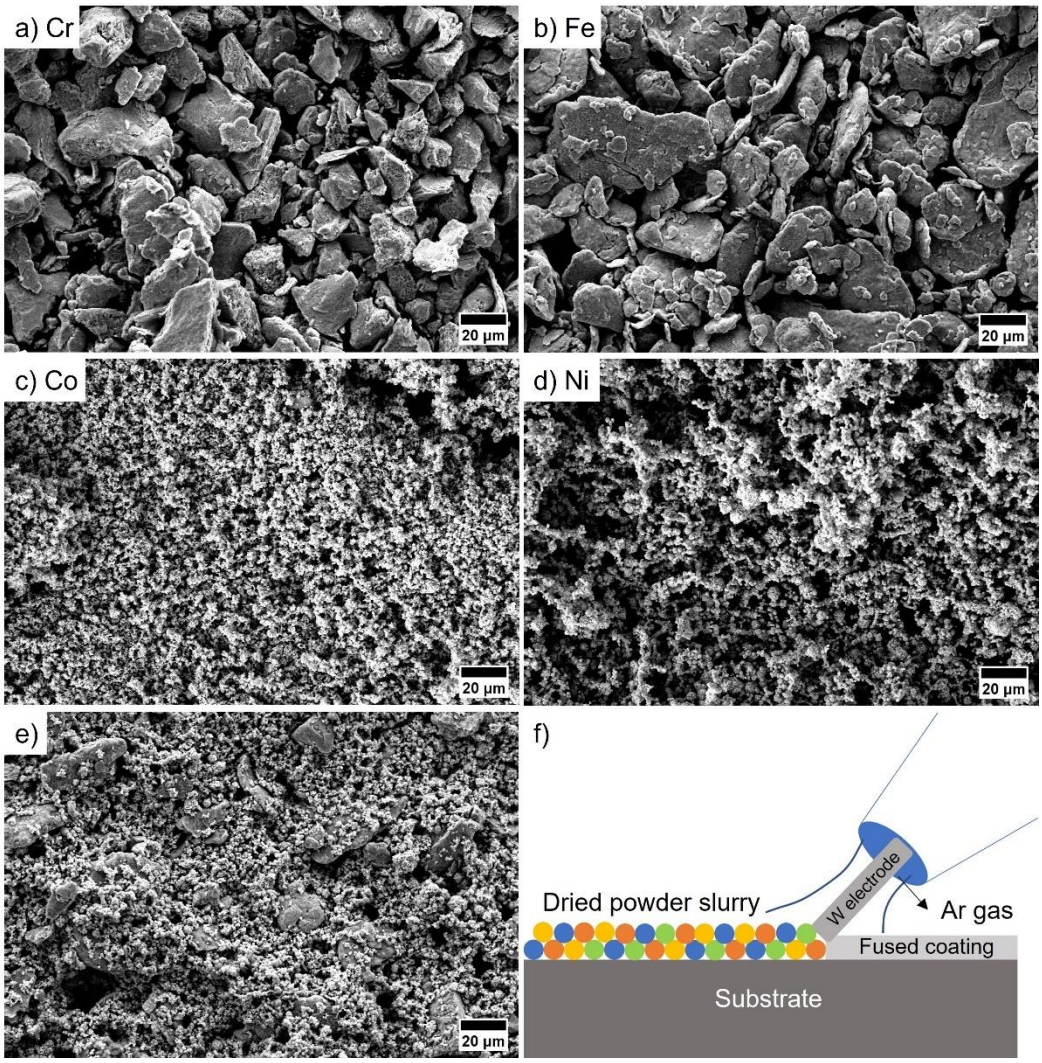

Figure 4-1 Morphology of powder feedstock a) Cr; b) Fe; c) Co; d) Ni; and e) dried slurry; f) a brief sketch of ESPD

4.2.2 Electrospark Power Deposition (ESPD) Process

The process of the ESPD is sketched in Fig. 4-1f. A pure tungsten rod with 3.175 mm in diameter was used as the electrode to restrict the unexpected addition of the electrode material into the ESD coating. The process parameters adjusted in this study to create the alloy coating are capacitance, voltage, and pulse frequency, with the ranges shown in Table 4-1. A manual ESD machine manufactured by Huys Industries was used with a 30 L/min flow of argon shielding gas to minimize the oxidation of the powder.

Table 4-1 Electric parameters attempted for powder deposition using ESD

Capacitance (μF)	Voltage (V)	Discharge frequency (Hz)
60, 80, 100, 120, 150, 180	40, 70, 100	100, 150, 200, 250

The deposition rate was calculated from the deposition weight, which was measured by weighing the samples before and after applying the coating, by per unit area.

4.2.3 Characterization

The samples were mounted in conductive resin and were ground and polished. The A516 steel substrate was etched with Nital etchant and the alloy coating was etched by Kalling's 2 Reagent. Microhardness was measured by a Clemex CMT (v. 8.0.197) with a force load of 25 g and a dwell time of 10 s. A linear wear tester was used to perform the wear test with a force load of 988.9 g for 200 cycles (400 passes) with 7 mm of travel distance per pass. Roughness was measured with a WYKO NT1100 optical profiler and a Keyence VK-X250 Laser Profilometer.

Image analysis was performed on an Olympus BX51M optical microscopy and a Zeiss UltraPlus Field Emission scanning electron microscope (FE-SEM) with an AMETEK EDAX Apollo XL energy-dispersive X-ray spectroscope (EDX) attachment for element information. XRD spectra were obtained by PANalytical Materials Research Diffractometer (MRD) with copper being anode material, X-ray wavelength of 1.5406 Å, and scanning angles of 2θ=20-90°. The electron backscattered diffraction (EBSD) was performed using a JEOL 7000F SEM in Canadian Centre for Electron Microscopy (CCEM), and the obtained results were post-processed using HKL channel 5 software.

4.3 Results and Discussion

4.3.1 Deposition Process Optimization

The conventional principle of ESD is the generation of sparks when the anode and cathode come into contact, resulting in a very high local temperature that causes the anode electrode material to melt, transfer, and solidify onto the cathode substrate [70]. Similarly, when ESD is performed with powders, the powder particle in contact with the cathode substrate can be considered as the cathode during the powder deposition process. Sparks are generated when the anode contacts the cathode powder, which is also in contact with the dense cathode substrate. High localized temperatures cause the powders to melt, fuse together, and solidify onto the substrate to form coating. A cross-sectional image of the

coating deposited with the ESD parameter set of 100 μF, 60 V, 100 Hz, which corresponds to a relative low pulse energy of 0.18 J and power input of 18 W, is shown in Fig. 4-2. As can be seen in Fig. 4-2a, most of the powders are fused, but some unmelted particles are still visible. EDX analysis shows these are mainly unmelted Co and Ni powders located between a fused layer of powder and the substrate. This is expected to be highly detrimental to the integrity of the coating, and suggests that the pulse energy and power input needs to be increased to ensure a greater melting. When the parameters are increased to 180 μF, 100 V, 250 Hz, corresponding to high pulse energy and power input of 0.9 J and 225 W, respectively, the powders are completely fused whereas tungsten could also be deposited from the electrode as shown in Fig. 4-2b. EDX analysis shows the weight fraction of the W was 63.13% because of excessively high pulse energy. Therefore, a medium parameter set of 150 μF, 70 V, and 200 Hz was selected for powder deposition for detailed study. The EDX analysis in Fig. 4-2c shows a lack of fusion in Cr powder that was not completely melted when using this medium energy parameter set.

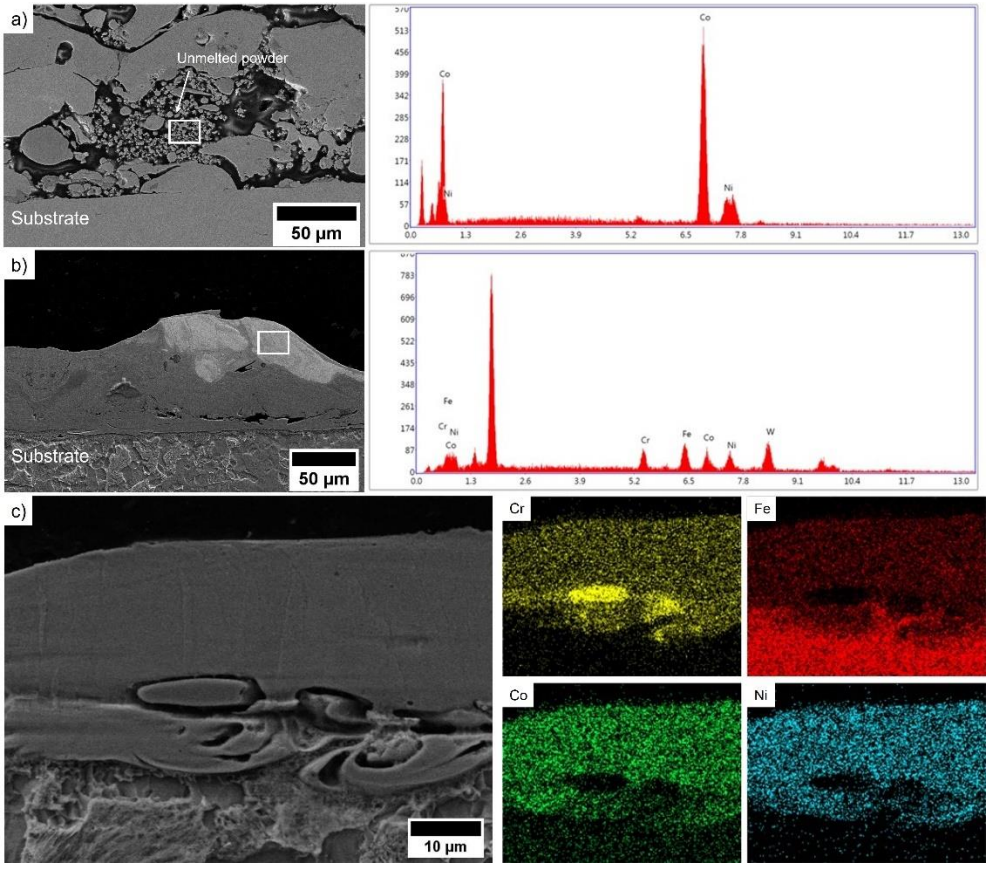

Figure 4-2 SEM image of a) partially molten powder mixture with its magnified area at low pulse

energy and power input; b) undesired W inclusion at high pulse energy and power input; c) unmelted Cr and its EDX mapping

Firstly, the initial powder slurry with a mole fraction of 1:1:1:1 for the constituent elements is used. The dried slurry was then coated on the substrate surface using a pure tungsten rod as the electrode with the selected parameter set. The cross-section of the as-deposited coating with the medium parameter set is shown in Fig. 4-3a. The EDX line scan in Fig. 4-3b indicates the atomic percentages of Cr, Fe, Co, and Ni are 20.72 ± 1.86%, 28.92 ± 1.32%, 25.44 ± 1.42%, and 24.92 ± 1.08% (ratio is 0.83:1.16:1:1), respectively. It is found that the Cr concentration is low while Fe is high, and Co or Ni are almost equal to the desired 25%. This is because of their different melting points. Cr has the highest melting point of 1907 °C; whereas Fe, Co, and Ni with lower melting point could be melted more thoroughly. This explains why a lack of Cr fusion as observed in Fig. 4-2c and a lower Cr fraction was present in the coating. The more-than-expected Fe content may be from the steel substrate. Therefore, an adjustment of the molar ratio for the four constituent elements can be rationalized by their melting points and external sources of material, a lower degree of fusion is expected with higher melting temperature materials.

The powder proportions were then adjusted according to the corresponding deposited ratio, calculated by expected fraction/received fraction (1/0.83:1/1.16:1:1). Consequently, the modified slurry with mole fractions of 1.2:0.86:1:1 is designed to achieve the expected ratio of 1:1:1:1. The new coating in Fig. 4-3c-d shows a quite uniform coating without obvious unmelted powders, with an equal mole fraction of 24.83 ± 2.49%, 25.20 ± 2.59%, 25.07 ± 2.18%, and 24.89 ± 1.44% for these four elements, respectively. The calculated coating deposition rate is $5.80\times10^{-5} \pm 1.74\times10^{-5}$ g/mm^2.

The XRD spectra of the A516 steel and the deposited coating are shown in Fig. 4-3e and f, respectively. The A516 substrate has a BCC phase whereas the coating has the FCC phase. There are three peaks at 2θ of 43.75°, 50.86°, and 74.95°, corresponding to (111), (200), and (220) plane of FCC, respectively. The lattice constant of the deposited alloy is calculated to be 0.358 nm, which is in agreement with the CrFeCoNi alloy fabricate with laser melting [133] and arc melting [134] methods. Therefore, it can be concluded that the fabricated alloy coating is a promising single phase MEA CrFeCoNi.

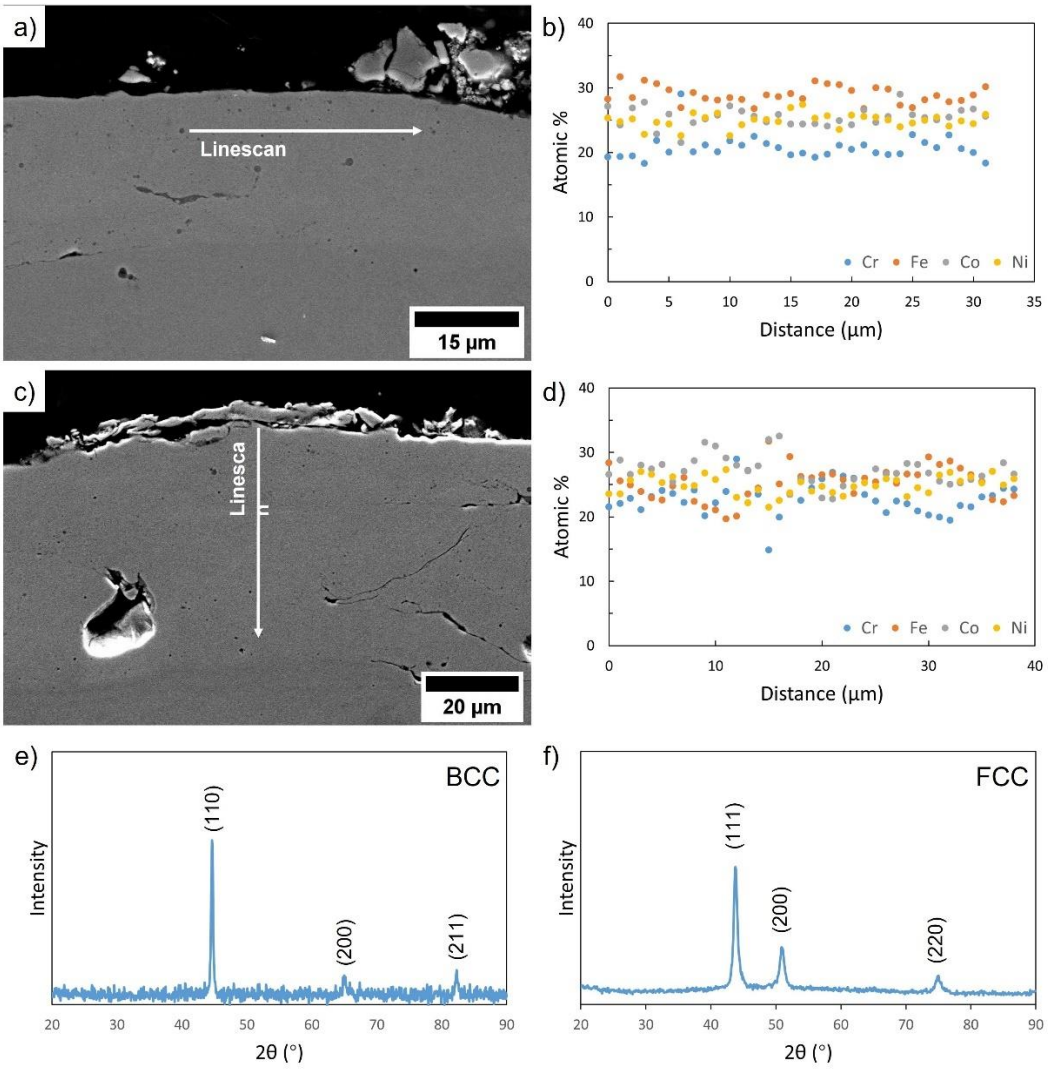

Figure 4-3 Cross-section and EDX analysis of deposited coating with a-b) equal atomic Cr, Fe, Co, Ni slurry mixture and c-d) optimized unequal mixture. XRD analysis of e) A516 steel substrate and f) the deposited coating

When deposition is performed directly with electrodes (electrospark electrode deposition ESED), the electrode material melts and rapidly solidifies onto the substrate surface. For ESPD, the powders act as an intermediate between the electrode and substrate. The poor electrical connection between the powders and the substrate would cause the melted powders been deposited on electrode as well, see Fig. 4-4a. The EDX analysis (Fig. 4-4b) indicates the deposition on electrode yields an atomic fraction of 24.55%, 24.84%, 26.87%, and 23.73% for Cr, Fe, Co, and Ni, similar as the coating composition on

the substrate. This suggests MEA is also deposited on W electrode. Consequently, post surface smoothing process was then performed with this MEA coated W electrode using low pulse energy conditions to smoothen the deposited coating on the substrate. Although low pulse energy decreases the deposition rate, re-melting/depositing the MEA alloy on the electrode to the valleys for smoothening the substrate surface can happen. In the study, the parameter set of 60 μF, 40 V, 100 Hz was used for surface smoothening. Fig. 4-4c-f show the surface morphology and roughness of coating before and after smoothening. The arithmetical mean height (Ra) within the effective measurement area is 17.86 μm, while the distance between the peak and the valley (Rz) is 127.73 μm. A significant improvement in roughness after low-pulse-energy smoothing is observed, with a decrease in Ra and of Rz 11.61 μm and 83.23 μm, respectively.

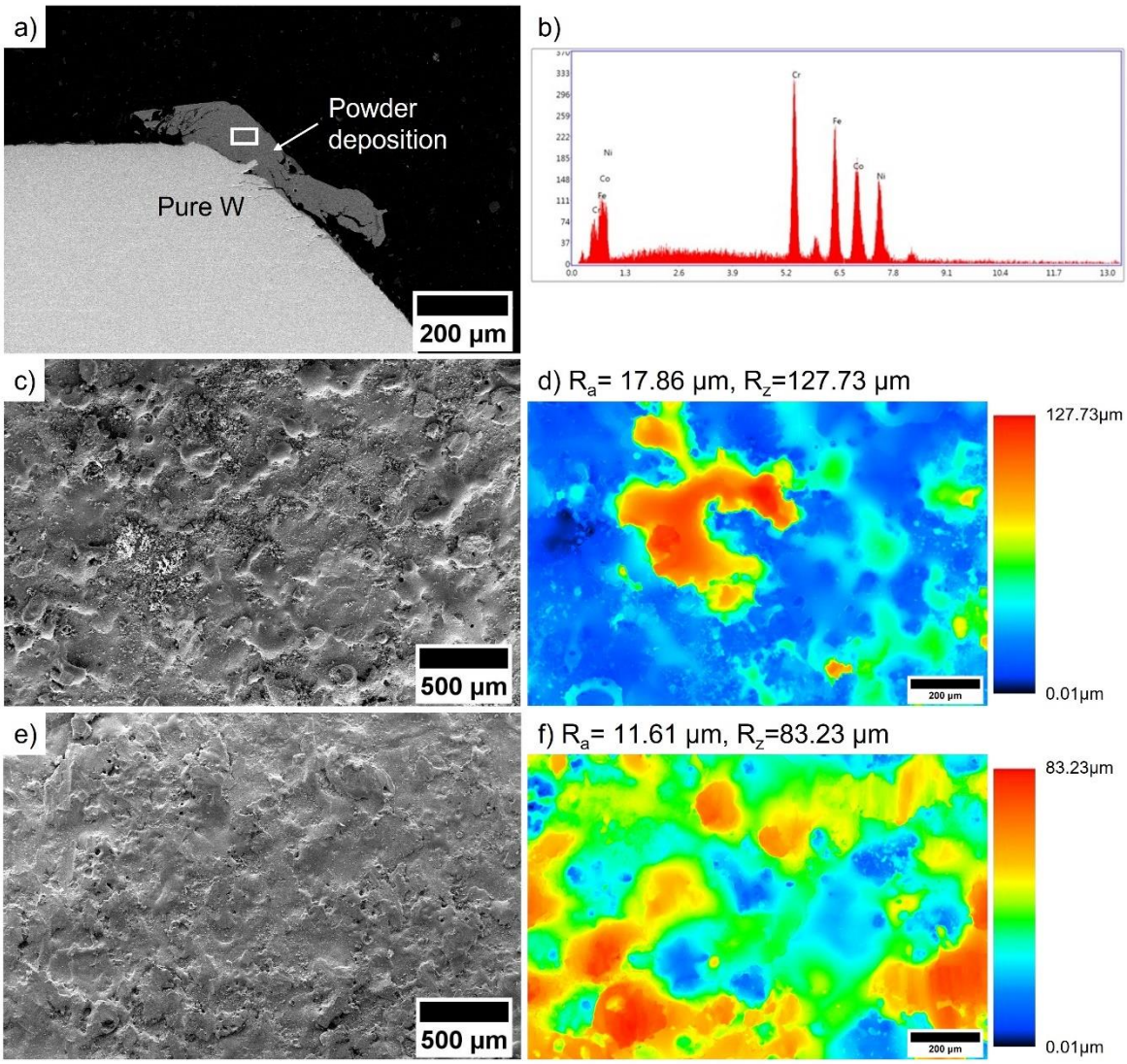

Figure 4-4 a) SEM image of W electrode after deposition with powder deposited on the electrode and b) the EDX analysis of deposited alloy; c) SEM image of the as-deposited coating surface with high pulse energy and d) its roughness measurement; e) smoothened surface with deposition of alloy on the electrode under low pulse energy and f) its roughness measurement

4.3.2 Microstructure Analysis of the In-situ MEA Coating

The OM images of the deposited microstructure after etching are shown in Fig. 4-5. Fig. 4-5a and c illustrate the microstructure at low magnification, where columnar grains parallel to the deposition direction can be observed because this direction has the maximum temperature gradient [135]. Representative areas in Fig. 4-5a and c are marked with white boxes and their magnified areas are

shown in Fig. 4-5b and d with white dotted lines marking the visible grain boundaries.

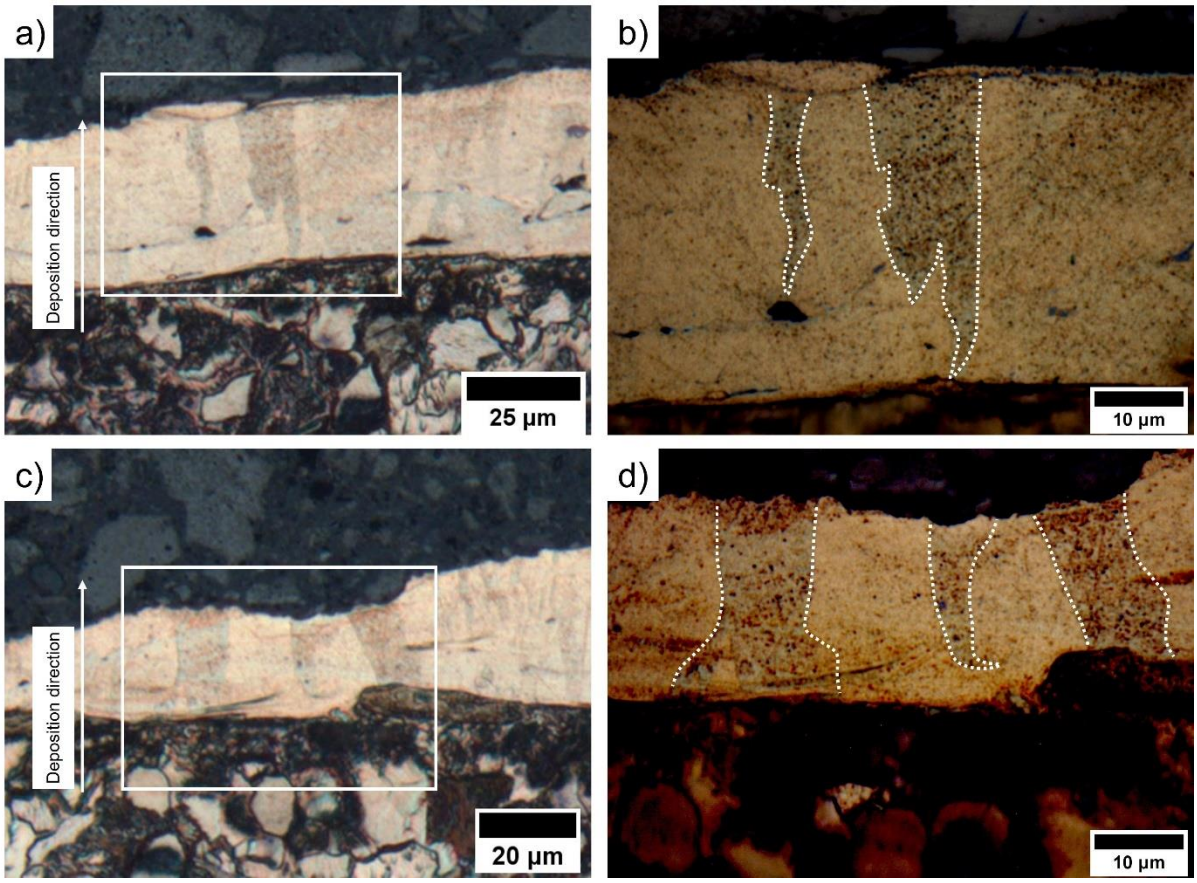

Figure 4-5 OM images of minor etched coating, where a) and c) grains are parallel to the deposition direction with b) and d) magnified areas, respectively

OM image of the coating after major etching are shown in Fig. 4-6a, which contain substrate, ESPD layer, and the afterward ESED layer from smoothening process. The morphology of the microstructure of the matrix of the coating (Point 1) is far more different than the transition zone near the substrate (Point 2). EDX analysis in Fig. 4-6b indicate that point 1 has a uniform distribution of the four elements with an atomic fraction of 1:1:1:1, while point 2 has a Fe-rich composition. During the traditional ESD process, the melting and solidification of the substrate material are also necessary to bond the electrode material to the substrate material, which is accompanied by the dilution of the substrate elements into the coating to form an electrode-substrate alloy [136]. This dilution could also result in the formation of the Fe-rich transition zone near the interface in this ESPD process. No W was detected in the overall regions, suggesting the melting of W is negligible in the process. SEM image at the same area is shown

in Fig. 4-6c. EDX mapping shows homogeneous distribution of elements in the coating and no obvious segregation of elements between different grains. However, there is a Fe-rich zone in the range of about 10 μm above the interface which behaves differently in the susceptibility to etching.

The boundaries between the different deposited passes can be observed and are marked in Fig. 4-6c. The grains extend from the substrate to the top of the coating indicated by arrows that penetrate throughout multiple fusion lines, this is because the atoms in the liquid (melted material) stick on the solidified materials and arrange themselves with the same atomic pattern, thus they do not change the orientation of crystallization [135]. Three regions with different microstructures are represented with numbers in Fig. 4-6d. With the melt pool highlighted with dash line in Fig. 4-6d, region 3 is considered as the ESED layer, evidences being 1) a thick central region, where melting is most severe, and thin sides can be observed, which attributes to material splat during the ESED, and 2) vertical texture roughly parallel to the buildup direction indicated by the arrows in Fig. 4-6d. Region 1 and 2 represent the ESPD layer which does not have the splashing structure. ESED involves a relatively higher or more effective heat input, which can coarsen the texture of the deposited layer [72], in this case, region 2 has a coarser granular textures size of 1-2 μm, and those of the texture in region 1 are <1 μm. However, the heat input of ESPD is not high enough to coarsen the deposited ESED layer, resulting in the texture size in region 2 being evidently larger. The material melting and transfer mechanism occur in pulses during each ESPD pass, it is not possible to distinguish individual layers attributed to each of the three powder deposition layers. The relatively random nature of the discharge mechanism during ESD results in solidified melt pools with random degrees of overlap compared to other coating or additive processes, which leaves a lower degree of tensile residual stresses.

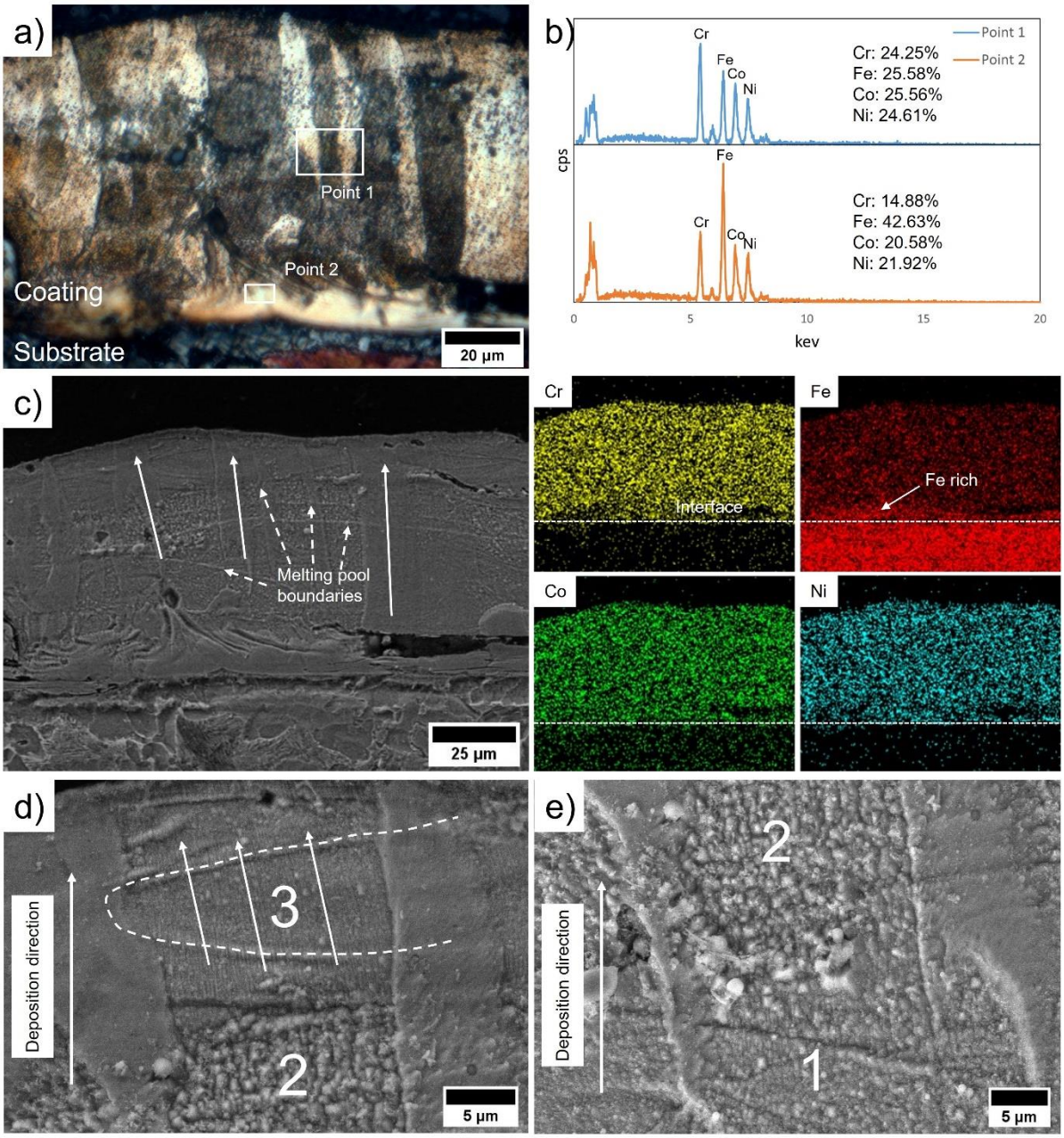

Figure 4-6 a) OM image of the major etched region; b) EDX point scan at two marked regions in a); c) SEM image at the same region with EDX mapping; d) and e) representative magnified areas in a)

EBSD results of the coatings are shown in Fig. 4-7. The substrate and coating have the iron BCC phase and the FCC phase, respectively, as shown in Fig. 4-7a. The equiaxed grains can be observed in the

substrate in Fig.7b, while the coating has large columnar grains, which is consistent with the OM and SEM observations. An unindexed layer with a thickness of approximately 5 µm can be observed near the interface between the substrate and the coating, which is due to the dilution of the substrate elements and the formation of an iron-rich region near the interface as already identified in Fig. 4-6c. Since the phase in this transition zone is not uniform, the Kikuchi pattern is not able to be indexed. In addition, the contents in this region could also be intermetallic phases because of the high concentration of Fe. The grain size near the interface is smaller than that in the bulk region, which is because the materials in this region are formed through recrystallization during the melting and solidification process, which can also be observed in Kernel average misorientation (KAM) map in Fig. 4-7c, with a relatively higher misorientation near the interface. The above region can be considered as the intermetallic compounds or HAZ), which has a size of approximately 12 µm.

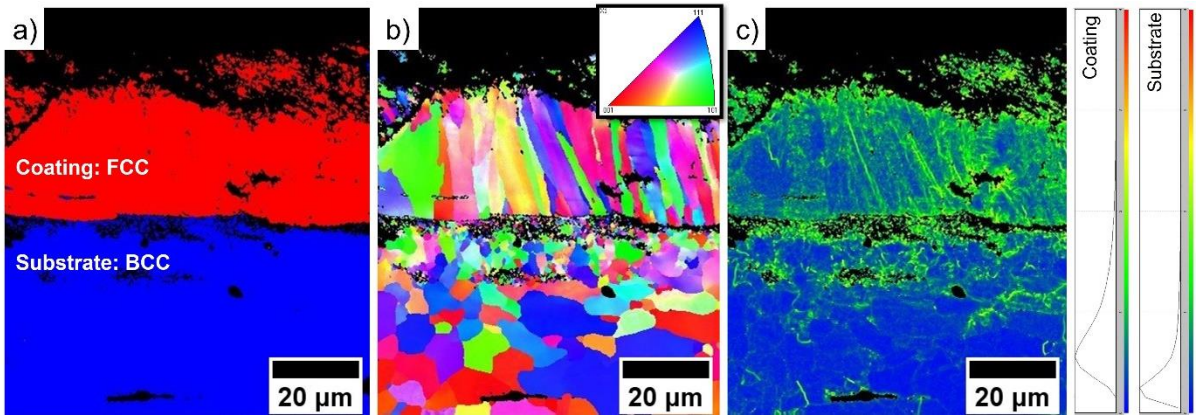

Figure 4-7 EBSD analysis of deposition with a) phase map; b) IPF X map, and c) KAM map

4.3.3 Heat Affected Zone in the Substrate

The microstructure of the as-received A516 carbon steel substrate is shown in Fig. 4-8a. A ferritic microstructure is observed and the measured microhardness of the as-received A516 steel is 186 ± 3.5 Hv. Small changes in terms of the phases and size of the grains are observed after the ESD process, as shown in Fig. 4-8b. This is attributed to the low-energy input that occurs during ESD, with minimal heating of the substrate. The microhardness measured on the coating is 331.53±18.96 Hv, which is much higher than that of the cast [137]–[139] and arc melted [140] which has a much lower grain width of approximately 7 µm as shown in Fig. 4-7b in this study. Therefore, the relatively high hardness can be attributed to the finer grain size, and the width of the texture may also play an important role in

determining the microhardness [69], [132] and possibly high residual stresses caused by very high cooling rates in ESD process [134].

The microhardness profile is shown in Fig. 4-8c, the negative and positive x-axis represent the distance from the measured indentation in coating and substrate to the deposition-substrate interface, respectively. The microhardness of the interface (distance = 0) is much higher than the A516 steel and the deposited CrFeCoNi. This is attributed to the dilution of Fe from the substrate and the coating materials during ESD. As a result, the chemical composition of the coating nearest the substrate is Fe-rich and displays increased hardness because of the formation of IMCs as observed in Fig. 4-7b.

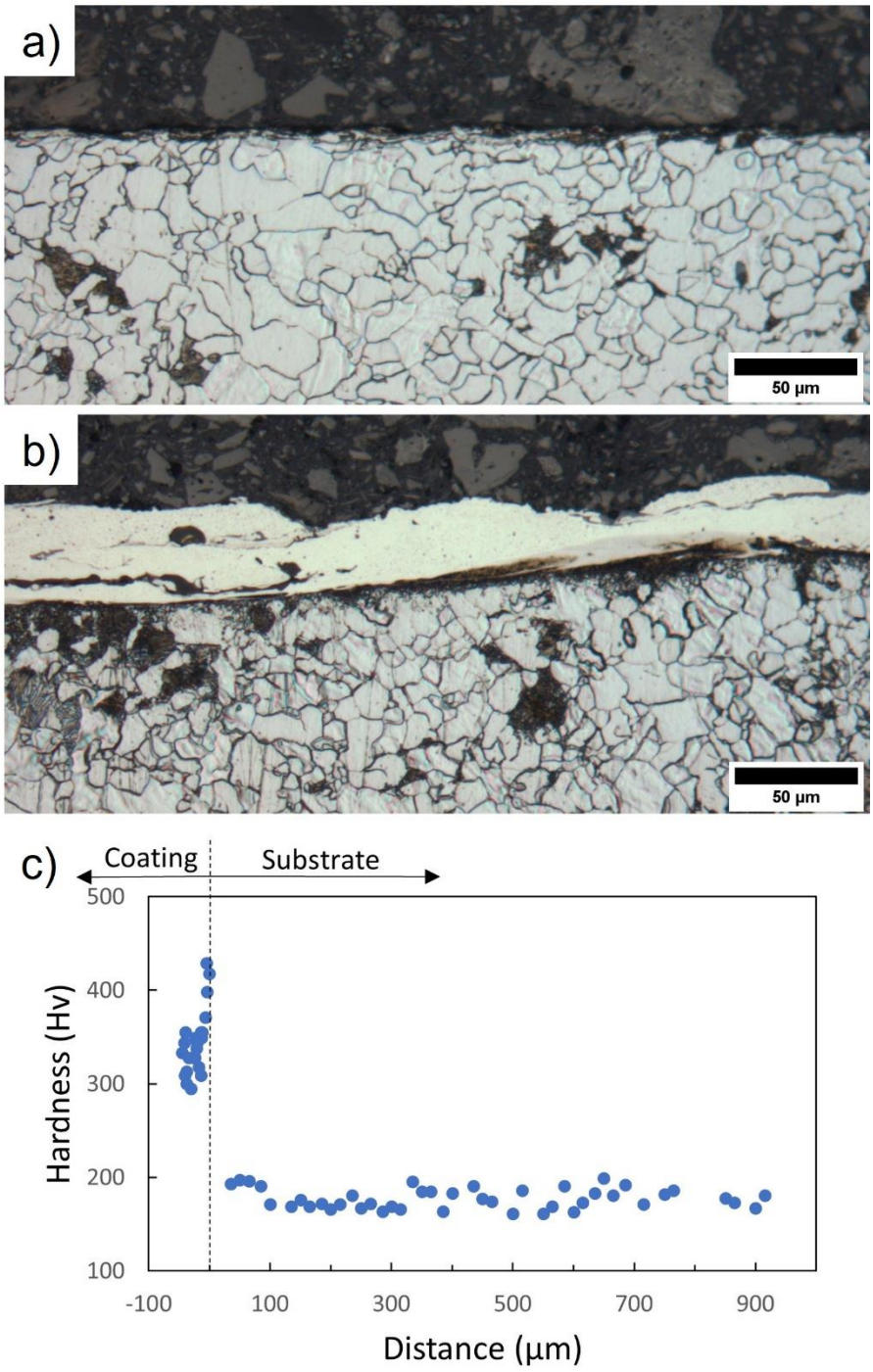

Figure 4-8 OM images of microstructure of a) A516 carbon steel substrate with and b) with coating; c) microhardness profile of coated sample on the substrate

4.3.4 Wear Property of Coatings

Fig. 4-9a and b show the wear tests performed on bare A516 carbon steel substrate. Wide and deep wear tracks are observed. The roughness measurement in Fig. 4-9c shows that the depth is approximately 11.5 μm. The X and Y axes are marked in Fig. 9c, and the height profiles at random Y are shown in Fig. 4-9d, and are used to determine that the width of the wear track is approximately 0.78 mm. The images show that the wear mechanism is likely abrasive, due to the much harder wear pin. The sides of the track edges are higher than the surrounding material due to the deformation of the coating by the wear pin. Fig. 4-9e and f show the wear test track on the polished surface of the MEA coated sample, a narrower and shallower track can be observed. The results of roughness in Fig. 4-9g indicates the maximum depth of tracks is approximately 2.5 μm, which is significantly smaller than that of without coating. The height profile of the sample surface at random X in Fig. 4-9h illustrates the width of the wear track is only 0.16 mm, which has a 79.49% reduction.

The specific wear rate coefficient can be calculated using $k_w=V/(FS)$,where V is the wear volume (mm^3), F is the applied normal load (N), and s is the length of the wear track (m). According to the measurements obtained in Fig. 8d and h, the k_w of the bare A516 substrate is 1.16×10^{-3} $mm^3/N\cdot m$; while the k_w of MEA coated sample is 5.16×10^{-5} $mm^3/N\cdot m$, which is much lower than that of the cast (2.51×10^{-4} $mm^2/N\cdot m$) [138], HVOF (3.74×10^{-4} $mm^3/N\cdot m$) [138], arc-melted (5.12×10^{-4} $mm^3/N\cdot m$) [140], and ball-milled (1.70×10^{-4} $mm^3/N\cdot m$) [139] MEA materials. The low wear rate may be due to the residual stresses generated during the ESPD process within the coating [141]–[144] and the refinement of the grain/subgrain [139], whereas this perspective needs a further study of the residual stress investigation. The two order of magnitude reduction in specific wear rate coefficient suggests that the coating material has a much higher wear resistance compared to the carbon steel substrate.

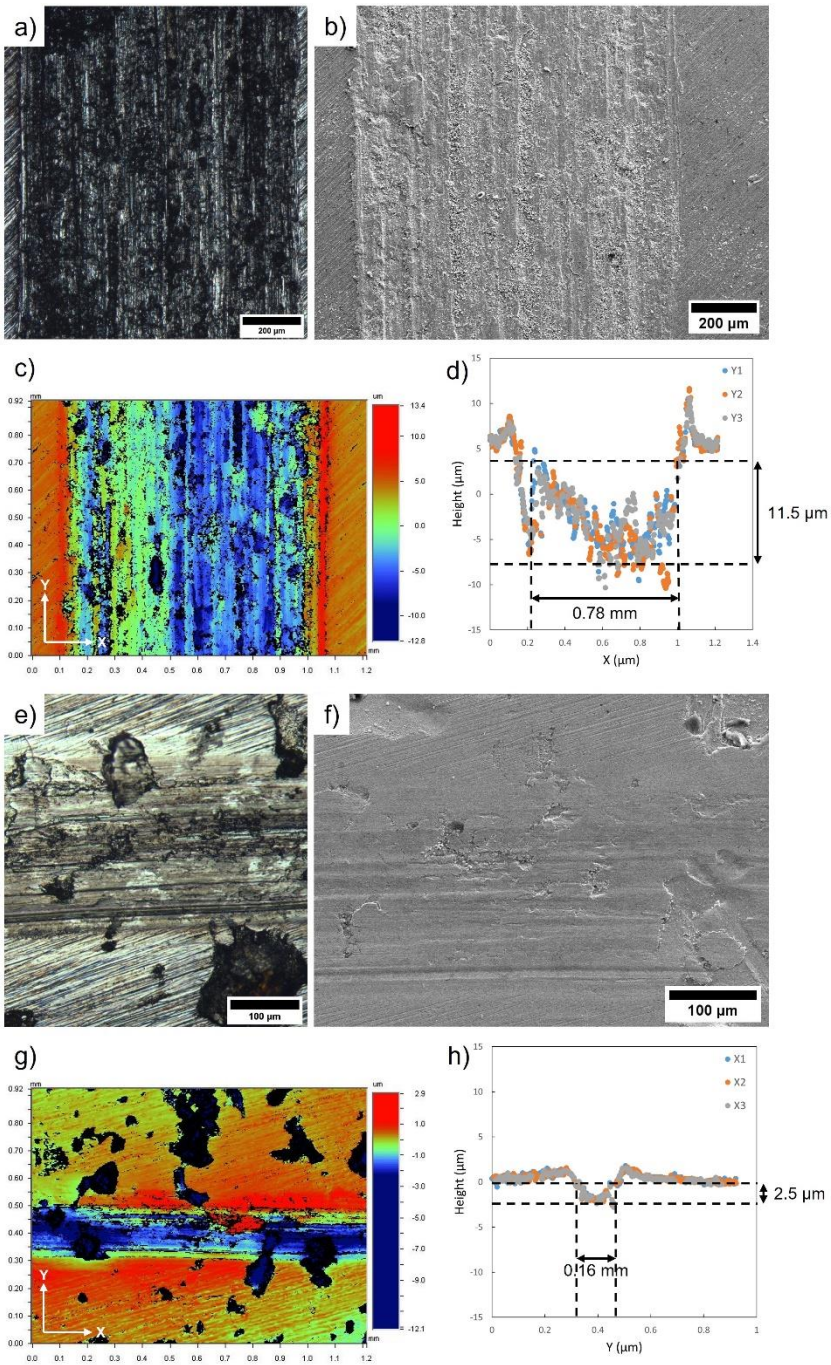

Figure 4-9 a) OM image and b) SEM image of linear wear track on the A516 steel substrate surface; c) roughness measurement of the wear track and d) its height profile at random Y; e) OM image and f) SEM image of linear wear track on coating surface; g) roughness measurement of the wear track and h) its height profile at random X

4.4 Summary

This study produced a high-quality MEA CrFeCoNi coating by depositing an elemental powder mixture slurry using ESD technology. The parameters of the deposition process were adjusted and optimized, including the selection of the ESD electrical parameters, the optimization of the composition of the different powders in the slurry, and the use of two ESD process parameters to reduce surface roughness. XRD and EDX analyses showed that the coatings produced were the desired CrFeCoNi equiatomic alloy, and the coatings were then characterized, including microstructure, microhardness, wear testing, and HAZ of the substrate.

- The proportion of power of each of the four constituent elements required to form an equiatomic CrFeCoNi alloy was successfully adjusted using an experimental approach. An initial coating performed with an equiatomic powder ratio identified low Cr and high Fe in the final coating, which was fixed after the initial powder ratio was adjusted with proportionally higher Cr and lower Fe.

- The microhardness of the coating was measured as 331.53±18.96 Hv, with columnar grains growing in the direction of deposition. This was significantly harder than the A516 carbon steel substrate (186±3.5 Hv) and is also harder than other reported literature values for CrFeCoNi. Microhardness profile and microstructural observations of the substrate showed minimum HAZ after ESD.

- The wear test results show that the CrFeCoNi alloy coating has higher wear resistance than the carbon steel substrate. Compared to the base material in this study, the CrFeCoNi coating effectively provides wear protection, with a 95.56% decrease in the specific wear rate.

Chapter 5

Application Trials of ESD Process for Coating

5.1 Repair of Damaged Thin Wall

5.1.1 Introduction

Aeroengines operate in extreme environments, including high temperatures, pressures, and centrifugal forces [145], [146], placing high demands on the strength of pump impellers and turbine blades. This results in exorbitant costs for manufacturing components in aircraft engines. Therefore, a reliable repair technique can be proposed for the restoration of damaged parts. One of the most common types of damage to pump impellers and turbine blades is associated with their thin-walled structures, which can be repaired using ESD.

5.1.2 Materials and Methods

A pump impeller [147]and a turbine blade [148] with thin walls were additive manufactured using the same printing method as described in Chapter 3 for repair demonstrations. The printed parts are shown in Fig. 5-1.

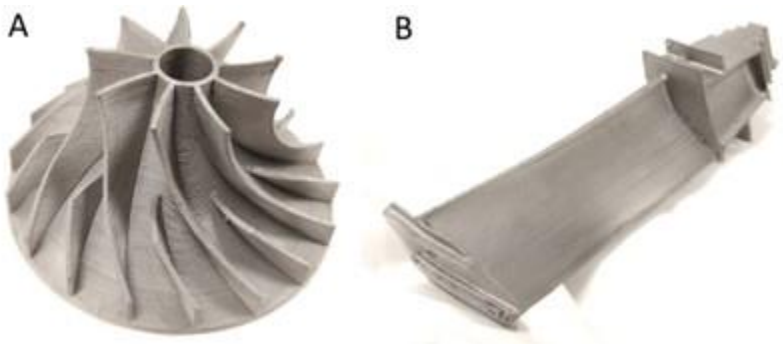

Figure 5-1 Additive manufactured a) pump impeller; and b) turbine blade

5.1.3 Repair of Thin-walled Additive Manufactured Parts

The parameter set G6 (120 μF, 80 V, 150 Hz) demonstrated a low defect rate, small HAZ formation in the substrate, limited dilution with the substrate during deposition, and acceptable deposition rates as already discussed in Chapter 3. To validate the effectiveness of the G6 parameter identified as a good

candidate for the thin wall repair of additive manufactured parts, the repair of two components was performed as demonstration. In situations where cracks or defects are detected on a component, material from the damaged region can be removed, as shown in Fig. 5-2b, e, f. Thus, the ESD electrode has sufficient room to perform the deposition. The pump impeller shown in Fig. 5-2a-d has wall thicknesses of 1 mm, and can be repaired without any significant challenges. The turbine blade shown in Fig. 5-2e-h is also successfully repaired in two locations, both with wall thicknesses of 1 mm. As can be seen from the repaired images, the depositions can be built up beyond the prior part dimensions, both in height and thickness. This would then require machining or grinding to restore the proper part dimensions to the desired tolerance.

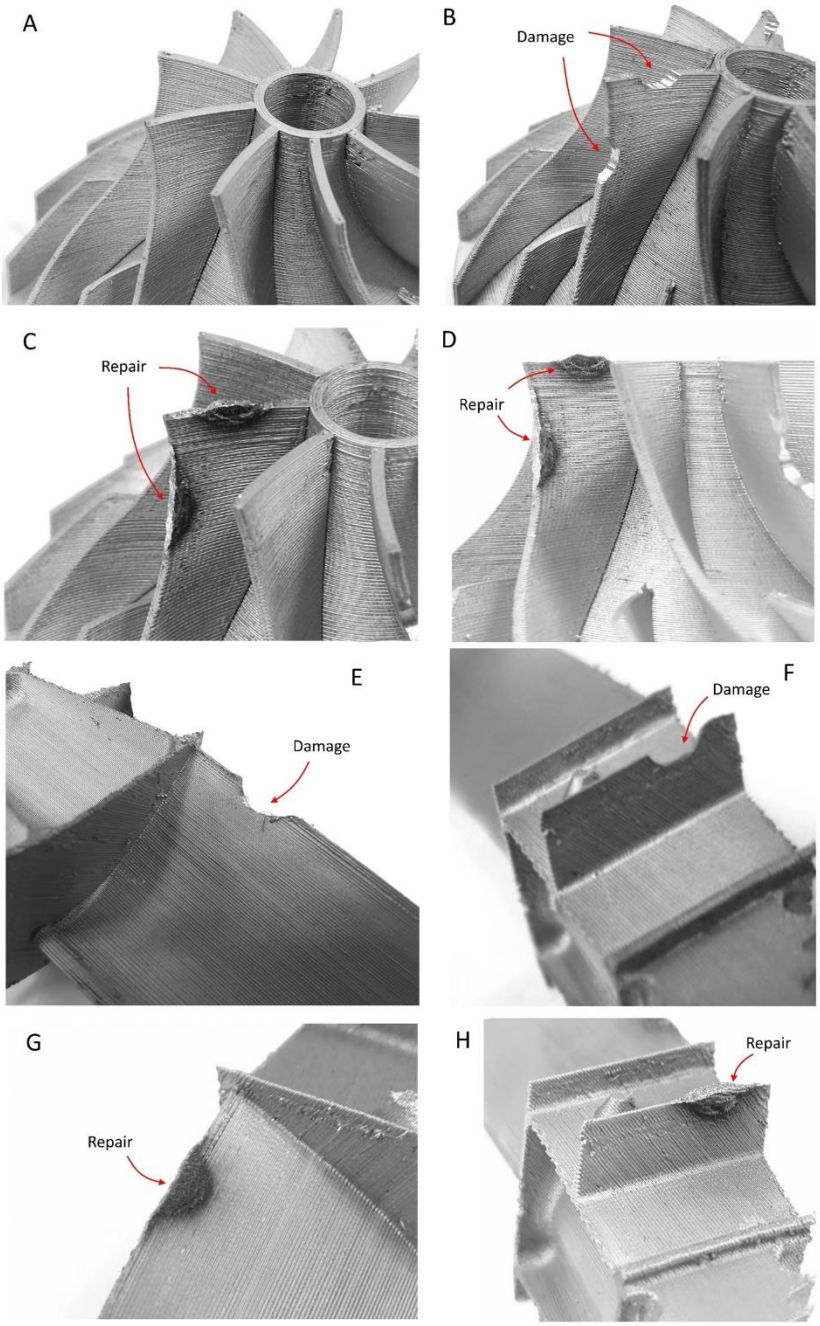

Figure 5-2 Demonstrations of a) pump impeller in original condition; b) damage introduced to blades; c, d) repaired impeller blades; e, f) damage introduced to turbine blade; g, h) repaired turbine blade

5.2 Thin Wall Deposition Using Automated ESD

5.2.1 Introduction

Three important electrical parameters, capacitance, voltage, and frequency in ESD were introduced in the literature review. However, the mechanical parameters also affect the quality of the deposition in the actual deposition process. During ESD, a dense layer of coating needs to have enough material to fill the entire space. When the travel speed increases, the number of discharge events in a unit space decreases, thus reducing the volume of material ejected from the electrode, preventing the coating from being filled and creating voids in the deposition [78]. The force between the electrode and substrate affects the gap of action during discharge, which is coupled with capacitance, and the transfer of electrode material becomes larger as the gap increases, peaking at a point equal to the arc gap and decreasing as the gap continues to increase [78, 91].

Pablo et al. [131] studied the fabrication of Inconel 718 coatings on Inconel 718 and 316L stainless steel substrates using automated ESD and investigated the effect of seven factors on the deposition rate: contact force, travel time, capacitance, voltage, frequency, rotation speed of the electrode and vibration or not. The results showed that voltage, capacitance, contact force, and travel speed had the greatest effect on the deposition rate, with the first three having a positive effect on the deposition rate and the higher travel speed decreasing the deposition rate. The other three parameters have almost no effect on deposition. In addition, the authors developed a mathematical model of the deposition of Inconel 718, which shows the equation with the four distinct parameters for the deposition rate (or deposition thickness). However, this model cannot be used in different cases, for example, it is only applicable to create deposition on wide planes, but not on thin walls. In Chapter 3, the thin wall is eroded at low pulse energy and power input, when it is changed from ESD to EDM, but effective deposition can be made on wide planes. In addition, this model is only for Inconel 718 coating, and the parameter relationships are applicable to other electrode materials but cannot be applied quantitatively. Therefore, it is only necessary to adjust the corresponding parameters when designing the experiment, such as reducing the travel speed, to obtain better quality deposition with high probability.

5.2.2 Materials and Methods

An automated ESD developed by Huys Inductries was used in this study, a photo of the automated ESD is shown in Fig. 5-3, which can not only control the electric parameters, but it can also adjust the

mechanical parameters such as travel speed and contacting force. In this study, a proper G-code was used to fabricate the buildup.

Figure 5-3 Photo of automated ESD developed by Huys Industries

Inconel 718 with a diameter of 1.8 mm was used as feedstock to fabricate buildup on additive manufactured thin walls of 17-4 stainless steel 0.5 and 1 mm thickness with electrical parameters 80 μF, 120 V, 150 Hz and 120 μF, 120 V, 150 Hz at mechanical parameters travel speed (3 mm/s) and contact force (5 g), respectively, and the parameters used are listed in Table 5-1. The electrode angles during deposition are shown in Fig. 5-3, with the travel direction perpendicular (Fig. 5-4a) and parallel (Fig. 5-4b) to the electrode.

Table 5-1 Parameters used for buildup using automated ESD

Parameter set #	Capacitance	Voltage	Frequency	Travel Speed	Contacting Force
P1	80 μF	120 V	150 Hz	6 mm/s	5g
P2	120 μF				

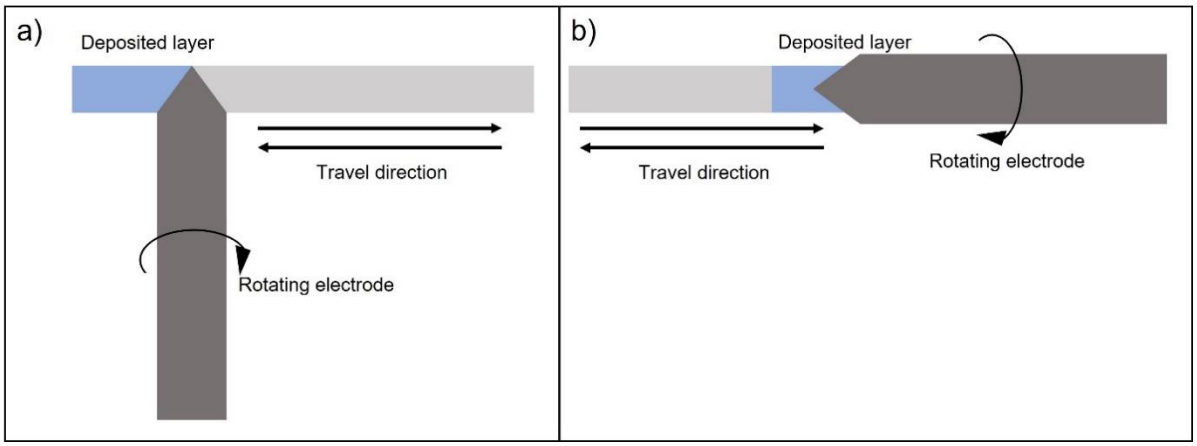

Figure 5-4 A brief sketch of deposition on thin wall with travel direction a) perpendicular, and b) parallel to the electrode.

5.2.3 Results and Discussion

Due to the controlled stable electrode traveling, the width of the buildup was about 0.5 mm, which means the deposition cannot cover the whole surface of the 1 mm wall, therefore, the 0.5 mm wall was used for automated trials. The as-deposited buildup is shown in Fig. 5-5

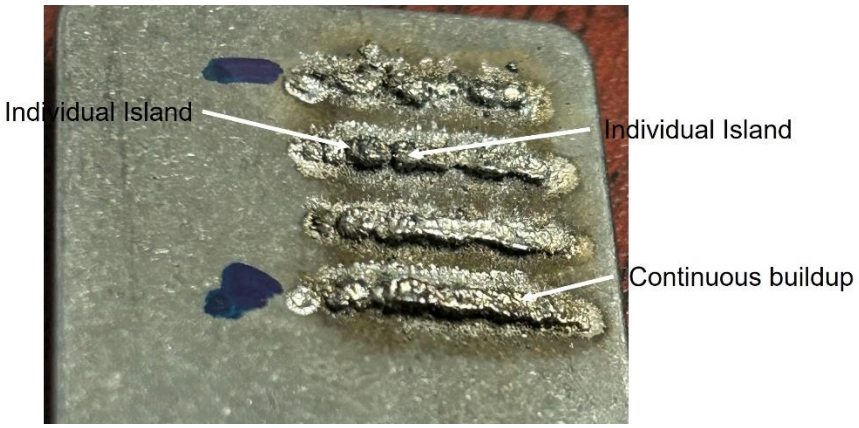

Figure 5-5 Photo of Buildup made by automated ESD, results in island shape with travel method in Fig. 5-4a, and continuous buildup with the travel method in Fig. 5-4b

The buildup made by the deposition method in Fig. 5-3a is shown in the sketch in Fig. 5-4a. When the electrode is perpendicular to the deposition direction, the contact between the rotating electrode and the substrate surface is not even enough, and the deposition is carried out when it is in contact and not when it is overhanging, creating a gap in between. The electrodes cannot fill the gaps when they are smaller

than the electrode size, making the coating form separate islands, which is not desired. In contrast, when the electrode is parallel to the deposition direction (Fig. 5-3b), because the electrode tip is conical, so that when the electrode is in contact with the substrate, there is a repeat contact area as shown in Fig. 5-4b, thus avoiding the problem of uneven contact, and thus getting an effective buildup.

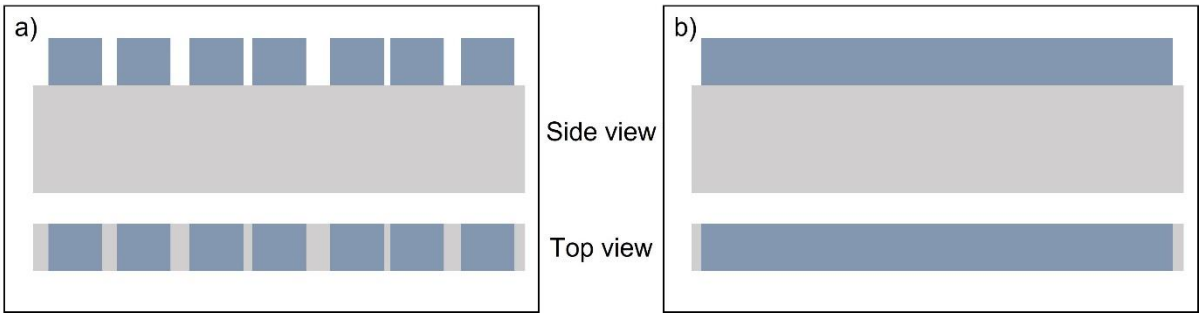

Figure 5-6 A sketch of as-deposited layer deposited with a) perpendicular deposition method, with formation of island, and b) parallel deposition method, with formation of continues and smooth buildup.

The images of the cross-section of the manual deposition and the automated deposition are shown in Fig. 5-5 with the parameter sets of P1 and P2. For P1, the shapes of defects in the automated ESD sample are mainly circles (Fig. 5-5a), which are different from the defect in manual ones, the elongated defects (Fig. 5-5b). The form of defect in the automated coating is mainly the voids, which show an incompatibility of the energy/power input and the travel speed. As for P2, the quality of the automated ESD is a lot higher with almost no defect (Fig. 5-5c), whereas the manual deposition has a defect of over 4% (Fig. 5-5d). The deposition rate of P2 can reach about 600 μm/min. The hardness of the coating was about 370 Hv, which strongly satisfies the quality of the application.

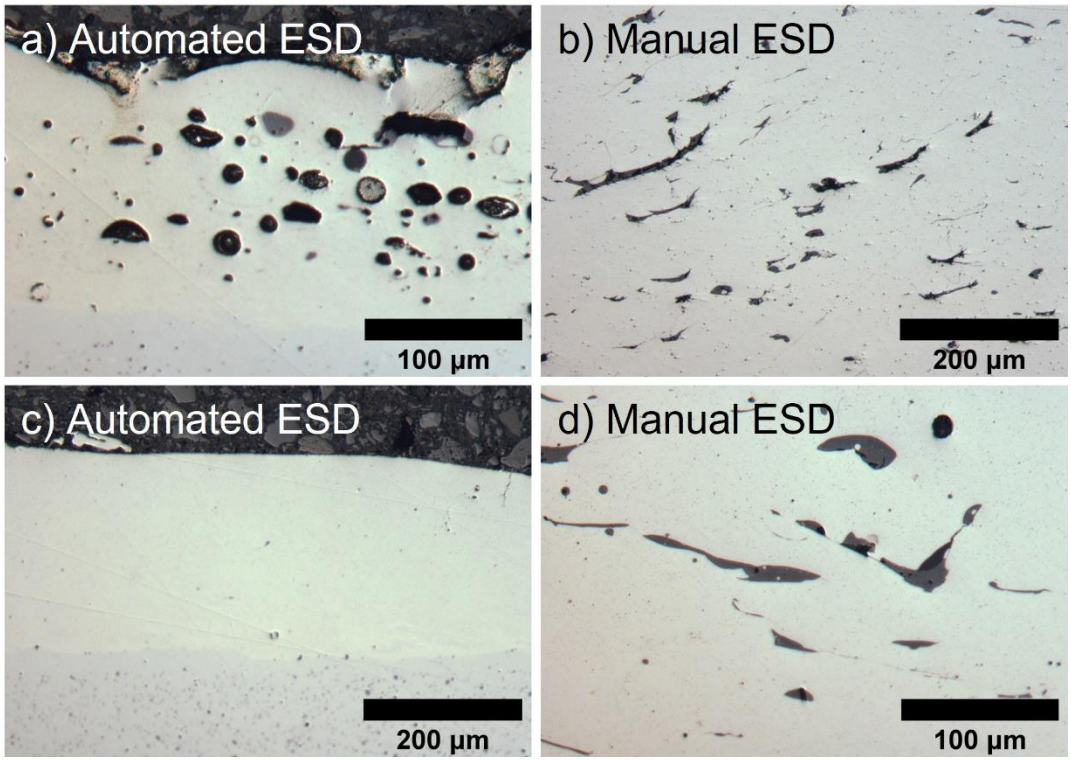

Figure 5-7 Cross-section images of manual ESD and automated ESD on 0.5 mm wall with parameter set P1 using a) automated ESD and b) manual ESD; parameter sets P2 using c) automated ESD and d) manual ESD

5.3 AlCrFeCoNi Coating using ESD

5.3.1 Introduction

The 3d transition metal HEAs have high fracture toughness [6], yield strength, and specific strength compared to conventional alloys [32]. Research into coatings is also in constant need of innovation, as the surface of the workpiece is in direct contact with the environment and its surface properties determine the service life of the workpiece. To further improve the properties and application areas for current engineering alloys, new coating design and process are needed. Among different coating techniques, a micro-welding technique known as electro-spark deposition (ESD) has the ability to coat any conduct materials onto workpieces in a low cost. The ESD process makes use of a consumable electrode to deposit material on a conductive substrate through the creation of a momentary short circuit. The momentary nature of the electric arcing and the small area impacted on the substrate results in very little heat transfer to the substrate. The minimized HAZ and the formation of true metallurgical bonding

between the deposited material and substrate make ESD an attractive option for coating on engineering alloys. The coatablity of HEAs using ESD is still lack of unstanding.

Here, in this work ESD is used to fabricate AlCoCrFeNi HEA coatings on conventional alloys, eg., steel. It aims to understand the weldability of HEA with conventional engineering alloy.

5.3.2 Materials and Methods

The A516 medium carbon steel and Inconel 718 substrate were used in this study, and 3.18-mm AlCrFeCoNi electrodes cut by wire-EDM were used as the coating material. The rust on the steel substrate was removed and the surface was flattened and cleaned in ethanol using an ultrasonic cleaner. The coating was then directly applied onto the steel surface, using a manual ESD machine manufactured by Huys Industries. The process parameters range adjusted in this study is shown in Table 5-2.

Table 5-2 ESD parameters studied of HEA deposition

Factors	Values
Capacitance (μF)	80 - 150
Voltage (V)	60 - 120
Frequency (Hz)	100 - 200

The cross-section morphology of the coated samples was evaluated using an Olympus BX51M optical microscope. a Zeiss UltraPlus Field Emission scanning electron microscope (FE-SEM) with an AMETEK EDAX Apollo XL energy-dispersive X-ray spectroscope (EDX) attachment was used for SEM and EDX analysis. The Microhardness was measured by a Clemex CMT (v. 8.0.197) with a force load of 25 g and a dwell time of 10 s. A linear wear tester was used to perform the wear test with a force load of 988.9 g for 200 cycles (400 passes) with 7 mm of travel distance per pass.

5.3.3 Results and Discussion

The cross-section of the AlCrFeCoNi HEA coating on different substrates is shown in Fig. 5-8. Fig. 5-8a and c show the cross-section on Inconel 718 and steel after polishing, respectively. The morphology of the coating and the substrate are significantly different, making the interface easily distinguishable. The mechanism of the ESD is the melting, transfer, and solidification of the electrodes, during which the material shrinks, causing cracks to form in the coating on both substrates. In addition, because of the high temperatures during the generation of electrical sparks, certain elements in the material are

oxidized and these oxides are trapped in the coating, which is another type of defect. In this HEA, Al is the main oxidized element. The cross-section after etching is shown in Fig. 5-8b and d, where the HEA coating and the substrate can be clearly identified from the microstructure. The grains of the coating on both substrates are columnar and penetrate from the coating-substrate interface right up to the outer surface of the coating. This is because during the solidification of the material because of supercooling, resulting in columnar grains [69].

The microstructure of the interface is significantly different on different substrates. For the HEA coating on Inconel 718, the microstructure does not have much difference throughout the whole coating from the interface to the top of the coating. Whereas the microstructure of coating on steel near the interface has different morphology compared to the far side of the interface, which shows a great influence of diluted iron from the substrate.

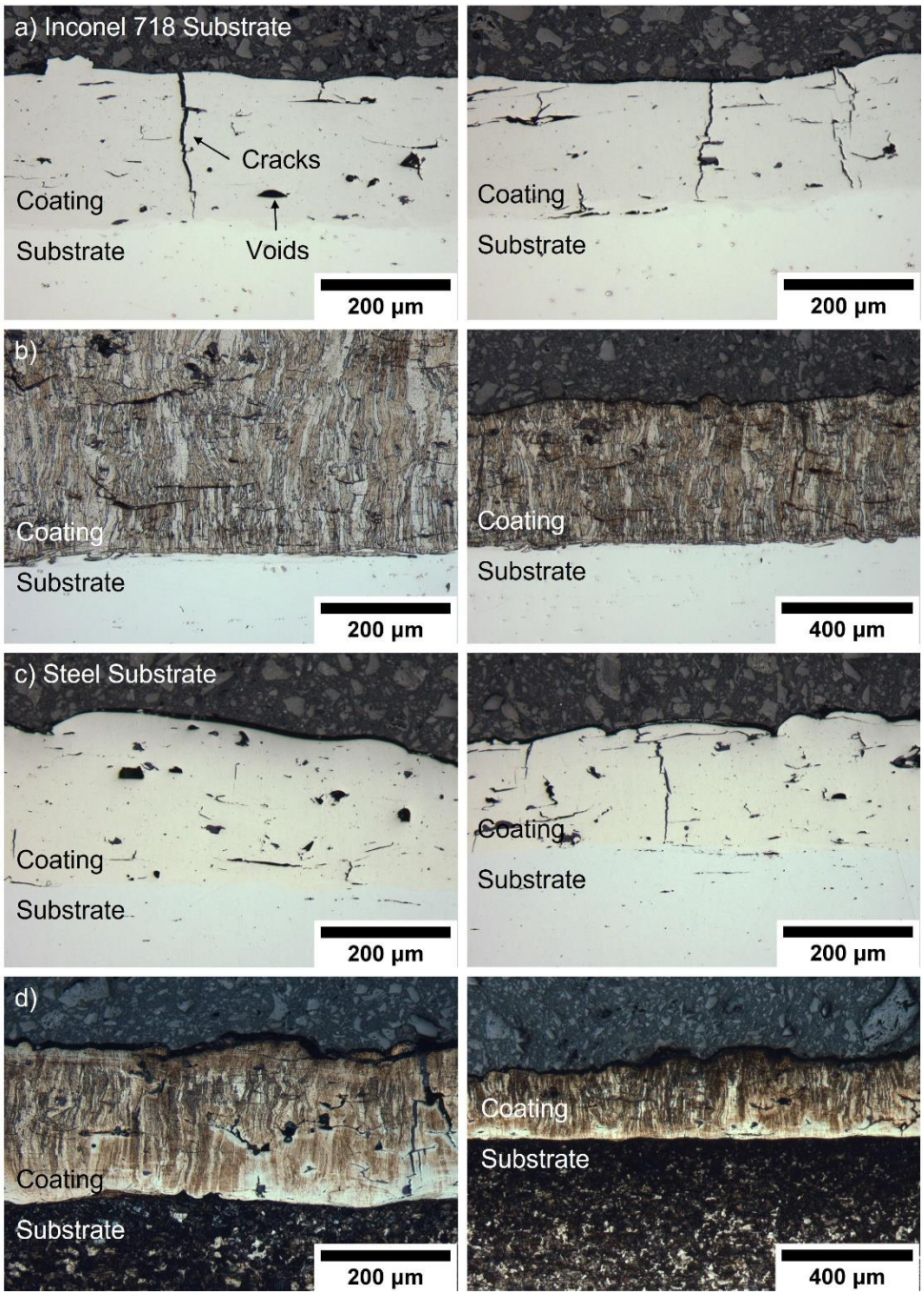

Figure 5-8 OM images of cross-section of a) rough-polished and b) etched sample

A cross section of the AlCrFeCoNi HEA coating and substrate is shown in Fig. 5-9. 20% of the atomic fraction of Al, Cr, Fe, Co and Ni are present in the coating. The concentration of elements in substrate

increases near the interface, confirming the composition near the interface is a more complicated region (Ni-rich on Inconel 718 substrate, and Fe-rich on steel substrate).

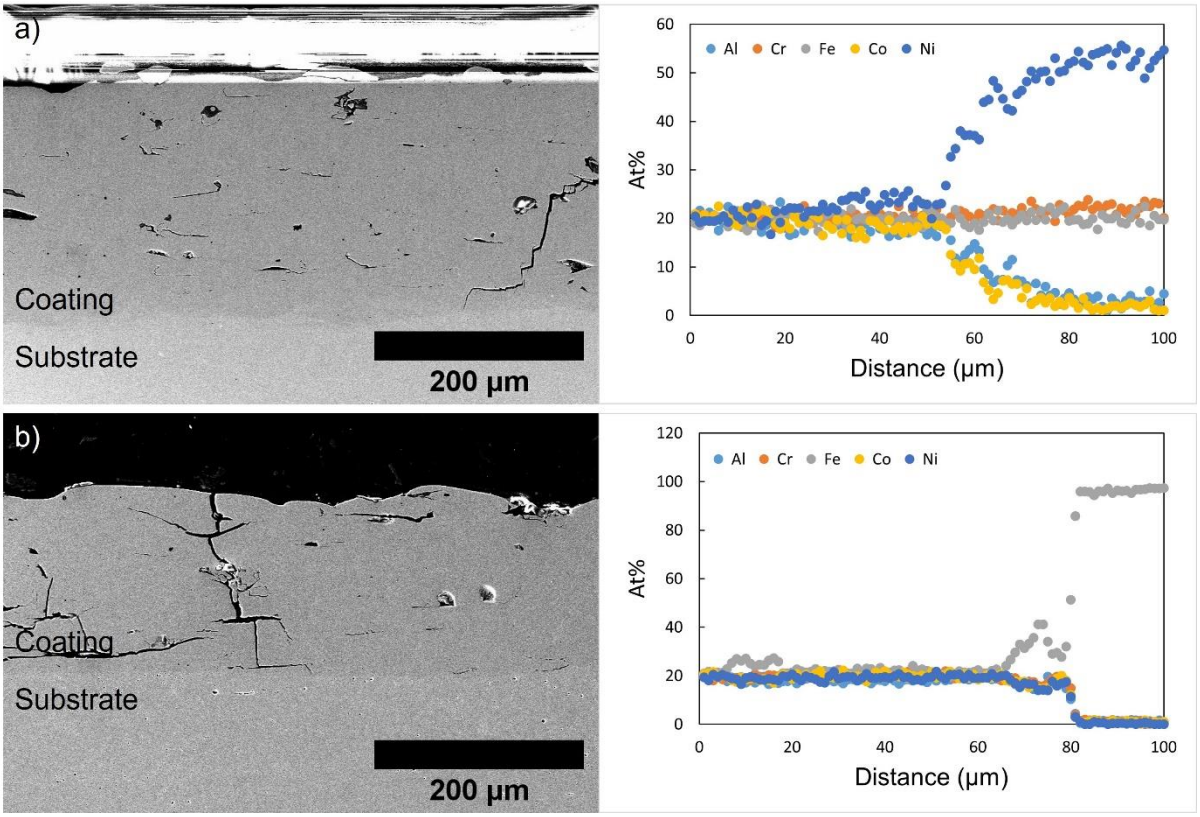

Figure 5-9 SEM of cross-section and the EDX line scan of AlCrFeCoNi HEA coating on a) Inconel 718 and b) steel

The microhardness profile is shown in Fig. 5-10. The negative and positive sides indicate the distance of indentation in the coating and substrate, respectively, from the interface. The hardness of this HEA coating is approximately 540 Hv, which is significantly less than that of the casted HEA [92], which might be due to the substrains in cast HEA. The microhardness in the coating near the interface gradually decreases and reaches the hardness of Inconel 718 and steel substrate, approximately 260 Hv and 145 Hv, respectively. No increase in interfacial microhardness is observed, indicating that no intermetallic compounds are formed.

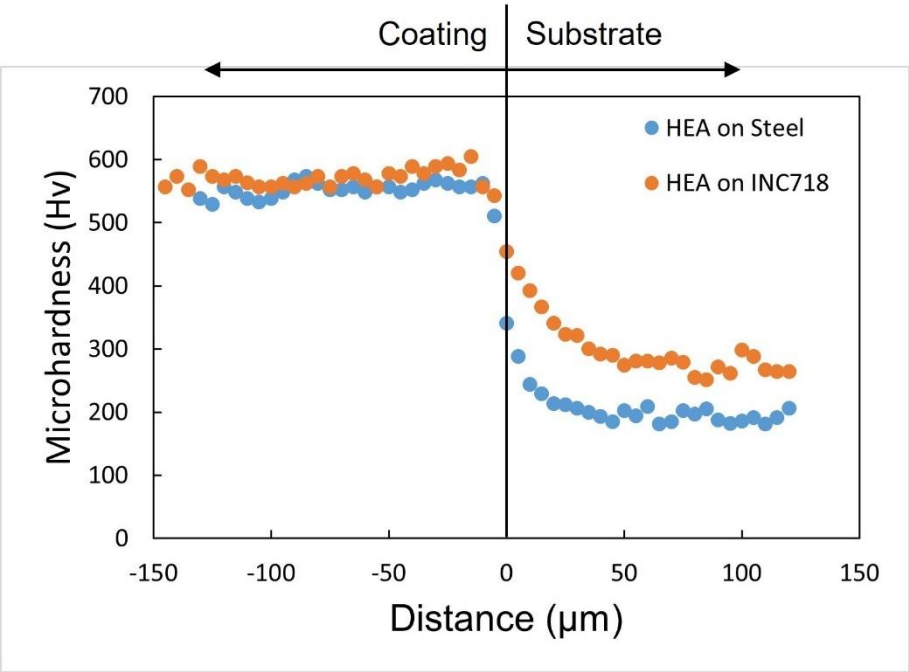

Figure 5-10 Microhardness profile of HEA coating

Fig. 5-11 shows the wear tests performed on deposited AlCrFeCoNi coating and on bare Inconel 718. The roughness measurement in Fig. 5-11a and b, c and d show the surface roughness mapping of the wear track and depth profile on HEA coating and on Inconel 718, respectively. The HEA coating has the wear track depth of approximately 7.7 μm, and the width of the wear track is approximately 0.2 mm. Compared to the wear test on Inconel 718 and steel substrate shown in Fig. 5-11 c and d, and Fig. 4-9c and d, respectively, the depth have a reduction of 35% and 33%, the depth and width have a reduction of 56% and 74%, respectively.

The calculated specific wear rate is 1.97×10^{-4} $mm^3/(Nm)$, which has a reduction of 83% and 72% compared to the steel substrate (1.16×10^{-3} $mm^3/N\cdot m$), and Inconel 718 substrate (6.97×10^{-4} $mm^3/N\cdot m$), the comparison of wear rate, wear track depth and width are shown in Fig. 5-12. The wear rate is significantly higher than that of vacuum arc melted AlCrFeCoNi [149], [150], laser cladding coated AlCrFeCoNi [151], and HVOF with spark plasma sintered AlCrFeCoNi [152]. The main factor of higher wear rate may be the tensile residual stresses in ESD-coated AlCrFeCoNi, which reduces the wear resistance.

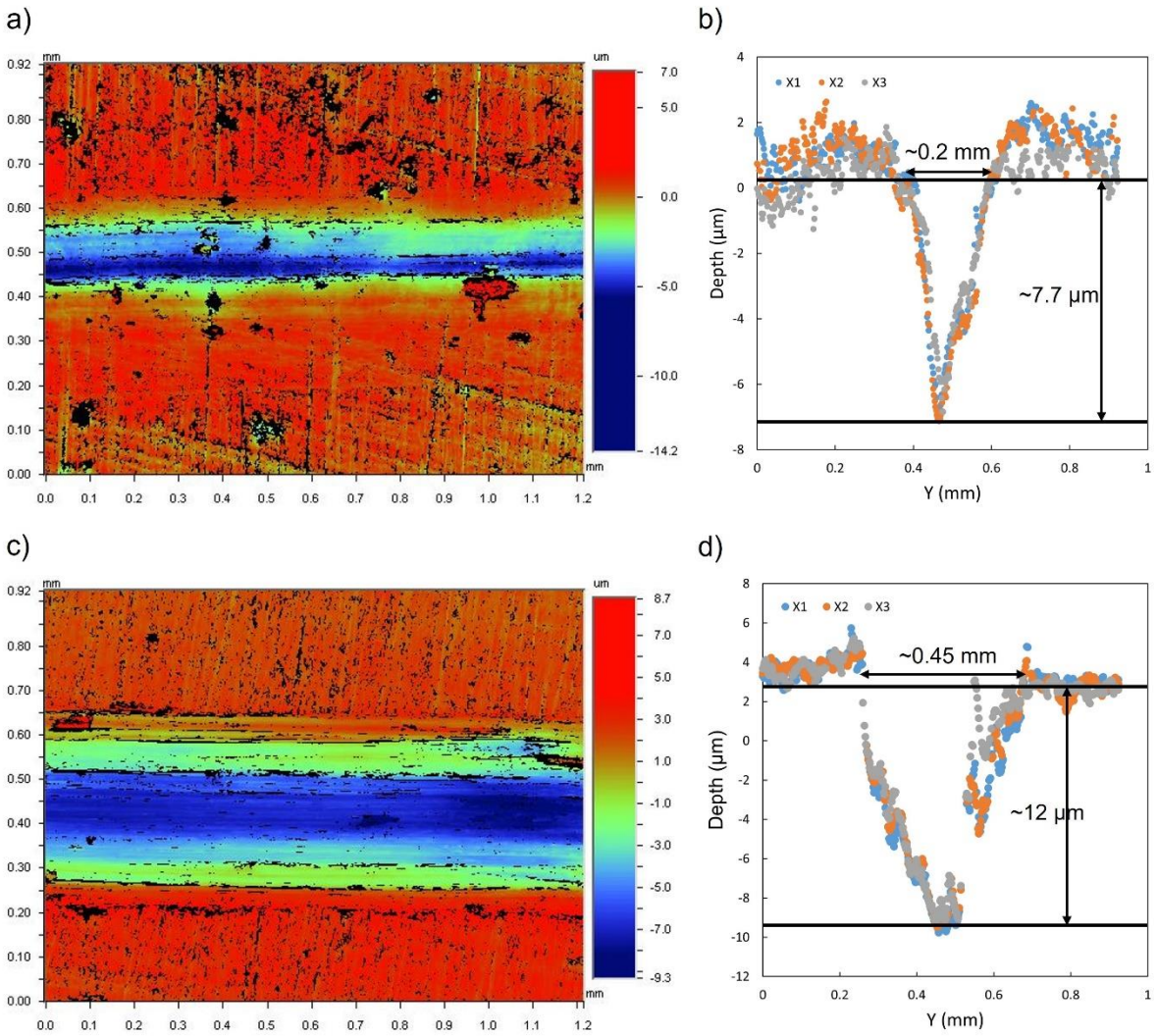

Figure 5-11 Roughness measurement of the wear track of a) AlCrFeCoNi coating and b) the height profile at random X, and the wear track of c) bare Inconel 718 substrate and e) the height profile at random X

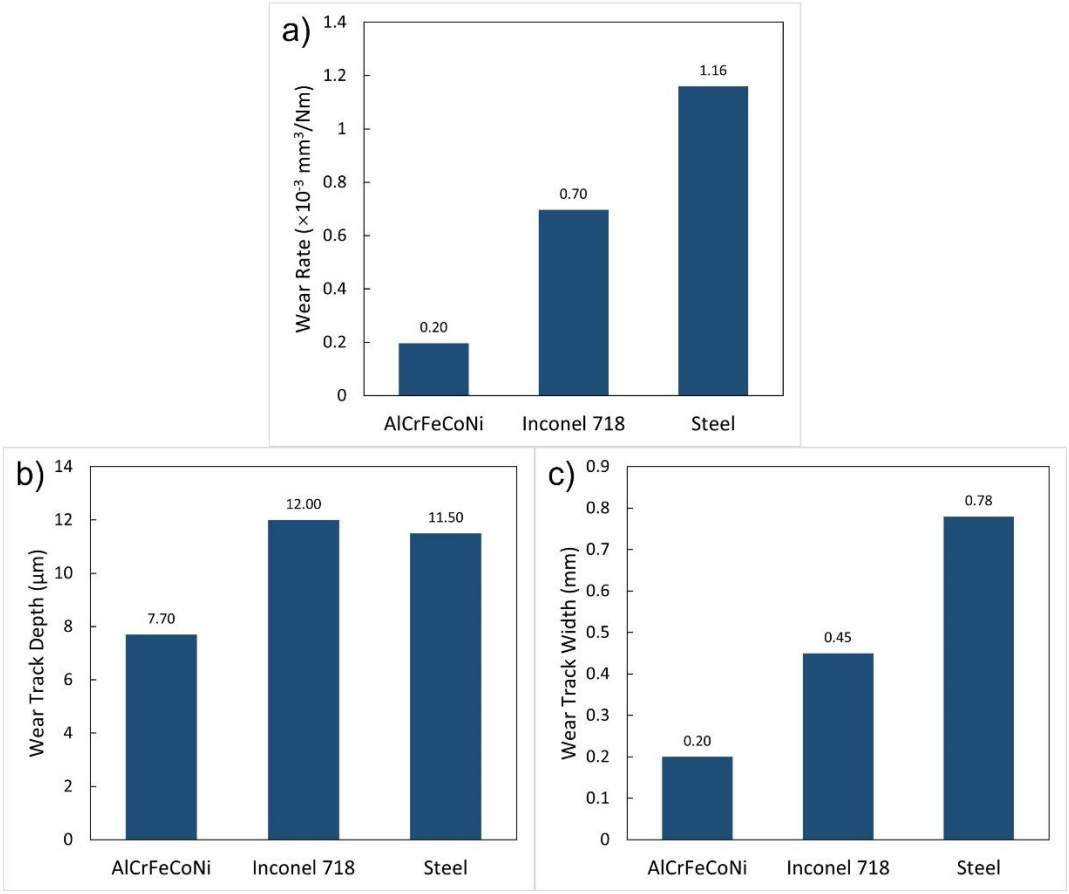

Figure 5-12 Comparison of a) wear rate; b) wear track depth; and c) wear track width on AlCrFeCoNi, bare Inconel 718 and steel

5.4 Summary

In this chapter, the repair of additive manufactured thin-walled notches was performed using the parameters selected in Chapter 3. Additionally, attempts were made to apply automated ESD on thin-walled structures. Furthermore, the fabrication of HEA coatings using ESD was explored, followed by preliminary characterization.

- Automation ESD demonstrated opposite results compared to the manual ESD. With the compatibility between the electric parameters and engineering parameters, the quality of the coating can significantly increase, and the trade off between the deposition rate and defect was negligible, high deposition rate and low defect can be reached, the former can reach to over 600

μm/min, and the defect (void + oxidation) can be minimized to zero based on the optical microscopy images.

- The primary results show the weldability of AlCrFeCoNi HEA onto Inconel 718 and steel through the study of the cross-section, including the OM and SEM images, and EDX analysis. The HEA coating has a very high microhardness and wear resistance compared to the chosen substrate, which can effectively protect the substrate material. For further investigation, tests strength of the interface, and corrosion resistance of this HEA coating will be performed to fill the gap of this HEA coating.

Chapter 6

Conclusion

6.1 Conclusion

The purpose of this thesis is to explore the extended use of ESD beyond the fabrication of coatings and simple repair. This includes the fabrication of effective buildup on thin-walled structures and the fabrication of intuitive alloy coatings using metal powder as a raw material. The results of these two studies demonstrate the flexibility of ESD that can be developed in a wider range of fields.

Fabricating deposition on thin walls is far different from fabricating it on a flat surface because the smaller contact area and smaller volume of a thin-walled structure result in a lower heat transfer efficiency. The melting of the substrate during the deposition process has a slower solidification rate at low thermal transfer efficiency, making it easier for the melted material (substrate and electrode) to splash away with the rotating electrode, rather than transferring and solidifying onto the part, where erosion of the substrate can be observed, resulting in secondary damage to the parts. Therefore, the technical way to is to increase the pulse energy so that more electrode material is melted with each pulse, offsetting the splashed molten material. Increasing the pulse energy enhances the deposition rate, but it also brings disadvantages. The high temperatures during Inconel 718 deposition cause the material to oxidize, forming oxides of aluminum and titanium, which are the main defects in accumulation. At properly reduced pulse energies, the electrode material melted per pulse is not enough to fill the entire space, creating voids in the deposition and making them a major defect in the buildup. Therefore, the investigation of a balance between them is important in industrial production. The fabrication of the buildup requires a long deposition period, and this process can be considered as a heat treatment of the deposited layer. From the analysis of the microstructure, it can be observed that the closer the substrate/deposition interface, or the higher the pulse energy, the coarser the subgrains, which can also be carried out by microhardness measurements. This report also discusses the feasibility of repairing thin-walled notches with automatic ESD, and the results show that a high-quality buildup can be obtained with automatic ESD, which requires a balance of electrical and mechanical parameters.

Conventional ESD uses electrode rods as the feedstock and the target material to create the coating because the composition of the elements in the alloy is difficult to control and needs to distribute

uniformly, which often requires multiple heat treatment processes to facilitate the element diffusion in the solid solution. However, the content of some alloys is more intuitive, a typical example is the equiatomic M/HEA. In this study, single-element metal powders Cr, Fe, Co, and Ni were used as feedstock, mixed and painted to the substrate surface in the form of slurry, and pure tungsten was used as the electrode to melt the powders by the high temperature generated during ESD, which fused and solidified on the substrate surface. This technique requires the optimization of the deposition process to obtain a high-quality coating, for example, low pulse energies cause the powder to melt insufficiently, while higher pulse energies cause the electrode material to melt and attach to the coating, therefore, a moderate parameter set needs to be proposed. In addition, the melted powders are also deposited on the electrode during the deposition process, thus, the electrode can then be treated as the target material and the electrode is therefore used to form the last layer to smoothen the coating surface. The mechanism of melting and solidification of powder and electrode is different, which is why the microstructure of ESPD and ESED layers are different during microstructure analysis. And the ESED layer and interlayer cannot be indexed in the EBSD results, the former may be due to the higher tensile residual stresses. The latter may be due to the formation of intermetallic compounds in the interlayer as a rise of microhardness at the interlayer is measured.

This report also briefly discusses the direct fabrication of coatings with AlCrFeCoNi HEA electrodes. The wide range of ESD applications allows almost any material to be fabricated as a coating, which extends the research direction to HEAs.

6.2 Future Work

The buildup of thin-walled structures can be manufactured with automatic ESD, as it can control the variables like travel speed of the electrodes, and the contact force, so that they can be fully coordinated with the electrical parameters to obtain a low defect and high deposition rate buildup.

The study of powder deposition presents a new approach to the fabrication of MEA and HEA coatings that takes full advantage of the flexibility and diversity in the composition of these alloys. Beneficial properties of the component elements can be obtained in the final coating by the melting and in-situ combination of the individual elements in powder form during ESD.

In addition, research directions that have been incorporated into the plan include, but are not limited to, fabrication of HEA coatings as an interlayer in resistance spot welding (RSW) to reduce possible

intermetallic compounds; post-processing, and coating fabrication on additive manufactured parts for additional properties; multilayer deposition of 3d metal HEA and refractory metals/alloys (e.g., WC, Nb, Mo) to obtain new coating systems, and etc.

References

[1] J. Bennett *et al.*, "Repairing Automotive Dies with Directed Energy Deposition: Industrial Application and Life Cycle Analysis," *Journal of Manufacturing Science and Engineering, Transactions of the ASME*, vol. 141, no. 2, Feb. 2019, doi: 10.1115/1.4042078.

[2] M. P. Nascimento and H. J. C. Voorwald, "Considerations About the Welding Repair Effects on the Structural Integrity of an Airframe Critical to the Flight-Safety," in *Procedia Engineering*, Apr. 2010, pp. 1895–1903. doi: 10.1016/j.proeng.2010.03.204.

[3] M. P. Nascimento, H. J. C. Voorwald, and J. D. C. Payão Filho, "Fatigue Strength of Tungsten Inert Gas-Repaired Weld Joints in Airplane Critical Structures," *J Mater Process Technol*, vol. 211, no. 6, pp. 1126–1135, Jun. 2011, doi: 10.1016/j.jmatprotec.2011.01.016.

[4] V. Champagne, M. Pepi, and B. Edwards, "Electrospark Deposition for the Repair of Army Main Battle Tank Components," 2006.

[5] J. W. Yeh *et al.*, "Nanostructured High-Entropy Alloys with Multiple Principal Elements: Novel Alloy Design Concepts and Outcomes," *Adv Eng Mater*, vol. 6, no. 5, pp. 299–303, 2004, doi: 10.1002/adem.200300567.

[6] M. H. Tsai and J. W. Yeh, "High-Entropy Alloys: A Critical Review," *Mater Res Lett*, vol. 2, no. 3, pp. 107–123, 2014, doi: 10.1080/21663831.2014.912690.

[7] P. L. Fauchais, J. V. R. Heberlein Maher, and I. Boulos, "Thermal Spray Fundamentals From Powder to Part."

[8] Lech. Pawłowski, *The science and engineering of thermal spray coatings*. Wiley, 2008.

[9] I. D. Utu, G. Marginean, I. Hulka, V. A. Serban, and D. Cristea, "Properties of the thermally sprayed Al2O3-TiO2 coatings deposited on titanium substrate," *Int J Refract Metals Hard Mater*, vol. 51, pp. 118–123, 2015, doi: 10.1016/j.ijrmhm.2015.03.009.

[10] A. Ibrahim, R. S. Lima, C. C. Berndt, and B. R. Marple, "Fatigue and mechanical properties of nanostructured and conventional titania (TiO2) thermal spray coatings," *Surf Coat Technol*, vol. 201, no. 16–17, pp. 7589–7596, May 2007, doi: 10.1016/j.surfcoat.2007.02.025.

[11] M. Szala, L. Łatka, M. Awtoniuk, M. Winnicki, and M. Michalak, "Neural modelling of aps thermal spray process parameters for optimizing the hardness, porosity and cavitation erosion

resistance of al2o3-13 wt% tio2 coatings," *Processes*, vol. 8, no. 12, pp. 1–15, Dec. 2020, doi: 10.3390/pr8121544.

[12] J. Voyer, P. Schulz, and M. Schreiber, "Conducting flame-sprayed Al coatings on textile fabrics," *Journal of Thermal Spray Technology*, vol. 17, no. 4, pp. 583–588, 2008, doi: 10.1007/s11666-008-9213-1.

[13] R. Beydon, G. Bernhart, and Y. Segui, "Measurement of metallic coatings adhesion to fibre reinforced plastic materials," 2000.

[14] A. Liu, M. Guo, M. Zhao, H. Ma, and S. Hu, "Arc sprayed erosion-resistant coating for carbon fiber reinforced polymer matrix composite substrates," *Surf Coat Technol*, vol. 200, no. 9, pp. 3073–3077, Feb. 2006, doi: 10.1016/j.surfcoat.2005.01.042.

[15] L. Y. Sheng, C. Lai, F. Yang, Q. L. Wang, and T. F. Xi, "Microstructure and wear behaviour of ceramic particles strengthening NiAl based composite," in *Materials Research Innovations*, Maney Publishing, Jul. 2014, pp. S4544–S4549. doi: 10.1179/1432891714Z.000000000738.

[16] O. Poliarus *et al.*, "Effect of Powder Preparation on the Microstructure and Wear of Plasma-Sprayed NiAl/CrB2 Composite Coatings," *Journal of Thermal Spray Technology*, vol. 28, no. 5, pp. 1039–1048, Jun. 2019, doi: 10.1007/s11666-019-00861-5.

[17] H. S. Grewal, H. Singh, and A. Agrawal, "Microstructural and mechanical characterization of thermal sprayed nickel-alumina composite coatings," *Surf Coat Technol*, vol. 216, pp. 78–92, Feb. 2013, doi: 10.1016/j.surfcoat.2012.11.029.

[18] H. Jamali, R. Mozafarinia, R. Shoja Razavi, and R. Ahmadi-Pidani, "Comparison of thermal shock resistances of plasma-sprayed nanostructured and conventional yttria stabilized zirconia thermal barrier coatings," *Ceram Int*, vol. 38, no. 8, pp. 6705–6712, Dec. 2012, doi: 10.1016/j.ceramint.2012.05.060.

[19] F. Zhou, Y. Wang, L. Wang, Z. Cui, and Z. Zhang, "High temperature oxidation and insulation behavior of plasma-sprayed nanostructured thermal barrier coatings," *J Alloys Compd*, vol. 704, pp. 614–623, 2017, doi: 10.1016/j.jallcom.2017.02.073.

[20] A. K. Basak, P. Matteazzi, M. Vardavoulias, and J. P. Celis, "Corrosion-wear behaviour of thermal sprayed nanostructured FeCu/WC-Co coatings," *Wear*, vol. 261, no. 9, pp. 1042–1050, Nov. 2006, doi: 10.1016/j.wear.2006.03.026.

[21] B. Swain, S. Mantry, S. S. Mohapatra, S. C. Mishra, and A. Behera, “Investigation of Tribological Behavior of Plasma Sprayed NiTi Coating for Aerospace Application,” *Journal of Thermal Spray Technology*, vol. 31, no. 8, pp. 2342–2369, Dec. 2022, doi: 10.1007/s11666-022-01452-7.

[22] A. Thibblin and U. Olofsson, “A study of suspension plasma-sprayed insulated pistons evaluated in a heavy-duty diesel engine,” *International Journal of Engine Research*, vol. 21, no. 6, pp. 987–997, Aug. 2020, doi: 10.1177/1468087419879530.

[23] M. Hasan, J. Stokes, L. Looney, and M. S. J. Hashmi, “Deposition and characterization of HVOF thermal sprayed functionally graded coatings deposited onto a lightweight material,” *J Mater Eng Perform*, vol. 18, no. 1, pp. 66–69, Feb. 2009, doi: 10.1007/s11665-008-9251-3.

[24] H. Wu and D. Kong, “Effects of laser power on friction–wear performances of laser thermal sprayed Cr3C2–NiCr composite coatings at elevated temperatures,” *Opt Laser Technol*, vol. 117, pp. 227–238, Sep. 2019, doi: 10.1016/j.optlastec.2019.04.022.

[25] D. Merino-Millan, C. J. Múnez, M. Á. Garrido-Maneiro, and P. Poza, “Alternative low-power plasma-sprayed inconel 625 coatings for thermal solar receivers: Effects of high temperature exposure on adhesion and solar absorptivity,” *Solar Energy Materials and Solar Cells*, vol. 245, Sep. 2022, doi: 10.1016/j.solmat.2022.111839.

[26] S. Kaur, N. Bala, and C. Khosla, “Characterization of Thermal-Sprayed HAP and HAP/TiO2 Coatings for Biomedical Applications,” *Journal of Thermal Spray Technology*, vol. 27, no. 8, pp. 1356–1370, Dec. 2018, doi: 10.1007/s11666-018-0766-3.

[27] S. Bose, D. Ke, A. A. Vu, A. Bandyopadhyay, and S. B. Goodman, “Thermal Oxide Layer Enhances Crystallinity and Mechanical Properties for Plasma-Sprayed Hydroxyapatite Biomedical Coatings,” *ACS Appl Mater Interfaces*, vol. 12, no. 30, pp. 33465–33472, Jul. 2020, doi: 10.1021/acsami.0c05035.

[28] F. Fanicchia and D. A. Axinte, “Transient three-dimensional geometrical/thermal modelling of thermal spray: Normal-impinging jet and single straight deposits,” *Int J Heat Mass Transf*, vol. 122, pp. 1327–1342, Jul. 2018, doi: 10.1016/j.ijheatmasstransfer.2018.01.127.

[29] A. A. Abubakar and A. F. M. Arif, “A hybrid computational approach for modeling thermal spray deposition,” *Surf Coat Technol*, vol. 362, pp. 311–327, Mar. 2019, doi: 10.1016/j.surfcoat.2019.02.010.

[30] G. Bolelli, A. Candeli, H. Koivuluoto, L. Lusvarghi, T. Manfredini, and P. Vuoristo, “Microstructure-Based Thermo-Mechanical Modelling of Thermal Spray Coatings,” *Mater Des*, vol. 73, pp. 20–34, May 2015, doi: 10.1016/j.matdes.2015.02.014.

[31] A. Czupryński, “Flame Spraying of Aluminum Coatings Reinforced with Particles of Carbonaceous Materials as an Alternative for Laser Cladding Technologies,” *Materials*, vol. 12, no. 21, Nov. 2019, doi: 10.3390/ma12213467.

[32] Y. Zhang *et al.*, “Microstructures and Properties of High-Entropy Alloys,” *Prog Mater Sci*, vol. 61, pp. 1–93, 2014, doi: 10.1016/j.pmatsci.2013.10.001.

[33] E. Jonda, L. Łatka, and W. Pakieła, “Microstructure and Selected Properties of Cr3C2–NiCr Coatings Obtained by HVOF on Magnesium Alloy Substrates,” *Materials*, vol. 13, no. 12, pp. 1–12, Jun. 2020, doi: 10.3390/ma13122775.

[34] P. Cavaliere, *Cold-Spray Coatings: Recent Trends and Future perspectives*. Springer International Publishing, 2017. doi: 10.1007/978-3-319-67183-3.

[35] J. Villafuerte, *Modern Cold Spray: Materials, Process, and Applications*. Springer International Publishing, 2015. doi: 10.1007/978-3-319-16772-5.

[36] H. Singh, M. Kumar, and R. Singh, “An Overview of Various Applications of Cold Spray Coating Process,” *Mater Today Proc*, vol. 56, pp. 2826–2830, Jan. 2022, doi: 10.1016/j.matpr.2021.10.160.

[37] O. Kovarik, J. Siegl, J. Cizek, T. Chraska, and J. Kondas, “Fracture Toughness of Cold Sprayed Pure Metals,” *Journal of Thermal Spray Technology*, vol. 29, no. 1–2, pp. 147–157, Jan. 2020, doi: 10.1007/s11666-019-00956-z.

[38] M. Wang, B. Yu, D. Chang, and L. Zheng, “Study on corrosion resistance of aluminium coating deposited on magnesium-zinc-yttrium-calcium alloy by cold spray,” *Materwiss Werksttech*, vol. 54, no. 3, pp. 267–274, Mar. 2023, doi: 10.1002/mawe.202100315.

[39] I. C. Park and S. J. Kim, “Electrochemical characteristics in seawater for cold thermal spray-coated Al-Mg alloy layer,” *Acta Metallurgica Sinica (English Letters)*, vol. 29, no. 8, pp. 727–734, Aug. 2016, doi: 10.1007/s40195-016-0437-7.

[40] J. Zhu *et al.*, “Microstructures, wear resistance and corrosion resistance of CoCrFeNi high entropy alloys coating on AZ91 Mg alloy prepared by cold spray,” *J Alloys Compd*, vol. 925, Dec. 2022, doi: 10.1016/j.jallcom.2022.166698.

[41] H. J. Kim, C. H. Lee, and S. Y. Hwang, “Fabrication of WC-Co coatings by cold spray deposition,” *Surf Coat Technol*, vol. 191, no. 2–3, pp. 335–340, Feb. 2005, doi: 10.1016/j.surfcoat.2004.04.058.

[42] K. Spencer, D. M. Fabijanic, and M. X. Zhang, “The Influence of Al2O3 Reinforcement on the Properties of Stainless Steel Cold Spray Coatings,” *Surf Coat Technol*, vol. 206, no. 14, pp. 3275–3282, Mar. 2012, doi: 10.1016/j.surfcoat.2012.01.031.

[43] K. S. Al-Hamdani, J. W. Murray, T. Hussain, A. Kennedy, and A. T. Clare, “Cold sprayed metal-ceramic coatings using satellited powders,” *Mater Lett*, vol. 198, pp. 184–187, Jul. 2017, doi: 10.1016/j.matlet.2017.03.175.

[44] J. Choi, N. Okimura, T. Yamada, Y. Hirata, N. Ohtake, and H. Akasaka, “Deposition of graphene–copper composite film by cold spray from particles with graphene grown on copper particles,” *Diam Relat Mater*, vol. 116, Jun. 2021, doi: 10.1016/j.diamond.2021.108384.

[45] Q. Wang, K. Spencer, N. Birbilis, and M. X. Zhang, “The Influence of Ceramic Particles on Bond Strength of Cold Spray Composite Coatings on AZ91 Alloy Substrate,” *Surf Coat Technol*, vol. 205, no. 1, pp. 50–56, Sep. 2010, doi: 10.1016/j.surfcoat.2010.06.008.

[46] K. Ravi, W. L. Sulen, C. Bernard, Y. Ichikawa, and K. Ogawa, “Fabrication of micro-/nano-structured super-hydrophobic fluorinated polymer coatings by cold-spray,” *Surf Coat Technol*, vol. 373, pp. 17–24, Sep. 2019, doi: 10.1016/j.surfcoat.2019.05.078.

[47] V. Bortolussi, B. Figliuzzi, F. Willot, M. Faessel, and M. Jeandin, “Electrical Conductivity of Metal–Polymer Cold Spray Composite Coatings onto Carbon Fiber-Reinforced Polymer,” *Journal of Thermal Spray Technology*, vol. 29, no. 4, pp. 642–656, Apr. 2020, doi: 10.1007/s11666-020-00999-7.

[48] E. Toyserkani, A. Khajepour, and Stephen. F. Corbin, “Laser Cladding,” Boca Raton, 2004.

[49] P. Cavaliere, *Laser Cladding of Metals*. Springer International Publishing, 2020. doi: 10.1007/978-3-030-53195-9.

[50] L. Zhu *et al.*, "Recent Research and Development Status of Laser Cladding: A Review," *Opt Laser Technol*, vol. 138, Jun. 2021, doi: 10.1016/j.optlastec.2021.106915.

[51] M. Kiehl, A. Scheid, K. Graf, B. Ernst, and U. Tetzlaff, "Coaxial Laser Cladding of Cobalt-Base Alloy Stellite™ 6 on Grey Cast Iron Analysis of the Microstructural and Mechanical Properties Depending on the Laser Power," *J Mater Eng Perform*, Apr. 2022, doi: 10.1007/s11665-022-07358-3.

[52] J. Wang, G. Jin, X. Feng, X. Cui, X. Wen, and Y. Zhao, "Al–Cu-based in-situ reinforced gradient coating on aluminum alloy by laser cladding: Tribological behavior under gradient loading and thermal conditions," *Mater Chem Phys*, vol. 301, p. 127595, Jun. 2023, doi: 10.1016/j.matchemphys.2023.127595.

[53] J. Li, C. Chen, T. Squartini, and Q. He, "A study on wear resistance and microcrack of the Ti 3 Al/TiAl + TiC ceramic layer deposited by laser cladding on Ti-6Al-4V alloy," *Appl Surf Sci*, vol. 257, no. 5, pp. 1550–1555, Dec. 2010, doi: 10.1016/j.apsusc.2010.08.094.

[54] Q. Wu, W. Li, N. Zhong, W. Gang, and W. Haishan, "Microstructure and wear behavior of laser cladding VC-Cr7C3 ceramic coating on steel substrate," *Mater Des*, vol. 49, pp. 10–18, 2013, doi: 10.1016/j.matdes.2013.01.067.

[55] Y. Feng, K. Feng, C. Yao, Z. Li, and J. Sun, "Microstructure and properties of in-situ synthesized (Ti3Al + TiB)/Ti composites by laser cladding," *Mater Des*, vol. 157, pp. 258–272, Nov. 2018, doi: 10.1016/j.matdes.2018.07.045.

[56] K. Liu, Y. Li, J. Wang, Q. Ma, J. Li, and X. Li, "Preparation, microstructural evolution and properties of Ni-Zr intermetallic/Zr-Si ceramic reinforced composite coatings on zirconium alloy by laser cladding," *J Alloys Compd*, vol. 647, pp. 41–49, Jun. 2015, doi: 10.1016/j.jallcom.2015.05.179.

[57] S. Da Sun, M. Leary, Q. Liu, and M. Brandt, " Evaluation of microstructure and fatigue properties in laser cladding repair of ultrahigh strength AerMet ® 100 steel ," *J Laser Appl*, vol. 27, no. S2, p. S29202, Feb. 2015, doi: 10.2351/1.4906377.

[58] H. Paydas, A. Mertens, R. Carrus, J. Lecomte-Beckers, and J. Tchoufang Tchuindjang, “Laser cladding as repair technology for Ti-6Al-4V alloy: Influence of building strategy on microstructure and hardness,” *Mater Des*, vol. 85, pp. 497–510, Nov. 2015, doi: 10.1016/j.matdes.2015.07.035.

[59] L. Sexton, S. Lavin, G. Byrne, and A. Kennedy, “Laser cladding of aerospace materials,” *J Mater Process Technol*, vol. 122, no. 1, pp. 63–68, 2002.

[60] J. Natarajan, C. H. Yang, and S. S. Karuppasamy, “Investigation on microstructure, nanohardness and corrosion response of laser cladded colmonoy-6 particles on 316l steel substrate,” *Materials*, vol. 14, no. 20, Oct. 2021, doi: 10.3390/ma14206183.

[61] G. L. de Faria, J. M. Á. de Paula, and M. S. F. de Lima, “Characterization of phase transformations and microstructural changes in an API 5CT L80 steel grade during Ni alloy laser cladding,” *Materials Research*, vol. 21, no. 5, 2018, doi: 10.1590/1980-5373-MR-2018-0294.

[62] X. J. Yan, H. Gugel, S. Huth, and W. Theisen, “Microstructures and properties of laser cladding NiTi alloy with W for biomedical applications,” *Mater Lett*, vol. 65, no. 19–20, pp. 2934–2936, Oct. 2011, doi: 10.1016/j.matlet.2011.06.040.

[63] G. long WU *et al.*, “Porous ceramic coating formed on 316L by laser cladding combined plasma electrolytic oxidation for biomedical application,” *Transactions of Nonferrous Metals Society of China (English Edition)*, vol. 32, no. 9, pp. 2993–3004, Sep. 2022, doi: 10.1016/S1003-6326(22)65998-3.

[64] X. Zhang *et al.*, “Laser cladding of manganese oxide doped aluminum oxide granules on titanium alloy for biomedical applications,” *Appl Surf Sci*, vol. 520, Aug. 2020, doi: 10.1016/j.apsusc.2020.146304.

[65] R. N. Johnson, “ElectroSpark Deposition: Principles and Applications,” Lake Buena Vista: Society of Vacuum Coaters, 2002.

[66] R. N. Johnson, R. C. Aungst, N. J. Hoffman, M. G. Cowgill, G. A. Whitlow, and W. L. Wilson, “Development of Low Friction Materials for LMFBR Component,” in *SPECIFIC NUCLEAR REACTORS AND ASSOCIATED PLANTS (E3500)*, M. H. Cooper, Ed.,

Champion: Proceedings of the international conference on liquid metal technology in energy production, 1967, pp. 122–130.

[67] R. N. Johnson and G. L. Sheldon, “Advances in the electrospark deposition coating process,” *Journal of Vacuum Science & Technology A: Vacuum, Surfaces, and Films*, vol. 4, no. 6, pp. 2740–2746, Nov. 1986, doi: 10.1116/1.573672.

[68] A. Lešnjak and J. Tušek, “Processes and properties of deposits in electrospark deposition,” *Science and Technology of Welding and Joining*, vol. 7, no. 6, pp. 391–396, Dec. 2002, doi: 10.1179/136217102225006886.

[69] P. D. Enrique, Z. Jiao, N. Y. Zhou, and E. Toyserkani, “Dendritic Coarsening Model for Rapid Solidification of Ni-Superalloy via Electrospark Deposition,” *J Mater Process Technol*, vol. 258, pp. 138–143, Aug. 2018, doi: 10.1016/j.jmatprotec.2018.03.023.

[70] Kenneth. P. Kees, “Hard-Facing with Electro-Spark Deposition,” Washington, 1983. doi: https://doi.org/10.2172/5537601.

[71] S. Peterkin, “Electro-Spark Deposition Machine Design, Physical Controls and Parameter Effects.”

[72] Pablo. D. Enrique, “Effect of Microstructure in Electrospark Deposition Repaired Conventional and Additive Manufactured Ni-Superalloys,” 2021.

[73] A. Lešnjak and J. Tušek, “Processes and Properties of Deposits in Electrospark Deposition,” *Science and Technology of Welding and Joining*, vol. 7, no. 6, pp. 391–396, Dec. 2002, doi: 10.1179/136217102225006886.

[74] V. D. Belik, R. V Litvin, M. S. Kovalchenko, and A. A. Rogozinskaya, “Effect of Pulse Duration and Size of Interelectrode Interval on Electrospark Spraying. II. Effect of Pulse Duration and Size of Interelectrode Interval on Composition and Mechanical Properties of Coatings,” *Powder Metallurgy and Metal Ceramics*, vol. 46, no. 2, pp. 115–121, 2007, doi: https://doi.org/10.1007/s11106-007-0015-7.

[75] S. Frangini and A. Masci, “A Study on the Effect of a Dynamic Contact Force Control for Improving Electrospark Coating Properties,” *Surf Coat Technol*, vol. 204, no. 16–17, pp. 2613–2623, May 2010, doi: 10.1016/j.surfcoat.2010.02.006.

[76] “Applications,” *Huysindustries*.

[77] R. N. Johnson, R. N. J. Senior, and S. Scientist, “Alternative Coatings for Wear and Corrosion: The Electrospark Deposition Process,” Richland, WA, 2002.

[78] C. Barile, C. Casavola, G. Pappalettera, and G. Renna, “Advancements in Electrospark Deposition (ESD) Technique: A Short Review,” *Coatings*, vol. 12, no. 10, p. 1536, Oct. 2022, doi: 10.3390/coatings12101536.

[79] H. Zhao, C. Gao, X. yu Wu, B. Xu, Y. jun Lu, and L. kuan Zhu, “A novel method to fabricate composite coatings via ultrasonic-assisted electro-spark powder deposition,” *Ceram Int*, vol. 45, no. 17, pp. 22528–22537, Dec. 2019, doi: 10.1016/j.ceramint.2019.07.279.

[80] A. A. Burkov, E. R. Zaikova, and M. I. Dvornik, “Deposition of Ti–Ni–Zr–Mo–Al–C Composite Coatings on the Ti6Al4V Alloy by Electrospark Alloying in a Granule Medium,” *Surface Engineering and Applied Electrochemistry*, vol. 54, no. 6, pp. 546–554, Nov. 2018, doi: 10.3103/S1068375518060030.

[81] A. A. Burkov, “The Effect of Discharge Pulse Energy in Electrospark Deposition of Amorphous Coatings,” *Protection of Metals and Physical Chemistry of Surfaces*, vol. 58, no. 5, pp. 1018–1027, Oct. 2022, doi: 10.1134/S2070205122050057.

[82] P. D. Enrique, E. Marzbanrad, Y. Mahmoodkhani, Z. Jiao, E. Toyserkani, and N. Y. Zhou, “Surface Modification of Binder-Jet Additive Manufactured Inconel 625 via Electrospark Deposition,” *Surf Coat Technol*, vol. 362, pp. 141–149, Mar. 2019, doi: 10.1016/j.surfcoat.2019.01.108.

[83] P. D. Enrique, Z. Jiao, and N. Y. Zhou, “Effect of Direct Aging on Heat-Affected Zone and Tensile Properties of Electrospark-Deposited Alloy 718,” *Metall Mater Trans A Phys Metall Mater Sci*, vol. 50, no. 1, pp. 285–294, Jan. 2019, doi: 10.1007/s11661-018-4997-1.

[84] P. D. Enrique *et al.*, “Enhancing Fatigue Life of Additive Manufactured Parts with Electrospark Deposition Post-Processing,” *Addit Manuf*, vol. 36, Dec. 2020, doi: 10.1016/j.addma.2020.101526.

[85] S. Spadlo, W. Depczyński, and P. Mlynarczyk, “Modification of the surface layer of magnesium with 1050A aluminum alloy using electrospark deposition,” in *IOP Conference*

Series: Materials Science and Engineering, Institute of Physics Publishing, Oct. 2019. doi: 10.1088/1757-899X/629/1/012017.

[86] C. Geng, H. Zhang, X. Li, and H. Geng, "Elevated temperature tensile behaviour of 5183 aluminium alloy made by electrospark deposition additive manufacturing," *Materials Science and Engineering: A*, vol. 868, p. 144746, Mar. 2023, doi: 10.1016/j.msea.2023.144746.

[87] Z. Jiao, "Surface Modification of Stainless Steel by Electro-Spark Deposition," Waterloo, 2016. Accessed: May 31, 2023. [Online]. Available: http://hdl.handle.net/10012/11098

[88] I. Pliszka and N. Radek, "Corrosion Resistance of WC-Cu Coatings Produced by Electrospark Deposition," in *Procedia Engineering*, Elsevier Ltd, 2017, pp. 707–712. doi: 10.1016/j.proeng.2017.06.122.

[89] K. R. Chan, "Weldability and Degradation Study of Coated Electrodes for Resistance Spot Welding," 2005.

[90] C. J. Chen, M. C. Wang, D. S. Wang, H. S. Liang, and P. Feng, "Characterisations of electrospark deposition Stellite 6 alloy coating on 316L sealed valve used in nuclear power plant," *Materials Science and Technology*, vol. 26, no. 3, pp. 276–280, Mar. 2010, doi: 10.1179/174328409X430447.

[91] D. F. Paulonis and J. J. Schirra, "Alloy 718 at Pratt & Whitney – Historical Perspective and Future Challenges," 2001. doi: https://doi.org/10.7449/2001/superalloys_2001_13_23.

[92] R. I. Jewett and J. A. H. Rocketdyne, "The Use OF Alloy 718 in the Space Shuttle Main Engine," 1991. doi: https://doi.org/10.7449/1991/superalloys_1991_749_760.

[93] Y. Liu *et al.*, "Recent Progress on Evolution of Precipitates in Inconel 718 Superalloy," *Acta Metallurgica Sinica*, vol. 52, no. 10, pp. 1259–1266, Oct. 2016, doi: 10.11900/0412.1961.2016.00290.

[94] M. Jouiad *et al.*, "Microstructure and Mechanical Properties Evolutions of Alloy 718 During Isothermal and Thermal Cycling Over-Aging," *Mater Des*, vol. 102, pp. 284–296, Jul. 2016, doi: 10.1016/j.matdes.2016.04.048.

[95] M. Sundararaman, P. Mukhopadhyay, and S. Banerjee, “Carbide Precipitation in Nickel Base Superalloys 718 and 625 and Their Effect on Mechanical Properties,” 1997. doi: https://doi.org/10.7449/1997/superalloys_1997_367_378.

[96] F. Stein and A. Leineweber, “Laves Phases: A Review of Their Functional and Structural Applications and an Improved Fundamental Understanding of Stability and Properties,” *J Mater Sci*, vol. 56, no. 9, pp. 5321–5427, Mar. 2021, doi: 10.1007/s10853-020-05509-2.

[97] S. Sui, J. Chen, E. Fan, H. Yang, X. Lin, and W. Huang, “The Influence of Laves Phases on the High-Cycle Fatigue Behavior of Laser Additive Manufactured Inconel 718,” *Materials Science and Engineering A*, vol. 695, pp. 6–13, May 2017, doi: 10.1016/j.msea.2017.03.098.

[98] L. M. Felix, C. C. F. Kwan, and N. Y. Zhou, “The Effect of Pulse Energy on the Defects and Microstructure of Electro-Spark-Deposited Inconel 718,” *Metall Mater Trans A Phys Metall Mater Sci*, vol. 50, no. 9, pp. 4223–4231, Sep. 2019, doi: 10.1007/s11661-019-05332-8.

[99] E. Anisimov, A. K. Khan, and O. A. Ojo, “Analysis of Microstructure in Electro-Spark Deposited IN718 Superalloy,” *Mater Charact*, vol. 119, pp. 233–240, Sep. 2016, doi: 10.1016/j.matchar.2016.07.025.

[100] C.-J. Tong *et al.*, “Microstructure Characterization of AlxCoCrCuFeNi High-Entropy Alloy System with Multiprincipal Elements,” *Metallurgical and Materials Transactions A*, vol. 36, no. 4, pp. 881–893, 2005, doi: https://doi.org/10.1007/s11661-005-0283-0.

[101] E. P. George, D. Raabe, and R. O. Ritchie, “High-Entropy Alloys,” *Nat Rev Mater*, vol. 4, no. 8, pp. 515–534, Aug. 2019, doi: 10.1038/s41578-019-0121-4.

[102] J. W. Yeh, “Recent Progress in High-Entropy Alloys,” *Annales de Chimie: Science des Materiaux*, vol. 31, no. 6, pp. 633–648, Nov. 2006, doi: 10.3166/acsm.31.633-648.

[103] B. Cantor, I. T. H. Chang, P. Knight, and A. J. B. Vincent, “Microstructural Development in Equiatomic Multicomponent Alloys,” *Materials Science and Engineering A*, vol. 375–377, no. 1-2 SPEC. ISS., pp. 213–218, Jul. 2004, doi: 10.1016/j.msea.2003.10.257.

[104] J. Yeh, S. Chen, J. Gan, and S. Lin, “Formation of Simple Crystal Structures in Cu-Co-Ni-Cr-Al-Fe-Ti-V Alloys with Multiprincipal Metallic Elements,” *Metallurgical and Materials Transactions A*, vol. 35, pp. 2533–2536, 2004.

[105] D. B. Miracle and O. N. Senkov, “A Critical Review of High Entropy Alloys and Related Concepts,” *Acta Materialia*, vol. 122. Elsevier Ltd, pp. 448–511, Jan. 01, 2017. doi: 10.1016/j.actamat.2016.08.081.

[106] O. N. Senkov, G. B. Wilks, D. B. Miracle, C. P. Chuang, and P. K. Liaw, “Refractory High-Entropy Alloys,” *Intermetallics (Barking)*, vol. 18, no. 9, pp. 1758–1765, Sep. 2010, doi: 10.1016/j.intermet.2010.05.014.

[107] O. N. Senkov, G. B. Wilks, J. M. Scott, and D. B. Miracle, “Mechanical Properties of Nb25Mo25Ta25W25 and V20Nb20Mo20Ta20W20 Refractory High Entropy Alloys,” *Intermetallics (Barking)*, vol. 19, no. 5, pp. 698–706, May 2011, doi: 10.1016/j.intermet.2011.01.004.

[108] V. H. Hammond, M. A. Atwater, K. A. Darling, H. Q. Nguyen, and L. J. Kecskes, “Equal-Channel Angular Extrusion of a Low-Density High-Entropy Alloy Produced by High-Energy Cryogenic Mechanical Alloying,” *JOM*, vol. 66, no. 10, pp. 2021–2029, Oct. 2014, doi: 10.1007/s11837-014-1113-x.

[109] X. Yang, S. Y. Chen, J. D. Cotton, and Y. Zhang, “Phase Stability of Low-Density, Multiprincipal Component Alloys Containing Aluminum, Magnesium, and Lithium,” *JOM*, vol. 66, no. 10, pp. 2009–2020, Oct. 2014, doi: 10.1007/s11837-014-1059-z.

[110] A. Takeuchi, K. Amiya, T. Wada, K. Yubuta, and W. Zhang, “High-Entropy Alloys with a Hexagonal Close-Packed Structure Designed by Equi-Atomic Alloy Strategy and Binary Phase Diagrams,” *JOM*, vol. 66, no. 10, pp. 1984–1992, Oct. 2014, doi: 10.1007/s11837-014-1085-x.

[111] C. Hsu, J. Yeh, S. Chen, and T. Shun, “Wear Resistance and High-Temperature Compression Strength of FCC CuCoNiCrAl0.5Fe Alloy with Boron Addition,” *Metallurgical and Materials Transactions A*, vol. 35, pp. 1465–1469, 2004, doi: https://doi.org/10.1007/s11661-004-0254-x.

[112] B. S. Murty, S. Ranganathan, and J. W. Yeh, *High-Entropy Alloys*. Butterworth-Heinemann, 2014.

[113] T. K. Chen, T. T. Shun, J. W. Yeh, and M. S. Wong, “Nanostructured Nitride Films of Multi-Element High-Entropy Alloys by Reactive DC Sputtering,” *Surf Coat Technol*, vol. 188–189, no. 1-3 SPEC.ISS., pp. 193–200, Nov. 2004, doi: 10.1016/j.surfcoat.2004.08.023.

[114] S. Güler, E. D. Alkan, and M. Alkan, “Vacuum Arc Melted and Heat Treated AlCoCrFeNiTiX Based High-Entropy Alloys: Thermodynamic and Microstructural Investigations,” *J Alloys Compd*, vol. 903, May 2022, doi: 10.1016/j.jallcom.2022.163901.

[115] O. A. Waseem and H. J. Ryu, “Powder Metallurgy Processing of a Wx TaTiVCr High-Entropy Alloy and Its Derivative Alloys for Fusion Material Applications,” *Sci Rep*, vol. 7, no. 1, Dec. 2017, doi: 10.1038/s41598-017-02168-3.

[116] S. Varalakshmi, M. Kamaraj, and B. S. Murty, “Processing and Properties of Nanocrystalline CuNiCoZnAlTi High Entropy Alloys by Mechanical Alloying,” *Materials Science and Engineering A*, vol. 527, no. 4–5, pp. 1027–1030, Feb. 2010, doi: 10.1016/j.msea.2009.09.019.

[117] J. Liu, Y. Guan, X. Xia, P. Peng, Q. Ding, and X. Liu, “Laser Cladding of Al0.5CoCrCuFeNiSi High Entropy Alloy Coating Without and with Yttria Addition on H13 Steel,” *Crystals (Basel)*, vol. 10, no. 4, Apr. 2020, doi: 10.3390/cryst10040320.

[118] Y. Li and Y. Shi, “Microstructure and Wear Resistance of the Laser-Cladded Al0.8CrFeCoNiCu0.5Bx High-entropy Alloy Coating on Aluminum,” *Mater Res Express*, vol. 7, no. 2, 2020, doi: 10.1088/2053-1591/ab7161.

[119] A. S. M. Ang *et al.*, “Plasma-Sprayed High Entropy Alloys: Microstructure and Properties of AlCoCrFeNi and MnCoCrFeNi,” *Metall Mater Trans A Phys Metall Mater Sci*, vol. 46, no. 2, pp. 791–800, Feb. 2015, doi: 10.1007/s11661-014-2644-z.

[120] S. Feng *et al.*, “Cold Spray Additive Manufacturing of CoCrFeNiMn High-Entropy Alloy: Process Development, Microstructure, and Mechanical Properties,” *Journal of Thermal Spray Technology*, vol. 31, no. 4. Springer, pp. 1222–1231, Apr. 01, 2022. doi: 10.1007/s11666-022-01374-4.

[121] P. Jenczyk, D. M. Jarzabek, Z. Lu, E. Gadalińska, N. Levintant-Zayonts, and Y. Zhang, “Unexpected Crystallographic Structure, Phase Transformation, and Hardening Behavior in the AlCoCrFeNiTi0.2 High-Entropy Alloy after High-Dose Nitrogen Ion Implantation,” *Mater Des*, vol. 216, Apr. 2022, doi: 10.1016/j.matdes.2022.110568.

[122] V. Soare *et al.*, “Electrochemical Deposition and Microstructural Characterization of AlCrFeMnNi and AlCrCuFeMnNi High Entropy Alloy Thin Films,” *Appl Surf Sci*, vol. 358, pp. 533–539, Dec. 2015, doi: 10.1016/j.apsusc.2015.07.142.

[123] H. Schwarz *et al.*, “CoCrFeNi High-entropy Alloy Thin Films Synthesised by Magnetron Sputter Deposition from Spark Plasma Sintered Targets,” *Coatings*, vol. 11, no. 4, Apr. 2021, doi: 10.3390/coatings11040468.

[124] Chandrakant, N. S. Reddy, and B. B. Panigrahi, “Electro Spark Coating of AlCoCrFeNi High Entropy Alloy on AISI410 Stainless Steel,” *Mater Lett*, vol. 304, Dec. 2021, doi: 10.1016/j.matlet.2021.130580.

[125] C. A. Manea, M. Sohaciu, R. Stefănoiu, M. I. Petrescu, M. V. Lungu, and I. Csaki, “New HfNbTaTiZr High-Entropy Alloy Coatings Produced by Electrospark Deposition with High Corrosion Resistance,” *Materials*, vol. 14, no. 15, Aug. 2021, doi: 10.3390/ma14154333.

[126] K. A. Kuptsov *et al.*, “High-entropy Fe-Cr-Ni-Co-(Cu) Coatings Produced by Vacuum Electro-Spark Deposition for Marine and Coastal Applications,” *Surf Coat Technol*, vol. 453, Jan. 2023, doi: 10.1016/j.surfcoat.2022.129136.

[127] M. N. Hussain and A. Dash, “Analysis Active Vibration of Ti-Alloy Gas Turbine Blade Rotation after Grind-Out Repair of Surface Damage,” *International Journal of Research in Engineering and Science (IJRES) ISSN*, vol. 3, no. 71, pp. 86–92, 2015, [Online]. Available: www.ijres.org

[128] X. R. Wang, Z. Q. Wang, T. S. Lin, and P. He, “Mass Transfer Trends of AlCoCrFeNi High-Entropy Alloy Coatings on TC11 Substrate via Electrospark − Computer Numerical Control Deposition,” *J Mater Process Technol*, vol. 241, pp. 93–102, Mar. 2017, doi: 10.1016/j.jmatprotec.2016.09.012.

[129] V. P. Konoval, O. P. Umanskii, A. D. Panasyuk, and O. F. Lukyanchuk, “Effect of the Chemical Composition of Electrode Materials and Deposition Parameters on the Properties of Electrospark-Deposited Coatings. I. Mass Transfer Rate and Coating Composition,” *Powder Metallurgy and Metal Ceramics*, vol. 53, no. 2, pp. 31–39, 2014, doi: https://doi.org/10.1007/s11106-014-9584-4.

[130] A. K. Sahu and S. Bag, “Design of a Double Aging Treatment for the Improvement of Mechanical and Microstructural Properties of Pulse Micro-Plasma Arc Welded Alloy 718,” *J Mater Sci*, vol. 56, no. 23, pp. 13400–13415, Aug. 2021, doi: 10.1007/s10853-021-06121-8.

[131] P. D. Enrique, S. Peterkin, and N. Y. Zhou, “Parametric Study of Automated Electrospark Deposition for Ni-Based Superalloys,” *Weld J*, vol. 100, no. 7, pp. 239–248, Jul. 2021, doi: 10.29391/2021.100.021.

[132] Y. Ruan, A. Mohajerani, and M. Dao, “Microstructural and Mechanical-Property Manipulation through Rapid Dendrite Growth and Undercooling in an Fe-based Multinary Alloy,” *Sci Rep*, vol. 6, Aug. 2016, doi: 10.1038/srep31684.

[133] C. Wang *et al.*, “Microstructure and Corrosion Properties of Laser Remelted CrFeCoNi and CrMnFeCoNi High Entropy Alloys Coatings,” *Journal of Materials Research and Technology*, vol. 15, pp. 5187–5196, Nov. 2021, doi: 10.1016/j.jmrt.2021.10.042.

[134] C. H. Tsau, C. Y. Yeh, and M. C. Tsai, “The Effect of Nb-Content on the Microstructures and Corrosion Properties of CrFeCoNiNbx High-Entropy Alloys,” *Materials*, vol. 12, no. 22, Nov. 2019, doi: 10.3390/ma12223716.

[135] S. Kou, *Welding Metallurgy*. Wiley, 2002. doi: 10.1002/0471434027.

[136] Z. Jiao *et al.*, “Surface Modification of 304 Stainless Steel by Electro-Spark Deposition,” *J Mater Eng Perform*, vol. 27, no. 9, pp. 4799–4809, Sep. 2018, doi: 10.1007/s11665-018-3579-0.

[137] P. Muangtong, R. M. Namus, and R. Goodall, “Improved Tribocorrosion Resistance by Addition of Sn to CrFeCoNi High Entropy Alloy,” *Metals (Basel)*, vol. 11, no. 1, pp. 1–14, Jan. 2021, doi: 10.3390/met11010013.

[138] G. A. Salishchev *et al.*, “Effect of Mn and V on Structure and Mechanical Properties of High-Entropy Alloys Based on CoCrFeNi System,” *J Alloys Compd*, vol. 591, pp. 11–21, Apr. 2014, doi: 10.1016/j.jallcom.2013.12.210.

[139] T. Lindner, M. Löbel, E. Saborowski, L. M. Rymer, and T. Lampke, “Wear and Corrosion Behaviour of Supersaturated Surface Layers in the High-Entropy Alloy Systems CrMnFeCoNi and CrFeCoNi,” *Crystals (Basel)*, vol. 10, no. 2, Feb. 2020, doi: 10.3390/cryst10020110.

[140] M. Löbel, T. Lindner, R. Hunger, R. Berger, and T. Lampke, “Precipitation Hardening of the HVOF Sprayed Single-Phase High-Entropy Alloy CrFeCoNi,” *Coatings*, vol. 10, no. 7, Jul. 2020, doi: 10.3390/coatings10070701.

[141] K. Holmberg and A. Matthews, *Coatings Tribology: Properties, Mechanisms, Techniques and Applications in Surface Engineering*, 2nd ed. Elsevier, 2009.

[142] W. Luo, U. Selvadurai, and W. Tillmann, “Effect of Residual Stress on the Wear Resistance of Thermal Spray Coatings,” *Journal of Thermal Spray Technology*, vol. 25, no. 1–2, pp. 321–330, Jan. 2016, doi: 10.1007/s11666-015-0309-0.

[143] Y. J. Cao *et al.*, “Effect of the Microstructure and Residual Stress on Tribological Behavior of Induction Hardened GCr15 Steel,” *Tribol Int*, vol. 115, pp. 108–115, 2017, doi: 10.1016/j.triboint.2017.05.028.

[144] Y. Feng, X. Pang, K. Feng, Y. Feng, and Z. Li, “Residual Stress Distribution and Wear Behavior in Multi-Pass Laser Cladded Fe-Based Coating Reinforced by M3(C, B),” *Journal of Materials Research and Technology*, vol. 15, pp. 5597–5607, Nov. 2021, doi: 10.1016/j.jmrt.2021.11.032.

[145] X. T. Centrich, E. Shehab, P. Sydor, T. Mackley, P. John, and A. Harrison, “An Aerospace Requirements Setting Model to Improve System Design,” in *Procedia CIRP*, Elsevier B.V., 2014, pp. 287–292. doi: 10.1016/j.procir.2014.07.127.

[146] L. Witek, “Failure Analysis of Turbine Disc of an Aero Engine,” *Eng Fail Anal*, vol. 13, no. 1, pp. 9–17, Jan. 2006, doi: 10.1016/j.engfailanal.2004.12.028.

[147] “Impeller,” *UltiMaker Thingiverse*.

[148] “Turbine blade,” *GrabCAD Community Library*.

[149] Y. Wang, Y. Yang, H. Yang, M. Zhang, S. Ma, and J. Qiao, “Microstructure and wear properties of nitrided AlCoCrFeNi high-entropy alloy,” *Mater Chem Phys*, vol. 210, pp. 233–239, May 2018, doi: 10.1016/j.matchemphys.2017.05.029.

[150] M. Löbel, T. Lindner, T. Mehner, and T. Lampke, “Influence of titanium on microstructure, phase formation and wear behaviour of AlCoCrFeNiTix high-entropy alloy,” *Entropy*, vol. 20, no. 7, Jul. 2018, doi: 10.3390/e20070505.

[151] H. Jiang, K. Han, D. Li, and Z. Cao, “Synthesis and characterization of AlCoCrFeNiNbx high-entropy alloy coatings by laser cladding,” *Crystals (Basel)*, vol. 9, no. 1, pp. 1–11, Jan. 2019, doi: 10.3390/cryst9010056.

[152] M. Löbel, T. Lindner, S. Clauß, R. Pippig, D. Dietrich, and T. Lampke, “Microstructure and Wear Behavior of the High-Velocity-Oxygen-Fuel Sprayed and Spark Plasma Sintered High-Entropy Alloy AlCrFeCoNi,” *Adv Eng Mater*, vol. 23, no. 4, Apr. 2021, doi: 10.1002/adem.202001253.